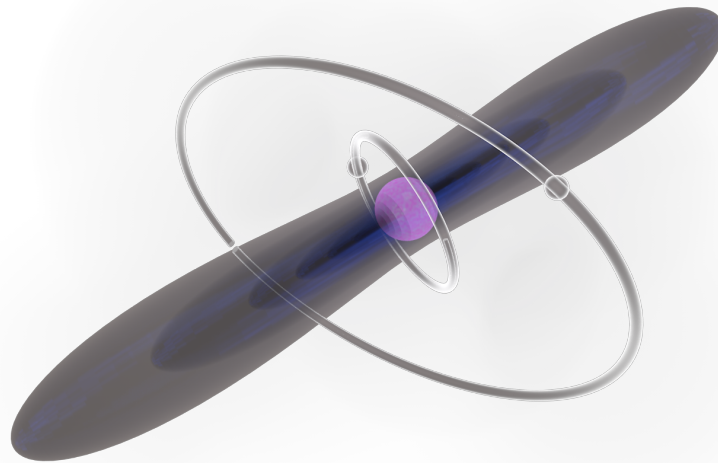# Single ytterbium atoms in an optical tweezer array: high-resolution spectroscopy, single-photon Rydberg excitation, and a scheme for nondestructive detection

A dissertation submitted to

the Department of Physics of the Kyoto University

presented by

Daichi Okuno

for the degree of Doctor of Science

Abstract

Arrays of interacting neutral atoms trapped in individually controllable optical tweezers are versatile platform for quantum simulation and quantum computing. Use of two–electron atoms, in contrast to the alkali atoms, offers abundant internal state structures beneficial for control and measurement of quantum state of atoms.

We present an experimental system for Rydberg tweezer arrays with ytterbium (Yb) atoms featuring internal state manipulation between the ground $^1S_0$ and the metastable $^3P_2$ states, and single-photon excitation from the $^3P_2$ to Rydberg states. In the experiments, single Yb atoms are trapped in two-dimensional arrays of optical tweezers and are detected by fluorescence imaging with the intercombination $^1S_0 \leftrightarrow {}^3P_1$ transition, and the defect-free single atom arrays are prepared by the rearrangement with the feedaback. We successfully perform high-resolution $^1S_0 \leftrightarrow {}^3P_2$ state spectroscopy for the single atoms, demonstrating the utilities of this ultranarrow transition. We further perform single-photon excitation from the $^3P_2$ to Rydberg states for the single atoms, which is a key for the efficient Rydberg excitation. We also perform a systematic measurement of a complex energy structure of a series of D states including newly observed $^3D_3$ states. The developed system shows feasibility of future experiments towards quantum simulations and computations using single Yb atoms.

For such detections of single atoms as we performed, considerable heatings occur which might cause the change of internal state as well as losses from traps, which is especially problematic for atoms in an optical lattice. We here propose two schemes for detection of single atoms in an optical trap without change of internal state. The first one uses the magic condition of optical trap for the probe transition, which preserve the vibrational state of atoms, and the second one adopts the dispersive Faraday detection with combination of a squeezed vacuum state, which can realize the detection of atoms without photon absorption, which is considered as a nondestructive detection of the number of atoms. This work open the possibility for non-destructive observation of quantum dynamics of quantum many-body system, especially in an optical lattice.

Contents

List of Figures

Introduction

1.1 Rydberg atom tweezer array

Since the first realization of single-site resolved imaging of atoms in an optical lattice in Hubbard regime [1], known as quantum gas microscopy (QGM) [2–17], single atoms as a tool for quantum many-body physics is attracting much attentions [18]. An array of atoms in optical tweezers (OTs) is another approach to exploit single atoms [19]. Though trappping and detection of single atom in a single OT were achieved much earlier [20], site-resolved imaging and preparation of a defect-free atom array were accomplished later than the QGM [21, 22]. The technique is, however, developing remarkably rapidly since then. Atom tweezer array offers arbitrarily flexible geometry of atoms in contrast to an optical lattice, but with a difficulty of introducing tunnelings between adjacent sites. The interaction between other sites is mostly generated by an excitation to Rydberg states, in which the outermost electron is in a highly excited orbit with a principal quantum number typically larger than 10. The dynamics is described as a spin-model such as Ising model [23], in contrast to optilcal lattice system in which the dynamics is described well as a Hubbard model by on-site interactions and tunnelings [24]. Let us see the hamiltonian of interacting Rydberg atoms with interactions V_{ij} between i-th and j-th atoms, coupled to the ground state by a laser with the rabi frequency Ω and the detuning Δ. The Hamiltonian is given by

$$\mathcal{H}/\hbar = \frac{\Omega}{2} \sum_i \left(|g_i\rangle \langle r_i| + \text{h.c.} \right) - \Delta \sum_i |r_i\rangle \langle r_i| + \sum_{ij} (V_{ij}/h) |r_i r_j\rangle \langle r_i r_j|, \tag{1.1}$$

where $|g_i\rangle$ and $|r_i\rangle$ denotes the ground and the excited state of the i-th atom, respectively. One can find an analogy between Eq. (1.1) and the transverse-field Ising model, by regarding the first, the second, and the third term as the transverse-field, the longitudinal-field, and the spin-spin interaction term, respectively. $|g\rangle$ and $|r\rangle$ corresponds to spin up $|\uparrow\rangle$ and down $|\downarrow\rangle$. The difference lies in the interaction term. While the interaction in Ising model depends on whether the interacting spins are parallel or antiparallel, in Eq. (1.1) the interaction depends on whether atoms are simultaneously excited (spin up) or not. Quantum simulation of the dynamics under Eq. (1.1) is important

for condensed matter physics. Quantum phase transitions has been studied using hundreds of atoms [25, 26].

    An atom array is also considered as a promising quantum computing platform [27, 28]. As we describe in section 3.2.4, strong interactions between Rydberg atoms allow us to perform two-qubit gate operations. We summarize previous experiments of the atom tweezer array based quantum computing platforms in Table 1.1. For alkali atoms, single-qubit and two-qubit gate operations on hyperfine clock states ($|F, m_F = 0\rangle \leftrightarrow |F', m_{F'} = 0\rangle$) or on the ground and Rydberg states, such as Toffoli gates [29,30] or generation of Bell or cat states [31–33], based on Rydberg interactions have been demonstrated. Comparing with other physical systems such as trapped ions or superconducting circuits, the most important advantage of neutral atoms is its scalability. Many atoms can be trapped with the spacing of typically $1\,\mu$m to $5\,\mu$m without affecting each others, unless we generate interactions between them. In fact, several hundreds or a thousand of atoms can be prepared in an OT array [25,26]. The number of trapped atoms is limited by some factors such as the field of view of the optical system or the power of the OT beams, which limit the number of OTs. Another difficulty unique to neutral atoms is the vulnerability to collisions with background-gas atoms, which causes escapes of atoms from the trap. Collisions occur once every $100\,$s typically for a standard room-temperature vacuum chamber [34]. This is one of the dominant limiting factor, since the lower loss rate is required as the size of atom array becomes larger. A natural way to reduce the collisions is to use a cryogenic chamber, which enables trapping of atoms for tens of minutes. Lifetimes up to $6000\,$s is demonstrated using a $4\,$K environment recently [35].

    In addition to above mentioned achievements, use of alkaline-earth (like) atoms (AE(L)As) rather than alkali atoms offers a fundamentally advantageous physical platform for quantum computing and simulation, as we describe in the next section.

Table 1.1: List of notable atom tweezer array based quantum computing platforms ever realized.

Group	Atomic species	Qubit state	Clifford fidelity	Bell state fidelity	Ref.
M. Lukin (Harvard University)	^{87}Rb	$\lvert 5S_{1/2}, F = 2, m_F = -2\rangle$ $\lvert 70S, J = 1/2, m_J = -1/2\rangle$		$\geq 0.97(3)$	[36]
M. Saffman (University of Wisconsin–Madison) (ColdQuanta)	Cs	$\lvert 6S_{1/2}, F = 3, m_F = 0\rangle$ $\lvert 6S_{1/2}, F = 4, m_F = 0\rangle$	$0.9961(4)$	$0.955^{\dagger}$	[32,37]
M. Endres (Caltech)	^{88}Sr	$\lvert (5s)(5p)^3P_0\rangle$ $\lvert (5s)(61s)^3S_1, m_J = 0\rangle$	$0.9967(9)^{\dagger}$	$\leq 0.991(4)^{\dagger}$	[38]
Atom Computing	^{87}Sr	$\lvert (5s^2)^1S_0, F = 9/2, m_F = -9/2\rangle$ $\lvert (5s^2)^1S_0, F = 9/2, m_F = -7/2\rangle$			[39]
A. M. Kaufman	^{88}Sr	$\lvert (5s)^2\,^1S_0\rangle, \lvert (5s)(5p)\,^3P_0\rangle$		$0.928(20)$	[40]
(JILA)	^{171}Yb	$\lvert (6s^2)^1S_0, F = 1/2, m_F = \pm 1/2\rangle$	$0.9948(5)$		[41]
J. D. Thompson (Princeton University)	^{171}Yb	$\lvert (6s^2)^1S_0, F = 1/2, m_F = \pm 1/2\rangle$	$0.99959(6)$	$0.83(2)$	[42]

† SPAM corrected

1.2   Alkali atoms vs. Alkaline-earth (like) atoms

Alkaline-earth (like) atoms which possesses two valence electrons, such as strontium (Sr) and ytterbium (Yb), have many intriguing and useful properties for quantum simulation, quantum computing, and also quantum metrology. The most well known application should be an optical lattice clock [43] using the ultra-narrow $^1S_0 \leftrightarrow ^3P_0$ transition for the frequency standard, which reached the level that enables the observation of gravitational redshift across millimeter scale atomic samples recently [44]. The utilization of AE(L)A to the OT array system as well as the optical lattice system is a hot topic since the first realizations for Sr [45, 46] and Yb [47]. The clock based on an OT array has also been demonstrated [48–50]. This can be regarded as a hybrid of an optical lattice clock and an ion clock. The tunable and large separation of atoms offer less interatomic collisions, while allowing simultaneous interrogations to multiple atoms repeatedly without dead time by loading of atoms to the array. In particular, an ensemble of 150 Sr atoms has been used for a clock in a cut-of-edge experiment [50].

The ultra-narrow transition is also considered as a good resource for quantum computing. Quantum gate operations in an OT array system using the clock $^3P_0$ state have been demonstrated [38, 40], achieving 99.67% SPAM-corrected fidelity for single-atom π-rotation and 99.1(3)% for the Bell state fidelity. Despite these investigations using the $^3P_0$ state, experiments utilizing the $^3P_2$ state has not been performed so far, in spite of its comparable lifetime and linewidth to those of the $^3P_0$ state. There are also several unique features of the $^3P_2$ state compared to $^3P_0$ [51, 52]: First, the polarizability of the $^3P_2$ state can be widely tuned by changing the magnetic field orientation with respect to the trapping light. Thus, the magic-like condition can be achieved without choosing any special wavelengths. Second, the Zeeman shift of the $J = 2$ electronic spin enables individual addressing of the atoms in different tweezer sites with a modest strength of the magnetic field gradient, as demonstrated for the atoms in an optical lattice [53]. Third, the $m_J = 0$ state of the bosonic isotopes is expected to be less sensitive to the magnetic field fluctuations than the $^3P_0$ state as the second-order Zeeman coefficients for the $^3P_0$ and $^3P_2$ states are caluclated to be $-6.0\,\text{Hz/G}^2$ and $1.2\,\text{Hz/G}^2$, respectively [54]. This implies that the $^1S_0$–$^3P_2$ ($m_J = 0$) system of the bosonic isotopes can be a promising qubit as well as a good resource for precision measurements.

The metastable states also enables a possibility of single-photon Rydberg excitation which offers a lossless excitation and an ideal controlled phase gate. Rydberg state excitation of alkali atoms is usually performed by a two-photon process with an intermediate state with a short lifetime mainly because of the difficulty of generating sufficient power at ultra-violet wavelengths for a single-photon excitation from the ground state. The protocol of two-qubit gate such as a controlled-Z gate based on this three-level system suffers from severe requirements of phase shift for exquisite adjustment of parameters to recover an ideal gate [55], as well as decoherence arising from the short lifetime of the intermediate state. Use of a metastable state of two-electron atoms, on the other hand, enables driving to Rydberg states within a two-level system free from such phase shifts and decoherence. Coherent driving between the $^3P_0$ and a Rydberg state was indeed demonstrated with ^{88}Sr [38].

Another important feature of AE(L)As is the absence of the electron spins in the $^1S_0$ and $^3P_0$

electronic states, which makes it possible to realize nuclear spin qubits with fermionic isotopes robust against environmental magnetic field fluctuations [56]. The advantage of the use of the nuclear spin degrees of freedom of ^{171}Yb, in particular, in quantum information processing was discussed in [51, 57, 58]. Coherent nuclear spin control between two out of ten spin components in ^{87}Sr [39] and between the two spin components in ^{171}Yb [41, 42] in optical tweezers were experimentally demonstrated recently. Furthermore, the nuclear spins of ^{1}S$_0$ and the ^{3}P$_0$ state is considered as a powerful tool for the quantum simulation of the SU($\mathcal{N}$) Hubbard model [59, 60].

There are also significant differences between the Rydberg states of alkali atoms and AE(L)As, which originates from the remaining inner valence electron. The Rydberg electron's orbit is so large that it is justified to treat the Rydberg electron and the inner core separately. In the case of alkali atoms, the electron configuration of the atomic core part is the same as that of noble gas atoms, which is stable and scarcely interact with photons. In the case of AE(L)A, however, the core part is equivalent to a monovalent ion, which has strong optical transitions. The resonant transition leads to doubly excited Rydberg states, (6p)(nl) for the case of Yb atoms, followed by evolving into ionized state, referred to as auto-ionization [61]. High-fidelity detection of Rydberg states [38] with the aid of auto-ionization process and control of energy shift of Rydberg states [62, 63] have been demonstrated for single atoms in an OT array.

The most important consequence of this ionic-core transition is the optical dipole trap of Rydberg states. Because the energy shift of free electrons by laser fields, known as ponderomotive shift, is always repulsive, Rydberg states of alkali atoms cannot be trapped directly by an optical dipole force. On the other hand, in the case of AE(L)A, the polarizability of Rydberg states can be negative thanks to the contributions from ionic-core transitions. In fact, the trapping of Yb Rydberg atoms in an OT array has been demonstrated [64].
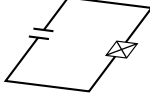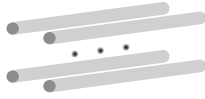
Thanks to these technical improvements, the performance of a neutral atom as a qubit is well competing with others. We summarize the performance of neutral atoms, superconducting circuits, and trapped ions for quantum computing in Table 1.2.

1.3 Nondestructive detection of atoms

For the site-resolved imaging of atoms, fluorescence of atoms by irradiating a resonant light is used generally. This causes a considerable heating and losses from the trap. Atoms in an optical lattice, especially, requires additional elaborate cooling procedures in a deep optical lattice during the imaging to prevent hoppings and losses of atoms. Even with the cooling of the atoms in an optical lattice site, the imaging fidelity is not perfect [3, 5, 6].

If one can measure the number of atoms without of the change of internal states except projections to the measurement basis, one can study the subsequent quantum many-body dynamics starting from the product state of the fixed numbers of atoms as a result of the atom-number projective measurement. An example of interesting quantum many-body dynamics is the quantum critical behavior of the Bose-Hubbard systems influenced by measurement backaction [71] and the creation of a strong correlation with feedback control [72].

Table 1.2: Comparisons of physical system: neutral atoms, superconduciting circuits, and trapped ions.

	Neutral atoms	Superconducting circuits	Trapped ions
Single-qubit gate fidelity	99.7% [38]	>99% [65]	99.99% [66]
Two-qubit gate fidelity	99.1% [38]	99.7% [67]	99.94% [68]
Operation time	~1 μs	10–50 ns	3–50 μs
T_1	60 s [39]	2 ms [69]	5500 s [70]
T_2	42 s [39]	1 ms [69]	4200 s [70]
Number of physical qubits	256 [26]	127 (IBM)	32 (Ion Q)

From a technical viewpoint, realization of the nondestructive limit of the imaging of single atoms relaxes the crucial requirement of incorporating an elaborate cooling scheme for an extremely deep potential. We note that nondestructive monitoring of quantum dynamics of cold atoms in a cavity quantum electrodynamics setup using a scanning microscope is recently proposed [73,74].

One may expect that the dispersive method using off-resonant probe light such as a Faraday effect can detect atoms without photon absorption by taking a sufficiently large detuning. However, it has been discussed that both measurements using resonant and off-resonant light have the same sensitivity for an optically thin sample for a given extent of absorption [75–77]. This is because of the existence of the shot noise in the probe light in the interferometric measurement of the dispersive method. Thus far, there is no quantitative discussion regarding the detection limit of a single atom under the condition of quantum gas microscopy in which the light can be efficiently collected by an objective lens with a high numerical aperture (NA).

1.4   This work

In the first part of this work, we focus on Yb atoms and its long-lived metastable $^3P_2$ state toward the high-fidelity quantum computing in an OT array. In this thesis, we present an experimental system for Yb Rydberg atom arrays featuring internal state manipulation between the ground $^1S_0$ and the $^3P_2$ states, and single-photon excitation from the $^3P_2$ to Rydberg states.

We trap single ^{174}Yb atoms in arrays of optical tweezers generated by a pair of acousto-optic deflectors (AODs). High-sensitive imaging of trapped single atoms is performed using the narrow-line $^1S_0 \leftrightarrow {}^3P_1$ transition, yielding 95% of imaging fidelity. The trapped single atoms in one dimension (1D) and two dimension (2D) are dynamically rearranged to defect-free single atom arrays with a fast feedback system. Using this system, we succeed in high-resolution $^1S_0 \leftrightarrow {}^3P_2$ laser spectroscopy for single Yb atoms. We also successfully demonstrate single-photon excitation

to a Rydberg state from the metastable $^3P_2$ state for single atoms in optical tweezers. In addition, we perform a systematic laser spectroscopy for Rydberg states using evaporatively cooled atoms, in which we newly observe a series of $(6s)(nd)^3D_3$ states ranging n = 65–80. This work offers an important step towards the realization of scalable systems for versatile quantum simulation and computation applications using Yb atom tweezer arrays.

In the second part, we also propose novel schemes that enables nondestructive atom detection, thus evading higher-band excitation and change of the internal degrees of freedom. We first discuss the limitation of detection of single atoms by a dispersive Faraday effect. We show that the photon absorption of the probe beam cannot be ignored to obtain a signal-to-noise ratio greater than unity even under an ideal condition with an unity NA, which is reminiscent of the result for an optically thin sample [75–77].

To overcome this limitation, we propose two schemes. The first is to utilize the magic-wavelength condition of the optical lattice for the transition of probing. The tight confinement in a Lamb-Dicke regime provides optical transitions mostly between states with the same vibrational quantum number in the optical lattice sites, thus satisfying the "nondestructive" condition. This is only applicable for atoms in the ground state without any spin degrees of freedom, such as a bosonic isotope of two-electron atoms. The second is a scanning-type quantum gas microscope with a confocal configuration with the use of a broadband squeezed vacuum [78–81]. Squeezed light has been used to reduce the shot noise [78]. It has been considered to be incorporated into a gravitational wave detector to beat the standard quantum limit [82]. It has also been shown to be an important resource of spectroscopy [81], biological measurement [83], magnetometry [79,80], and continuous-variable quantum information processing [84]. Utilizing the squeezed vacuum and heterodyne detection of scattered light from the atoms during the Faraday process, we achieve a signal-to-noise ratio greater than one while suppressing the light absorption and associated higher-band excitations. A scanning microscope with a confocal configuration is necessary to avoid effective losses on the squeezed state due to the branching of the spatial distribution of the light and mode-mismatch between the squeezed light and a local oscillator (LO) in the heterodyne detection. We discuss a system of two-electron atoms in metastable states as a realistic example of the application of the proposed scheme, enabling spin-sensitive nondestructive observation of a SU(N) Fermi-Hubbard model. This work opens the possibility for non-destructive observation of quantum dynamics of quantum many-body system, especially in an optical lattice.

1.5   Outline

This thesis is structured as follows:

In chapter 2, several fundamental theories of atomic transitions are described. We derive the multipole expansion of the laser-atom interactions and selection rules including M2 transitions such as the $^1S_0 \leftrightarrow ^3P_2$ transition of bosonic isotopes of AE(L)A. Transfers of the center-of-mass motion by optical transitions and its applications to cooling of atoms are also discussed.

In chapter 3, properties of Yb atoms and Rydberg states are summarized. We describe basic

aspects of Yb atoms and its energy levels regarding our experiments. We also describe basics of Rydberg states: scaling laws, a response to static electric fields, interactions between Rydberg states, unique features of Rydberg states of AE(L)As, and a brief introduction to the quantum defect theory.

In chapter 4, we explain the experimental apparatuses and techniques used in our work. We datail our vacuum chamber system integrating electrodes and a microchannel plate (MCP), an optical tweezer array generation system, and laser sources. We explain principles of absorption and fluorescence imaging, ionization detection, and trapping of single atoms.

Chapter 5 is devoted to the description of trapping and imaging of single atoms in an OT array. Optical setups, initial alignment, and procedure for getting images of single atoms are first present. We then show the result of single atom trapping and imaging in optical tweezer arrays, as well as cooling of atoms and OT array rearrangement by a feedback program.

In chapter 6, we present our results of spectroscopy of $^1S_0 \leftrightarrow {}^3P_2$ and $^3P_2 \leftrightarrow (6s)(nl)$ Rydberg states. We perform sideband-resolved spectroscopy of $^1S_0 \leftrightarrow {}^3P_2$ $m_J = 0$ for single atoms which could lead to cooling of atoms to their motional ground state. Single-photon excitation of single atoms to Rydberg states is also demonstrated. We further report our observation of complex spectra of D-series Rydberg states, including newly observed $^3D_3$ state.

In chapter 7, our proposal of two schemes for realization of nondestructive detection of single atoms, especially in an optical lattice, is present. We formulate the relation between the signal-to-noise ratio and photon absorption of Faraday imaging, and show that the detection of atoms without photon absorption is possible with the aid of a squeezed vacuum state. The other scheme which does not excite atoms to higher band using a magic wavelength optical trap for the imaging transition is also present. We finally discuss the feasibility of our scheme using Yb atoms.

In the final chapter of this thesis, we summarize our results and outlooks for the future experiments toward high-fidelity, scalable, and universal quantum computing.

Atomic transitions

2.1 Multipole transitions

In this section, we derive the multipole expansion of the laser–atom interaction and the selection rule of atomic transitions. The discussion in this section is based on references [85–87].

2.1.1 Multipole expansion of atom–laser interaction

A hamiltonian of the internal state of an atom interacting with an electromagnetic field which is given by a vector potential $\boldsymbol{A}$ is given by

$$\mathcal{H} = \frac{1}{2m}\left(\boldsymbol{p} - e\boldsymbol{A}\right)^2 + V(\boldsymbol{r}) \tag{2.1}$$

$$= \underbrace{\frac{\boldsymbol{p}^2}{2m} + V(\boldsymbol{r})}_{\rightarrow \mathcal{H}_{\mathrm{A}}} + \underbrace{\frac{(e\boldsymbol{A})^2}{2m}}_{\rightarrow \mathcal{H}_{\mathrm{F}}} - \underbrace{\frac{e}{2m}\left(\boldsymbol{p}\cdot\boldsymbol{A} + \boldsymbol{A}\cdot\boldsymbol{p}\right)}_{\rightarrow \mathcal{H}_{\mathrm{AF}}}, \tag{2.2}$$

where m, e, $\boldsymbol{r}$, $\boldsymbol{p}$ is the mass, charge, the position operator and the momentum operator of the electron, respectively. V denotes the potential which the valence electron feels from the nuclear. Here we consider the case the atom is interacting with the laser which have the wavenumber $\boldsymbol{k}$ and the polarization unit vector $\hat{\boldsymbol{e}}_\lambda$. $\boldsymbol{A}$ is then written as

$$\boldsymbol{A} = A_0\hat{\boldsymbol{e}}_\lambda \exp(-\mathrm{i}\boldsymbol{k}\cdot\boldsymbol{r}). \tag{2.3}$$

The hamiltonian of the atom–field interaction thus becomes

$$\mathcal{H}_{\mathrm{AF}} = -\frac{e}{2m}\left(\boldsymbol{p}\cdot\boldsymbol{A} + \boldsymbol{A}\cdot\boldsymbol{p}\right) \tag{2.4}$$

$$= -\frac{e}{2m}\left(-\hbar(\boldsymbol{k}\cdot\boldsymbol{A}) + 2\boldsymbol{A}\cdot\boldsymbol{p}\right) \tag{2.5}$$

$$= -\frac{e}{m}\boldsymbol{A}\cdot\boldsymbol{p}. \tag{2.6}$$

Here we used the relation $\boldsymbol{k}\cdot\hat{\boldsymbol{e}}_\lambda = 0$. In the following discussion, we omit the sign -1 in Eq. (2.6) for the sake of simplicity without loss of generality. Using spherical harmonics $Y_l^m(\hat{\boldsymbol{n}}) = \langle \hat{\boldsymbol{n}}|lm\rangle$,

$\exp(-i\mathbf{k} \cdot \mathbf{r})$ is expanded as

$$\exp(-i\mathbf{k} \cdot \mathbf{r}) = 4\pi \sum_{l=0}^{\infty} \sum_{m=-l}^{l} (-i)^l g_l(kr) Y_l^{m*}(\hat{\mathbf{r}}) Y_l^m(\hat{\mathbf{k}}), \tag{2.7}$$

where $\hat{\mathbf{r}}, \hat{\mathbf{k}}$ denotes unit vectors parallel to $\mathbf{r}, \mathbf{k}$, respectively. $g_l(x)$ denotes the spherical bessel function which is equivalent to

$$g_l(x) = (-x)^l \left(\frac{1}{x} \frac{d}{dx} \right)^l \frac{\sin x}{x}. \tag{2.8}$$

Here let us introduce several formulae of spherical tensors. We denote a rank-k spherical tensor as $\mathbf{T}_k$ and its m-th component as $\mathbf{T}_k^m$. A product of two spherical tensors $U_l, V_{l'}$ is given by

$$\{\mathbf{U}_l \otimes \mathbf{V}_{l'}\}_j^M = \sum_{m,m'} \langle l\ m\ ;\ l'\ m'\ |\ j\ M \rangle \mathbf{U}_l^m \mathbf{V}_{l'}^{m'}. \tag{2.9}$$

$\langle l\ m\ ;\ l'\ m'\ |\ j\ M \rangle$ is the Clebsch–Gordan coefficient (CG coefficient). The CG coefficients satisfy the following orthogonality and symmetry relations:

$$\sum_{mm'} \langle\ j\ M\ |\ l\ m\ ;\ l'\ m' \rangle \langle l\ m\ ;\ l'\ m'\ |\ j'\ M' \rangle = \delta_{jj'} \delta_{MM'}. \tag{2.10}$$

$$\langle l\ m\ ;\ l'\ m'\ |\ j'\ M' \rangle = (-1)^{l+l'-j} \langle l'\ m'\ ;\ l\ m\ |\ j'\ M' \rangle \tag{2.11}$$

$$= (-1)^{l+l'-j} \langle l\ -m\ ;\ l'\ -m'\ |\ j'\ -M' \rangle \tag{2.12}$$

$$= \langle l'\ -m'\ ;\ l\ -m\ ;|\ j'\ -M' \rangle \tag{2.13}$$

Note that all the CG coefficients takes real values. Using Eq. (2.10), the inverse relation of Eq. (2.9) is derived such that

$$\mathbf{U}_l^m \mathbf{V}_{l'}^{m'} = \sum_{jM} \langle\ l\ m\ ;\ l'\ m'\ |\ j\ M \rangle \{\mathbf{U}_l \otimes \mathbf{V}_{l'}\}_j^M. \tag{2.14}$$

From the above relations and the conjugation relation of the sphecical harmonics $Y_l^{m*} = (-1)^m Y_l^{-m}$,

the interaction hamiltonian Eq. (2.6) becomes, using the spherical bases $\hat{e}_q$ [1],

$$\mathcal{H}_{AF} / 4\pi \frac{e}{m} A_0 = \sum_{q=-1}^{1} \sum_{lm} (-i)^l (-1)^{m+q} g_l(kr) Y_l^{-m}(\hat{r}) Y_l^m(\hat{k}) p_q (\hat{e}_\lambda)_{-q} \tag{2.16}$$

$$= \sum_{qlm} \sum_{jM} (-i)^l (-1)^{m+q} g_l(kr) \langle l -m ; 1 q \mid j M \rangle Y_l^m(\hat{k}) \{Y_l(\hat{r}) \otimes p\}_j^M (\hat{e}_\lambda)_{-q} \tag{2.17}$$

$$= \sum_{qlm} \sum_{jM} (-1)^{m+q} \langle l m ; 1 -q \mid j -M \rangle T_{j,l}^M(r) Y_l^m(\hat{k}) (\hat{e}_\lambda)_{-q} \tag{2.18}$$

$$= \sum_{qlm} \sum_{jM} (-1)^{m+q} T_{j,l}^M(r) \langle l -m ; 1 -q \mid j -M \rangle Y_l^{-m}(\hat{r}) (\hat{e}_\lambda)_{-q} \tag{2.19}$$

$$\tag{2.20}$$

Here we defined a rank-j tensor $T_{j,l}(r)$ as following:

$$T_{j,l}(r) = (-i)^l \{(-1)^{l+1-j} g_l(kr) Y_l(\hat{r}) \otimes p\}_j \tag{2.21}$$

$$= \frac{1}{2}(-i)^l \left(\{(-1)^{l+1-j} g_l(kr) Y_l(\hat{r}) \otimes p\}_j + \{p \otimes g_l(kr) Y_l(\hat{r})\}_j \right) \tag{2.22}$$

The second equation can be derived by using Eq. (2.4) instead of Eq. (2.6). The irreducible tensors can also be expressed in terms of the spherical harmonic vectors

$$Y_{j,l}^M(\hat{r}) = \sum_{m_1,m_2} \langle l m_1 ; 1 m_2 \mid j M \rangle Y_j^M(\hat{r}) \hat{e}_{m_1}, \tag{2.23}$$

of which the spherical basis component is

$$\left(Y_{j,l}^M(\hat{r})\right)_q = \hat{e}_q \cdot Y_{j,l}^M(\hat{r}) = \sum_{m_1} (-1)^q \langle l m_1 ; 1 -q \mid j M \rangle Y_j^M(\hat{r}), \tag{2.24}$$

which is useful in the discussion of the angular momentum transitions [88]. Taking into account the triangular condition and the conservation rule of the angular momentum, CG coefficients in Eq. (2.19) vanishes unless $L = l, l \pm 1$ and $m + q = M$. Equation (2.19) thus becomes

$$\sum_{q,M} \sum_{j=0}^{\infty} \sum_{l=j-1}^{j+1} (-1)^q (-1)^M (-1)^{l+1-j} T_{j,l}^M (Y_{j,l}^{-M}(\hat{k}))_q (\hat{e}_\lambda)_{-q} \tag{2.25}$$

$$= \sum_{j=0}^{\infty} \sum_{l=j-1}^{j+1} (-1)^{l+1-j} T_{j,l} \cdot \left(\hat{e}_\lambda \cdot Y_{j,l}(\hat{k})\right). \tag{2.26}$$

$$\tag{2.27}$$

---

[1]The inner product of two vectors a and b in the spherical basis is given as

$$a \cdot b = \sum_q (-1)^q a_q b_{-q}. \tag{2.15}$$

We define spherical vectors $\boldsymbol{Y}_j^{(E)}$ and $\boldsymbol{Y}_j^{(M)}$ as

$$\boldsymbol{Y}_j^{(E)}(\hat{\boldsymbol{k}}) = \sqrt{\frac{j+1}{2j+1}}\boldsymbol{Y}_{j,j-1}^m(\hat{\boldsymbol{k}}) + \sqrt{\frac{j}{2j+1}} + \boldsymbol{Y}_{j,j+1}^m(\hat{\boldsymbol{k}}) \tag{2.28}$$

$$\boldsymbol{Y}_j^{(M)} = \boldsymbol{Y}_{j,j}(\hat{\boldsymbol{k}}) \tag{2.29}$$

which corresponds to electric and magnetic transitions. With the aid of the relation:

$$\hat{\boldsymbol{k}}Y_j(\hat{\boldsymbol{k}}) = \sqrt{\frac{j}{2j+1}}\boldsymbol{Y}_{j,j-1}(\hat{\boldsymbol{k}}) - \sqrt{\frac{j}{2j+1}}\boldsymbol{Y}_{l,j+1}(\hat{\boldsymbol{k}}) \tag{2.30}$$

and Eq. (2.28), we find

$$\boldsymbol{Y}_{j,j-1}(\hat{\boldsymbol{k}}) = \sqrt{\frac{j+1}{2j+1}}\boldsymbol{Y}_j^{(E)}(\hat{\boldsymbol{k}}) + \sqrt{\frac{j}{2j+1}}\hat{\boldsymbol{k}}Y_j(\hat{\boldsymbol{k}}) \tag{2.31}$$

$$\boldsymbol{Y}_{j,j+1}(\hat{\boldsymbol{k}}) = \sqrt{\frac{j}{2j+1}}\boldsymbol{Y}_j^{(E)}(\hat{\boldsymbol{k}}) - \sqrt{\frac{j+1}{2j+1}}\hat{\boldsymbol{k}}Y_j(\hat{\boldsymbol{k}}). \tag{2.32}$$

Using this, $\mathcal{H}_{\mathrm{AF}}$ can be decomposed to two parts corresponding to electric and magnetic transitions:

$$\mathcal{H}_{\mathrm{AF}} \,/\, 4\pi\frac{e}{m}A_0 = \sum_{j=0}^{\infty} \underbrace{\left(\sqrt{\frac{j+1}{2j+1}}\boldsymbol{T}_{j,j-1} + \sqrt{\frac{j}{2j+1}}\boldsymbol{T}_{j,j+1}\right)\cdot(\hat{\boldsymbol{e}}_\lambda\cdot\boldsymbol{Y}_j^{(E)}(\hat{\boldsymbol{k}}))}_{\to\mathcal{H}_j^{(E)}} \tag{2.33}$$

$$+ \sum_{j=0}^{\infty} \underbrace{\left(-\boldsymbol{T}_{j,j}\cdot(\hat{\boldsymbol{e}}_\lambda\cdot\boldsymbol{Y}_j^{(M)}(\boldsymbol{k}))\right)}_{\to\mathcal{H}_j^{(M)}}. \tag{2.34}$$

2.1.2   Electric and magnetic multipole operators

Let us confirm that the tensor operator in Eqs. (2.33) and (2.34) correspond to the electric and magnetic 2^j-pole operators respectively, under the long-wave approximation: $kr \ll 1$. Using the expansion of $g_l(x)$

$$g_l(x) = \frac{x^l}{(2l+1)!!} + O(x^{l+1}), \tag{2.35}$$

and a rank-l tensor obtained by the "power" of $\boldsymbol{r}$ [89]:

$$\{\boldsymbol{r}\}_l \equiv \{\cdots\{\{\boldsymbol{r}\otimes\boldsymbol{r}\}_2\otimes\boldsymbol{r}\}_3\cdots\}_l = \sqrt{\frac{4\pi l!}{(2l+1)!!}}r^l Y_l(\hat{\boldsymbol{r}}), \tag{2.36}$$

and by taking the lowest order with respect to r, the tensor operators in Eq. (2.33) become

$$\sqrt{\frac{j+1}{2j+1}}\boldsymbol{T}_{j,j-1} + \sqrt{\frac{j}{2j+1}}\boldsymbol{T}_{j,j+1} \tag{2.37}$$

$$\simeq \frac{(-\mathrm{i}k)^{j-1}}{2}\sqrt{\frac{j+1}{2j+1}}\sqrt{\frac{(2j-1)!!}{4\pi(j-1)!}}\frac{1}{(2j-1)!!}\left(\{\boldsymbol{p}\otimes\{\boldsymbol{r}\}_{j-1}\}_j + \{\{\boldsymbol{r}\}_{j-1}\otimes\boldsymbol{p}\}_j\right), \tag{2.38}$$

using Eq. 2.22. The transition matrix element between the initial state i and the final state f can be calculated as following (ignoring the constant factor temporarily)

$$\langle f| \left(\{ \boldsymbol{p} \otimes \{ \boldsymbol{r} \}_{j-1} \}_j + \{ \{ \boldsymbol{r} \}_{j-1} \otimes \boldsymbol{p} \}_j \right) |i\rangle \tag{2.39}$$

$$= \frac{m}{i\hbar} \langle f| \left(\{ [\boldsymbol{r}, \mathcal{H}_A] \otimes \{ \boldsymbol{r} \}_{j-1} \}_j + \{ \{ \boldsymbol{r} \}_{j-1} \otimes [\boldsymbol{r}, \mathcal{H}_A] \}_j \right) |i\rangle \tag{2.40}$$

$$= -\frac{m}{i\hbar} \langle f| \left(\{ (\mathcal{H}_A \boldsymbol{r}) \otimes \{ \boldsymbol{r} \}_{j-1} \}_j - \{ \{ \boldsymbol{r} \}_{j-1} \otimes (\boldsymbol{r}\mathcal{H}_A) \}_j \right) |i\rangle \tag{2.41}$$

$$+ \frac{m}{i\hbar} \langle f| \left(\{ (\boldsymbol{r}\mathcal{H}_A) \otimes \{ \boldsymbol{r} \}_{j-1} \}_j - \{ \{ \boldsymbol{r} \}_{j-1} \otimes (\mathcal{H}_A \boldsymbol{r}) \}_j \right) |i\rangle \tag{2.42}$$

$$= -\frac{m}{i\hbar} \langle f| \left(E_f \{ \boldsymbol{r} \otimes \{ \boldsymbol{r} \}_{j-1} \}_j - E_i \{ \{ \boldsymbol{r} \}_{j-1} \otimes \boldsymbol{r} \}_j \right) |i\rangle \tag{2.43}$$

$$= im\omega \langle f| \{ \boldsymbol{r} \}_j |i\rangle \tag{2.44}$$

Here we used a relation

$$\boldsymbol{p} = \frac{m}{i\hbar} [\boldsymbol{r}, \mathcal{H}_A]. \tag{2.45}$$

We used that $|f\rangle, |i\rangle$ are eigenstates of $\mathcal{H}_A$ with the eigenvalues E_f, E_i. We also used $\boldsymbol{p}^2 \{\boldsymbol{r}\}_j^M \propto \Delta \left(r^j Y_j^M(\hat{\boldsymbol{r}}) \right) = 0$ to eliminate Eq. (2.42). $\omega = (E_f - E_i)/\hbar$ is the energy gap between the state i and f. Equation (2.38) become

$$\frac{-(-i)^j}{2} \frac{cmk^j}{(2j+1)!!} \sqrt{j(j+1)} r^j Y_j(\hat{\boldsymbol{r}}) \tag{2.46}$$

$$= \frac{-(-i)^j}{2} \frac{cmk^j}{(2j-1)!!} \sqrt{\frac{j(j+1)}{4\pi(2j+1)}} Q_j^{(E)}, \tag{2.47}$$

where

$$Q_j^{(E)} \equiv \sqrt{\frac{4\pi}{2j+1}} r^j Y_j \tag{2.48}$$

is the electric 2^j-pole operator. We thus obtain

$$\langle f| \mathcal{H}_j^{(E)} |i\rangle = -\frac{(-ik)^j ceA_0}{2(2j-1)!!} \sqrt{\frac{j(j+1)}{4\pi(2j+1)}} \left(\hat{\boldsymbol{e}}_\lambda \cdot \boldsymbol{Y}_j^{(E)}(\hat{\boldsymbol{k}}) \right) \cdot \langle f| Q_j^{(E)} |i\rangle. \tag{2.49}$$

For magnetic part, the lowest order of tensor operator is

$$T_{j,j} = -\frac{(-ik)^j}{(2j+1)!!} \{ r^j Y_j(\hat{\boldsymbol{r}}) \otimes \boldsymbol{p} \}_j \tag{2.50}$$

$$= -\frac{(-ik)^j}{(2j+1)!!} r^j \boldsymbol{Y}_j^{(M)} \cdot \boldsymbol{p}. \tag{2.51}$$

By using a formula

$$\boldsymbol{Y}_j^{(M)} = \frac{1}{\sqrt{j(j+1)}} \boldsymbol{r} \times \nabla Y_j, \tag{2.52}$$

we obtain

$$T_{j,j} = -\frac{(-ik)^j}{(2j+1)!!} r^j \boldsymbol{Y}_j^{(M)} \cdot \boldsymbol{p} \tag{2.53}$$

$$= -\frac{(-ik)^j}{(2j+1)!!} \frac{r^j}{\sqrt{j(j+1)}} \left(\boldsymbol{r} \times \nabla Y_j\right) \cdot \boldsymbol{p} \tag{2.54}$$

$$= \frac{(-ik)^j}{(2j+1)!!} \frac{\boldsymbol{r} \times \boldsymbol{p}}{\sqrt{j(j+1)}} \cdot \nabla(r^j Y_j) \tag{2.55}$$

$$= \frac{(-ik)^j}{(2j-1)!!} \sqrt{\frac{j+1}{4\pi j(2j+1)}} Q_j^{(M)}, \tag{2.56}$$

where

$$Q_j^{(M)} \equiv \frac{1}{j+1} \sqrt{\frac{4\pi}{2j+1}} \boldsymbol{r} \times \boldsymbol{p} \cdot \nabla(r^j Y_j) \tag{2.57}$$

is the magnetic 2^j-pole moment. The transition matrix element become

$$\langle f | \mathcal{H}_j^{(M)} | i \rangle = \frac{(-ik)^j}{(2j-1)!!} \sqrt{\frac{j+1}{4\pi j(2j+1)}} \left(\hat{\boldsymbol{e}}_\lambda \cdot \boldsymbol{Y}_j^{(M)}(\hat{\boldsymbol{k}})\right) \cdot \langle f | Q_j^{(M)} | i \rangle. \tag{2.58}$$

The terms $\hat{\boldsymbol{e}}_\lambda \cdot \boldsymbol{Y}_j^{(E)}(\hat{\boldsymbol{k}})$ and $\hat{\boldsymbol{e}}_\lambda \cdot \boldsymbol{Y}_j^{(M)}(\hat{\boldsymbol{k}})$ in Eqs. (2.49) and (2.58) determines the selection rule of the transition which change the magnetic sublevel by M.

2.2 Optical Bloch equation

Let us consider two-level system composed of the ground state $|g\rangle$ and the excited state $|e\rangle$ with the energy gap $\hbar\omega_0$. When the system is interacting with the laser oscillating as $e^{i\omega_L t}$, the interaction couples the two states as following

$$\langle e | \mathcal{H}_{\text{AF}} | g \rangle = e^{i\omega_L t} \hbar\Omega/2 \tag{2.59}$$

$$\langle g | \mathcal{H}_{\text{AF}} | e \rangle = e^{-i\omega_L t} \hbar\Omega/2. \tag{2.60}$$

Ω is the coupling strength between the ground and the excited state, called **rabi frequency**. We note that we can choose Ω to be real by choosing appropriate relative phase between $|g\rangle$ and $|e\rangle$. The Schrödinger equation of the system is

$$i\frac{\partial}{\partial t} |\psi\rangle = \begin{pmatrix} 0 & e^{i\omega_L t}\Omega/2 \\ e^{-i\omega_L t}\Omega/2 & \omega_0 \end{pmatrix} |\psi\rangle \tag{2.61}$$

Equation (2.61) in the rotating frame with ω_L is more convenient:

$$i\frac{\partial}{\partial t} |\psi\rangle = \begin{pmatrix} 0 & \Omega/2 \\ \Omega/2 & -\Delta \end{pmatrix} |\psi\rangle, \tag{2.62}$$

where we defined the detuning of the laser $\Delta \equiv \omega_L - \omega_0$. In such a two-level system, the bloch sphere representation is useful. We express the density operator in terms of pauli matrices σ_i as

$$\rho = |\psi\rangle \langle\psi| = \frac{I + \sum_{i=x,y,z} \langle\sigma_i\rangle \sigma_i}{2}. \tag{2.63}$$

From Eq. (2.62), we can get the time evolution equation of $\langle\sigma_i\rangle$:

$$i\frac{d}{dt}\begin{pmatrix} \langle\sigma_x\rangle \\ \langle\sigma_y\rangle \\ \langle\sigma_z\rangle \end{pmatrix} = \begin{pmatrix} 0 & \Delta & 0 \\ -\Delta & 0 & -\Omega \\ 0 & \Omega & 0 \end{pmatrix}\begin{pmatrix} \langle\sigma_x\rangle \\ \langle\sigma_y\rangle \\ \langle\sigma_z\rangle \end{pmatrix} \tag{2.64}$$

$$= \begin{pmatrix} \Omega \\ 0 \\ -\Delta \end{pmatrix} \times \begin{pmatrix} \langle\sigma_x\rangle \\ \langle\sigma_y\rangle \\ \langle\sigma_z\rangle \end{pmatrix}, \tag{2.65}$$

meaning the rotation along the axis $\Omega\sigma_x - \Delta\sigma_z$ without any damping. The modulation frequency and depth is given by $\Omega_{\text{eff}} = \sqrt{\Delta^2 + \Omega^2}$ and $\Omega^2/\Omega_{\text{eff}}^2 = 1/(1 + \Delta^2/\Omega^2)$, respectively. In the more real picture, the non-unitary evolution due to the spontaneous emission from $|e\rangle$ to $|g\rangle$ should be taken into account. This damping term can be included in Eq. (2.65) as is shown in the following:

$$i\frac{d}{dt}\begin{pmatrix} \langle\sigma_x\rangle \\ \langle\sigma_y\rangle \\ \langle\sigma_z\rangle \end{pmatrix} = \begin{pmatrix} \Omega \\ 0 \\ -\Delta \end{pmatrix} \times \begin{pmatrix} \langle\sigma_x\rangle \\ \langle\sigma_y\rangle \\ \langle\sigma_z\rangle \end{pmatrix} - \begin{pmatrix} \gamma \\ \gamma \\ \Gamma \end{pmatrix} \cdot \begin{pmatrix} \langle\sigma_x\rangle \\ \langle\sigma_y\rangle \\ \langle\sigma_z\rangle + 1 \end{pmatrix}, \tag{2.66}$$

where $\gamma = \Gamma/2$ and Γ is the transverse decay rate and the longitudinal decay rate, respectively. Γ corresponds to the usual decay rate of spontaneous emission, namely the inverse of the lifetime of the excited state. In this thesis we omit the detailed derivation of the damping term[2]. Equation (2.66) is called the **Optical Bloch Equation** (OBE).

The OBE relaxes to a steady state for $t \gg 1/\Gamma$. Usually we are interested in the population of the excited state ρ_{ee} in the steady state, which is given by

$$\rho_{ee}(t \to \infty) = \frac{1}{2}\frac{\Omega^2/\Gamma^2}{1 + (2\Delta/\Gamma)^2 + 2\Omega^2/\Gamma^2} \tag{2.67}$$

$$= \frac{1}{2}\frac{I/I_{\text{sat}}}{1 + (2\Delta/\Gamma)^2 + I/I_{\text{sat}}}, \tag{2.68}$$

where we used the relation between the saturation intensity I_{sat} and the intensity of the applied laser I: $I/I_{\text{sat}} = 2\Omega^2/\Gamma^2$. The photon scattering rate is obtained from Eq. (2.68) as

$$R_{\text{sc}} = \Gamma\rho_{ee}(t \to \infty) = \frac{\Gamma}{2}\frac{I/I_{\text{sat}}}{1 + (2\Delta/\Gamma)^2 + I/I_{\text{sat}}} \tag{2.69}$$
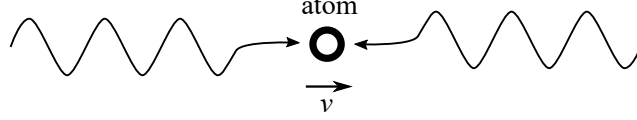
Figure 2.1: Molasses cooling configuration of an atom: Two counter-propagating lasers are irradiated to atom moving in one-dimensional free space.

2.3 Center-of-mass motion associated with optical transitions

2.3.1 Free atoms — Doppler cooling limit

Let us consider an two-level atom moving in free one-dimensional space with a momentum p. When two counter propagating lasers with detuning Δ and intensity I are irradiated (Fig. 2.1), the absorption of this light gives momentum to the atom in time dt

$$(dp)_{\mathrm{abs}} = \hbar k \left(R_{\mathrm{sc}}(v) - R_{\mathrm{sc}}(-v) \right) dt, \tag{2.70}$$

where k is a wavenumber of the photon, $v = p/m$ is the velocity of the atom, and

$$R_{\mathrm{sc}}(v) = \frac{\Gamma}{2} \frac{I/I_{\mathrm{sat}}}{1 + (2(\Delta - kv)/\Gamma)^2 + I/I_{\mathrm{sat}}} \tag{2.71}$$

is the photon scattering rate considering the doppler shift. When the dopple shift is small enough ($kv \ll \Delta$), R_{sc} can be expanded up to the first order of v as

$$R_{\mathrm{sc}}(v) = R_{\mathrm{sc}}(0) + R'_{\mathrm{sc}}(0)v \tag{2.72}$$

$$R'_{\mathrm{sc}} = \frac{4(\Delta/\Gamma)I/I_{\mathrm{sat}}}{\left(1 + (2\Delta/\Gamma)^2 + I/I_{\mathrm{sat}}\right)^2} \tag{2.73}$$

From Eq. (2.70), we obtain the equation for kinetic energy of the atom $E = p^2/2m$ as

$$(dE)_{\mathrm{abs}} = \frac{\left(dp^2\right)_{\mathrm{abs}}}{2m} = \frac{p}{m} \left(dp\right)_{\mathrm{abs}} = \frac{32(\Delta/\Gamma)I/I_{\mathrm{sat}}}{\left(1 + (2\Delta/\Gamma)^2 + I/I_{\mathrm{sat}}\right)^2} \frac{E_r}{\hbar} E dt. \tag{2.74}$$

E_r denotes **recoil energy** by a photon: $E_r \equiv (\hbar k)^2/2m$.

On the other hand, excited atoms spontaneously emit photons for random direction, resulting in heating of atom given by

$$(dE)_{\mathrm{em}} = 2E_r(R_{\mathrm{sc}}(v) + R_{\mathrm{sc}}(-v))dt \tag{2.75}$$

$$= 4E_r \frac{\Gamma}{2} \frac{I/I_{\mathrm{sat}}}{1 + (2\Delta/\Gamma)^2 + I/I_{\mathrm{sat}}} dt. \tag{2.76}$$

Adding Eq. (2.73) and Eq. (2.76), we obtain the formula for the time evolution of the energy:

$$\frac{dE}{dt} = 2E_r \frac{I/I_{\mathrm{sat}}}{1 + (2\Delta/\Gamma)^2 + I/I_{\mathrm{sat}}} \times \left(\Gamma + \frac{16(\Delta/\Gamma)(E/h)}{1 + (2\Delta/\Gamma)^2 + I/I_{\mathrm{sat}}} \right). \tag{2.77}$$

---

[2]See [90] for the detailed derivation.

In steady state the energy become

$$E = -\frac{\hbar\Gamma}{16(\Delta/\Gamma)}\left(1 + (2\Delta/\Gamma)^2 + I/I_{\text{sat}}\right),\tag{2.78}$$

which takes the minimum value

$$E = \frac{\hbar\Gamma}{4}\tag{2.79}$$

when $\Delta = -\Gamma/2$ and $I/I_{\text{sat}} \to 0$. The corresponding temperature

$$T_D = \frac{\hbar\Gamma}{2k_B}\tag{2.80}$$

is called the **Doppler cooling limit**. We used the relation between the energy and temperature of one-dimensional monatomic gas: $E = k_B T/2$. The same discussion holds for higher dimensions.

2.3.2 Strongly bound atoms

When an atom is bound to an trap, the center-of-mass (COM) motion is quantized. For the sake of simplicity, we consider an atom in one-dimensional harmonic trap with a trapping frequency ν. The hamiltonian for the COM motion is

$$V = \frac{p^2}{2m} + \frac{m\nu}{2}x^2\tag{2.81}$$

$$= a^\dagger a + \frac{1}{2},\tag{2.82}$$

where we have defined the lowering and the raising operator $a, a^\dagger$ according to

$$x = \frac{1}{\sqrt{2m\nu}}(a + a^\dagger) \equiv x_0(a + a^\dagger),\tag{2.83}$$

$$p = i\sqrt{\frac{m\nu}{2}}(a - a^\dagger) \equiv p_0(a - a^\dagger).\tag{2.84}$$

The transition matrix element between $|g, n_g\rangle$ and $|e, n_e\rangle$ is given by

$$\langle e, n_e| \mathcal{H}_{\text{AF}} |g, n_g\rangle = \Omega_0 \langle n_g| e^{ikx} |n_e\rangle\tag{2.85}$$

$$= \Omega_0 \langle n_g| e^{ikx_0(a+a^\dagger)} |n_e\rangle.\tag{2.86}$$

Ω_0 is the rabi frequency of the career transitions ($n_e = n_g$). The constant factor in exponential $\eta \equiv kx_0 = \sqrt{E_r/\hbar\nu}$ is called the **Lamb-Dicke factor**. When $\eta \ll 1$ is satisfied, by taking up to the first order of η of Eq. (2.86), we obtain

$$\Omega_0 \langle n_g| e^{ikx_0(a+a^\dagger)} |n_e\rangle \simeq \Omega_0 \langle n_g| \left(1 + i\eta(a + a^\dagger)\right) |n_e\rangle = \begin{cases} \Omega_0 & (n_e = n_g) \\ i\sqrt{n_e}\eta\Omega_0 & (n_e = n_g + 1) \\ i\sqrt{n_g}\eta\Omega_0 & (n_e = n_g - 1) \\ 0 & (\text{otherwise}) \end{cases},\tag{2.87}$$

which means the transition to add or remove only one phonon is allowed except the career transition, and their strength is scaled by the Lamb–Dicke factor to the career transition. We call this regime the Lamb–Dicke regime. Without approximation, exact form of the transition matrix is described as [91]

$$\langle n_g | e^{i\eta(a+a^\dagger)} | n_e \rangle = e^{-\eta^2/2} \eta^{\Delta n} \sqrt{\frac{n_<!}{n_>!}} L_{n_<}^{\Delta n}(\eta^2),$$ (2.88)

where we defined $n_< = \min(n_g, n_e)$, $n_> = \max(n_g, n_e)$, and $\Delta n = |n_e - n_g|$. $L_n^\alpha(x)$ denotesLaguerre polynomial

$$L_n^\alpha(x) = \sum_{m=0}^{n} (-1)^m \binom{n+\alpha}{n-\alpha} \frac{x^m}{m!}.$$ (2.89)

Note that we have assumed the trap potential does not depend on atom's internal state in the above calculation, but this assumption is not always true in case of optical trapping.

When the linewidth Γ of the transition between $|g\rangle$ and $|e\rangle$ is narrow enough to resolve the trapping frequency, the cycle of the transition can cool atoms to below the Doppler cooling limit. The cooling rate A_- and the heating rate A_+ can be derived as

$$A_\pm = \eta^2 \left(W(\Delta) + W(\mp\Delta) \right),$$ (2.90)

using the scattering rate $W(\Delta)$ at laser detuning Δ [92]. $W(\Delta)$ for the two-level system is given by $\Gamma \rho_{ee}$, where ρ_{ee} is deduced in Eq. (2.68). Here we assumed that atoms are precooled to $\eta^2 \bar{n} \leq 1$ region, where $\bar{n}$ denotes the mean occupation number of the motional states. Equation for time-evolution of $\bar{n}$ is expressed as

$$\frac{d}{dt}\bar{n} = -(A_- - A_+)\bar{n} + A_+.$$ (2.91)

In the cooling situation $(A_- - A_+) > 0$, $\bar{n}$ approaches to the steady state given by

$$\bar{n}_f = \frac{A_+}{A_- - A_+} = \frac{W(\Delta) + W(\Delta - \nu)}{W(\Delta + \nu) - W(\Delta - \nu)}.$$ (2.92)

For sideband resolved cooling situation $\Gamma \ll \nu$, this results in the sub-Doppler cooling $\bar{n}_f \ll 1$, while it recovers the Doppler cooling limit $\bar{n}_f \nu \simeq \Gamma/2$ for $\Gamma \gtrsim \nu$.

Ytterbium and Rydberg states

3.1 Ytterbium

3.1.1 Basic properties of Ytterbium

Ytterbium is one of the lanthanoide atoms with the atomic number $Z = 70$. Its electron configuration consists of complete internal shells and two valence electrons, written as $[\mathrm{Xe}]4f^{14}6s^2$ (Figure 3.1). The existence of two valence electrons makes the nature of Yb quite different from that of alkali atoms as well as alkaline-earth atoms, positively for applications to quantum computing, as is described in section 1.2.
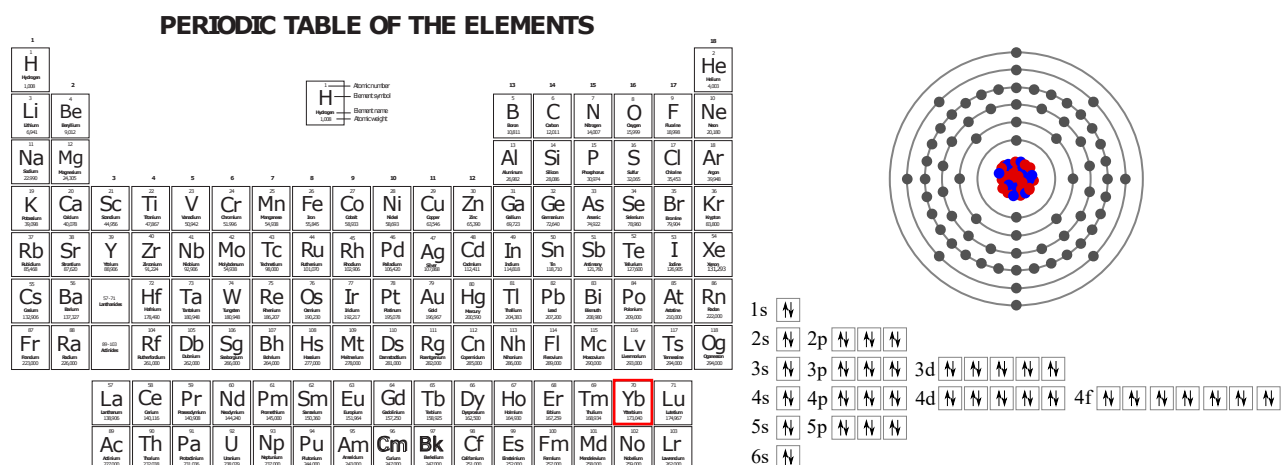
Figure 3.1: (Left) Periodic table of elements. Ytterbium in the lanthanoid series is highlighted by a red square. This periodic table is downloaded from https://www.periodictable.co.za. (Right) Electron configuration of ytterbium.

Naturally occurring Yb has seven stable isotopes with mass number 168, 170, 171, 173, 174 and 176. Because even/odd mass number corresponds to boson/fermion, Yb has five bosonic isotopes and two fermionic isotopes. Regarding to nuclear spin, even isotopes has even number protons

and neutrons, and therefore the nuclear becomes spinless ($I = 0$), while the odd isotopes have half integer nuclear spins. Especially, ^{171}Yb has 1/2 nuclear spin, which is why this isotope is thought to be desirable for the realization of nuclear spin qubit because it spans minimum qubit manifold, no need to isolate them from other spin components.

Mass number	Natural abundance (%)	Nuclear spin	Statistics
168	0.13	0	Boson
170	3.05	0	Boson
171	14.3	1/2	Fermion
172	21.9	0	Boson
173	16.12	5/2	Fermion
174	31.8	0	Boson
176	12.7	0	Boson

3.1.2 Energy structure and transitions

The energy levels of Yb is shown in Fig. 3.2. In the case of heavy atoms such as Yb, the spin–orbit coupling becomes not negligible that perturbs and mixes pure LS-coupling eigenstates, which is why Yb has intercombination transition ($\Delta S = 1$) which is strictly forbidden in the LS-coupling picture, in addition to dipole-allowed transitions such as $^1S_0$–$^1P_1$. As a consequence Yb has rich availability of optical transitions compared with alkali atoms. In this section properties of optical transitions used in our experiments are summarised.

3.1.2.1 $(6s)^2\,^1S_0 \leftrightarrow (6s)(6p)^1P_1$

An electric dipole-allowed transition (E1 transition) with the wavelength $\lambda = 398.9$ nm and the natural linewidth $\gamma = 2\pi \times 29$ MHz [95]. Thanks to its broad linewidth and resulting strong radiative pressure, this transition is useful for initial cooling of hot atomic beams, absorption imaging, and fluorescence imaging. This $^1P_1$ state slightly[1] decays to $(5d)(6s)\,^3D_1$ and $(5d)(6s)\,^3D_2$, which makes the transition not completely cyclic.

In our experiments, this transition is used for the Zeeman slowing and the absorption imaging.

3.1.2.2 $(6s)^2\,^1S_0 \leftrightarrow (6s)(6p)\,^3P_1$

The transition is essentially a closed transition and have the wavelength $\lambda = 555.8$ nm and the natual linewidth $\gamma = 2\pi \times 182.4$ kHz [97]. The presence of the spin-orbit coupling makes the state mixed of pure LS-coupling eigenstates denoted as $|^1P_1^0\rangle$ and $|^3P_1^0\rangle$, namely

$$|^1P_1\rangle = \alpha\,|^1P_1^0\rangle + \beta\,|^3P_1^0\rangle \,, \tag{3.1}$$

$$|^3P_1\rangle = \alpha\,|^3P_1^0\rangle - \beta\,|^1P_1^0\rangle \,, \tag{3.2}$$

---

[1]The branching ratio is roughly 10^{-7} [96].
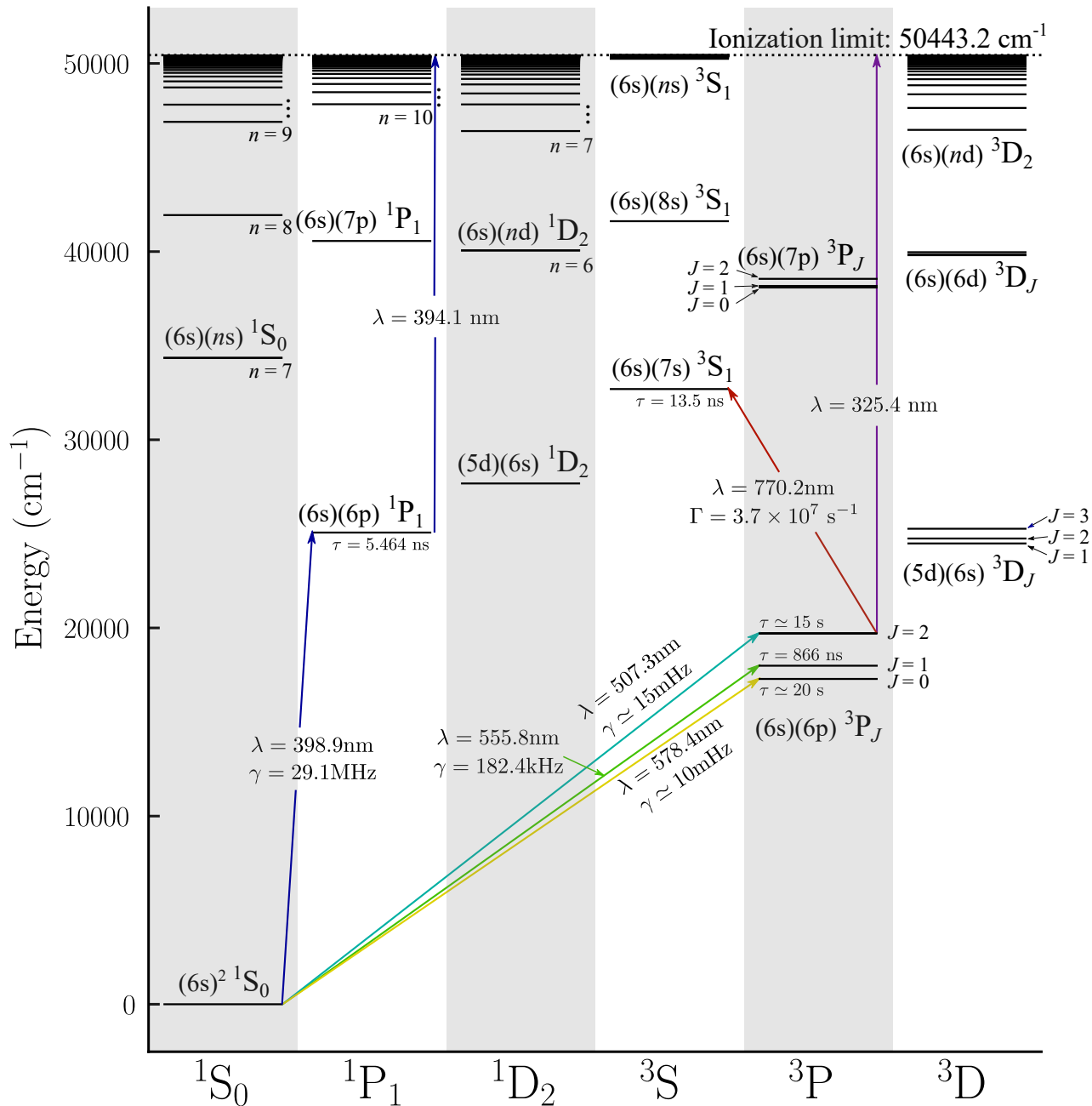
Figure 3.2: Energy levels of the Ytterbium atom is shown. The natural linewidth of the transition γ is given for a well closed transitions. For those transitions which have multiple states to decay, the inverse of the lifetime Γ is written. The energy of each levels is cited from [93], except $(6s)(ns)\ ^1S_0$, $(6s)(nd)\ ^1D_2$, $(6s)(nd)\ ^3D_2$ (n = 7-80) [94], and $(6s)(ns)\ ^3S_1$ (n = 28-97) [64].

thus enabling the coupling of the $^3P_1$ and $^1S_0$. The value of α and β can be obtained from the lifetime of each state by the following equation, considering that the $|^3P_1^0\rangle$ doesn't couple with the ground state,

$$\frac{|\alpha|^2}{|\beta|^2} = \frac{\tau(^3P_1)E(^3P_1)^3}{\tau(^1P_1)E(^1P_1)^3}, \tag{3.3}$$

where $\tau(\cdot)$ and $E(\cdot)$ represents the lifetime and the energy of a state, respectively. From this we can derive $|\alpha|^2 = 0.9834$ and $|\beta|^2 = 0.0166$.

Compared with $^1S_0$–$^1P_1$ transition, the MOT with this intercombination line is desirable because it is free from the loss of atoms by the branching. In addition to it, the narrow linewidth realizes much lower Doppler-limited temperature $T_D = h\Gamma/2k_B = 4.4\,\mu$K compared with alkali-atoms. Meanwhile this linewidth creates enough radiation pressure to perform the Magneto-Optical Trap (MOT) without other transitions, which is why we adopt the transition for the MOT. Except MOT, the transition is used for light-assisted collisions and fluorescence imaging, mainly because of compatibility with the high-NA imaging system as described in section 5.1.

Table 3.1: Frequently used parameters for $^1S_0\leftrightarrow^1P_1$, $^1S_0\leftrightarrow^3P_1$, and $^3P_2\leftrightarrow^3S_1$ transitions are summarized.

Parameter		$^1S_0\leftrightarrow^1P_1$	$^1S_0\leftrightarrow^3P_1$	$^3P_2\leftrightarrow^3S_1$	Unit
Wavelength	λ	398.9	555.8	770.2	nm
Lifetime	τ	5.5	873	13	ns
Natural linewidth	$\Gamma/2\pi = 1/2\pi\tau$	29	182		MHz
Saturation intensity	I_{sat}	59	0.139	1.7	mW/cm^2
Recoil energy	E_R/k_B	344	178	93	nK

3.1.2.3 $(6s)^2\,^1S_0 \leftrightarrow (6s)(6p)\,^3P_2$

Doubly forbidden as E1 transition ($\Delta S \neq 0$, $\Delta J \neq \pm1$). This transition is allowed as magnetic quadrupole (M2) transition or, in the case of fermionic isotopes, as a hyperfine mixing induced E1 (HFM-E1) transition.

- Bosonic isotopes — M2 transition

  As derived in Eq. (2.34), the selection rule of the magnetic sublevels of the M2 transition is given by

  $$\langle f|\,\mathcal{H}_{L=2}^{(M)}\,|i\rangle \propto \hat{e}_\lambda \cdot Y_2^{(M)}(\hat{k}), \tag{3.4}$$

where the explicit form of the spherical harmonic vector is expressed as

$$Y_{\pm 2}^{(M)}(\hat{k}) = \sqrt{\frac{5}{16\pi}}e^{\pm i\phi_k}\sin\theta_k\left(\sqrt{2}\cos\theta_k\hat{e}_{\pm 1} \pm \sin\theta_k e^{\pm i\phi_k}\hat{e}_0\right) \tag{3.5}$$

$$Y_{\pm 1}^{(M)}(\hat{k}) = \mp\frac{1}{4}\sqrt{\frac{5}{6\pi}}\left((3\cos^2\theta_k - 1)\hat{e}_{\pm} \pm \sqrt{6}\cos\theta_k\sin\theta_k e^{\pm i\phi_k}\hat{e}_0 - \sqrt{3}\sin^2\theta_k e^{\pm 2i\phi_k}\hat{e}_{\mp}\right) \tag{3.6}$$

$$Y_0^{(M)}(\hat{k}) = -\frac{1}{4}\sqrt{\frac{15}{\pi}}\cos\theta_k\sin\theta_k(e^{-i\phi_k}\hat{e}_+ + e^{i\phi_k}\hat{e}_-) \tag{3.7}$$

We show examples of selection rules in several situations in Fig. 3.3. Here z axis corresponds to the quantization axis.

(i)
$\theta_k = 0$
$\hat{e}_\lambda = \hat{x}$
$z \parallel B$
$\Delta m = \pm 1$

(ii)
$\theta_k = 45°$
$\hat{e}_\lambda = (\hat{x} + \hat{z})/\sqrt{2}$
$z \parallel B$
$\Delta m = 0, \pm 1, \pm 2$

(iii)
$\theta_k = 45°$
$\hat{e}_\lambda = \hat{y}$
$z \parallel B$
$\Delta m = 0, \pm 1, \pm 2$

(iv)
$\theta_k = 90°$
$\hat{e}_\lambda = \hat{z}$
$z \parallel B$
$\Delta m = \pm 2$

(v)
$\theta_k = 90°$
$\hat{e}_\lambda = \hat{y}$
$z \parallel B$
$\Delta m = \pm 1$
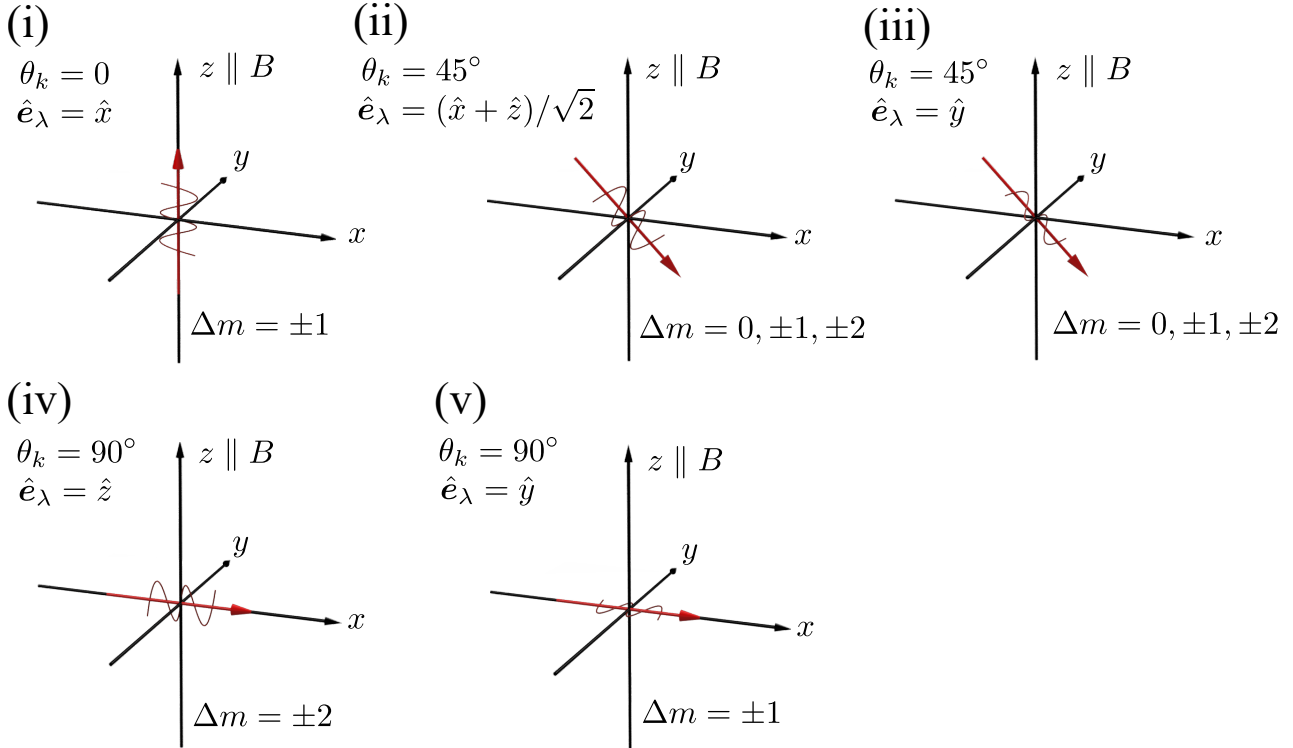
Figure 3.3: Five configurations of the laser direction $\hat{k}$ and the polarization $\hat{e}_\lambda$ (i)$\theta_k = 0, \hat{e}_\lambda = \hat{x}$, (ii)$\theta_k = 45°, \hat{e}_\lambda = (\hat{x} + \hat{z})/\sqrt{2}$, (iii)$\theta_k = 45°, \hat{e}_\lambda = \hat{y}$, (iv)$\theta_k = 90°, \hat{e}_\lambda = \hat{z}$, (v)$\theta_k = 90°, \hat{e}_\lambda = \hat{y}$ and the allowed change of the magnetic sublevels Δm in each cases is shown. z axis is set to be the quantization axis.

- Fermionic isotopes — Hyperfine mixing induced E1 transition

  In the case of fermionic isotopes, hyperfine interaction — the interaction between electron's angular momentum and the nuclear spin — mixes the pure LS-coupling eigenstates. Perturbed state up to the first order is

$$|^3P_2; F, m_F\rangle = \sum_\alpha \frac{\langle ^3P_2^0; F, m_F|\mathcal{H}_{\mathrm{HF}}|\alpha\rangle}{E(\alpha) - E(^3P_2^0)}|\alpha\rangle, \tag{3.8}$$

where $\mathcal{H}_{\mathrm{HF}}$ denotes the hyperfine interaction. The dipole coupling between the $^3P_2$ and the $^1S_0$ thus become

$$\sum_\alpha \frac{\langle ^3P_2^0; F, m_F | \mathcal{H}_{\mathrm{HF}} | \alpha \rangle}{E(\alpha) - E(^3P_2^0)} \langle \alpha | d | ^1S_0; F', m_{F'} \rangle. \tag{3.9}$$

This takes a non-zero value via an intermediate state $|\alpha\rangle$ E1-coupled with the ground state, such as (6s)(6p) $^3P_1$.

Table 3.2: Frequently used parameters of $^1S_0 \leftrightarrow ^3P_2$ transition. Because hyperfine structure changes the strength of the transition, each parameters for bosonic isotopes, ^{171}Yb, and ^{173}Yb are listed.

Parameter		Boson	^{173}Yb	^{171}Yb	Unit
Wavelength	λ		507.35		nm
Lifetime	τ	15	6.3	7.2	s
Natural linewidth	$\Gamma/2\pi = 1/2\pi\tau$	10.6	25	22	mHz
Saturation intensity	I_{sat}	1.1×10^{-8}	2.5×10^{-8}	2.2×10^{-8}	mW/cm^2
Recoil energy	E_R/k_B		214		nK

3.1.2.4   (6s)(6p) $^3P_2 \leftrightarrow$ (6s)(7s) $^3S_1$

$^3P_2$ state has long lifetime and therefore it requires repumping light to back to the ground state. We use $^3P_2 \leftrightarrow ^3S_1$ for this purpose. This is E1-allowed transition with a wavelength of 770 nm. The $^3S_1$ state atom decays to not only $^3P_2$ but also $^3P_0$ and $^3P_1$ which means this is not closed transition. The branching ratio to $^3P_0$, $^3P_1$, and $^3P_2$ state is 13%, 37%, and 50%, respectively [98].

3.2   Rydberg states

3.2.1   General properties of Rydberg atoms

The outermost electron of a Rydberg atom is in the large and weakly bound orbit with the principal quantum number n typically larger than several tens, which makes properties of Rydberg atoms exaggerated compared to those of lower energy states in which the outermost electron resides the orbit with the comparable n with the ground state [99]. In general, despite the complexity of electron's wavefunctions of non-hydrogenic atoms, the properties of a Rydberg atom obey simple scaling laws of n, or more precisely effective principal quantum number n^*, as well as a hydrogen atom, which can be understood as a consequence of the small overlap between the wavefunctions of core and outermost electrons for large n. The Schrödinger equation of a hydrogen atom — the simplest and the only analytically solvable atom — for the radial part of wavefunction rescaled by r is given by

$$\left(-\frac{\mathrm{d}^2}{\mathrm{d}^2 r} + \frac{l(l+1)}{r^2} - \frac{2}{r} \right) u_{nl}(r) = 2E_n u_l(r), \tag{3.10}$$

in (Hartree) atomic unit. Note we use the atomic unit throughout this chapter. l is the orbital angular momentum of the electron. This is equivalent to the one-dimensional Schrödinger equation in an effective potential

$$V_{\text{eff}}(r) = \frac{l(l+1)}{r^2} - \frac{2}{r}.$$

$$(3.11)$$

The eigenenergy and the eigenfunction of Eq. (3.10) is

$$E_n = -\frac{1}{2n^2},$$

$$(3.12)$$

$$u_{nl}(r) = C_{nl}(2r/n)^{l-1}L_{n+l}^{2L+1}(2r/n)e^{-r/n},$$

$$(3.13)$$

of which derivation can be seen in plenty of textbooks (See [100], for example). Here $L_n^m(x)$ and C_{nl} denotes associated Laguerre polynomial and a normalizing constant, respectively. Explicit form of the normalizing coefficient is

$$C_{nl} = \sqrt{\left(\frac{2}{n}\right)^3 \frac{(n-l-1)!}{2n(n+l)!}}.$$

$$(3.14)$$

Exaggerated properties of Rydberg atoms mainly originate from their huge orbit. In the semi-classical approach, the classically allowed region (i.e., $\{\, r \mid V_{\text{eff}}(r) < -1/(2n^2) \,\}$), where dominate the wavefunction, spans from $r_{\text{in}} \propto l(l+1)$ to $r_{\text{out}} \propto n^2$. Because the expectation value of r primarily depends on large-r part of the wavefunction, we can infer the scaling law of r as $\langle r \rangle \sim r_{\text{out}} \sim n^2$. One can confirm this is true by applying the exact solution Eq. (3.13) to $\langle r \rangle_{nl} = \int_0^\infty dr u_{nl}^*(r) r u_{nl}(r)$ [2]. From this we immediately obtain the scaling law of the dipole moment of Rydberg atoms:

$$\langle d \rangle_{nl} = \langle nl | (er) | nl \rangle \propto n^2$$

$$(3.16)$$

Another important feature of the Rydberg atoms is its long radiative lifetime which scales as n^3. The lifetime of the state is given as the inverse of the summation of the Einstein A coefficient for all possible spontaneous emission channels. The lifetime of a Rydberg state with a principal quantum number n and angular momentum l: τ_{nl} is given by

$$1/\tau_{nl} = \sum_{n'l'} A_{nl,n'l'}$$

$$(3.17)$$

$$\propto \sum_{n',l'} |E_{nl} - E_{n'l'}|^3 |\langle nl | (er) | n'l' \rangle|^2$$

$$(3.18)$$

The scaling of transition dipole matrix element changes depending on whether the transition is between Rydberg states ($n' \simeq n$, Microwave transitions) or with low-lying energy states ($n' \ll n$,

---

[2]The exact expectation value of the radius is given by

$$\langle r \rangle_{nl} = n^2 \left(1 + \frac{1}{2}\left(1 - \frac{l(l+1)}{n^2}\right)\right).$$

$$(3.15)$$

Optical transitions):

$$\langle nl|\,(er)\,|n'l'\rangle \sim \begin{cases} n^{-3/2} & (n' \ll n) \\ n^2 & (n' \simeq n). \end{cases}$$
(3.19)

The term of energy difference in Eq. (3.18) scales as n^{-3} for microwave transitions and n^{-2} for optical transitions. Therefore we find the dominant channel to determine the lifetime comes from optical transitions and result in the scaling as $\tau_{nl} \sim n^3$.

Scaling laws of several physical quantities and its typical values of Rb atom for $n = 50$ and $l = \mathrm{p}$ as an example is summarized in Table 3.3.

Table 3.3: Scaling laws of physical characters and actual values of Rubidium Rydberg atoms in the case of $n = 50$ and $l = \mathrm{p}$ is summarized.

Property	n scaling	Rb (50p)
Binding energy	n^{-2}	$6.2\,\mathrm{meV} = h \times 1.5\,\mathrm{THz}$
Energy between adjacent states	n^{-3}	$0.22\,\mathrm{meV} = h \times 53\,\mathrm{GHz}$
Radiative lifetime	n^3	$106\,\mu\mathrm{s}$
Orbital radius	n^2	$3200\,a_0 = 170\,\mathrm{nm}$
Scalar polarizability	n^7	$\sim\mathrm{GHz} \cdot \mathrm{cm}^2/\mathrm{V}^2$
van der Waals interaction C_6	n^{11}	$\sim 10\,\mathrm{GHz} \cdot \mu\mathrm{m}^6$

3.2.2   Response to static electric fields

Despite the discussion in the previous section assuming the similarity between Rydberg states of non-hydrogenic atoms and hydrogen atom, we should remark this is not always true. DC Stark shift — the shift of energy by an applied static electric field — is a good example. The stark shift comes from the interaction between the dipole d of the atom and an electric field E:

$$\mathcal{H}_{\mathrm{Stark}} = -d \cdot E.$$
(3.20)

Since the parity of $\mathcal{H}_{\mathrm{Stark}}$ is odd and energy levels of a hydrogen atom is degenerate with respect to l, the first order of perturbation doesn't vanish, resulting in linear response to electric fields. In cases of non-degenerate atoms, however, the first order perturbation vanishes due to the parity difference and the second order perturbation becomes the dominant term. We can thus derive the Stark shift as

$$\Delta E_{\mathrm{Stark}} = -\alpha_{nj}\frac{E^2}{2},$$
(3.21)

where α is the scalar static polarizability and j denotes all quantum numbers other than n. α_{nj} scales as

$$\alpha_{nj} = -2 \sum_{n'j' \neq nj} \frac{|\langle n'j'|\,d\,|nj\rangle|^2}{|E_{n',j'} - E_{nj}|^2} \sim \frac{n^4}{n^{-3}} \sim n^7.$$
(3.22)

We note the dominant contribution comes from dipole transition matrix elements between neighboring Rydberg states, different from the radiative lifetime. The dependency of the polarizability on total angular momentum J and magnetic sublevel M can be derived by separating $\mathcal{H}_{\text{Stark}}$ into scalar and tensor part [101] (we don't describe the derivation here):

$$\Delta E_{\text{Stark}} = -\frac{1}{2}\alpha_0(J)E^2 - \frac{1}{4}\alpha_2(J)\frac{3M^2 - J(J+1)}{2(2J-1)}(3E_z^2 - E^2), \tag{3.23}$$

where E_z is the component of the electric field along the quantization axis.

3.2.3 Interactions between Rydberg atoms

Interactions between Rydberg atoms are the most important feature for applications to quantum information processings. The interaction originates from dipole–dipole interaction given by

$$V_{\text{dd}} = \frac{\boldsymbol{d}_1 \cdot \boldsymbol{d}_2 - 3(\boldsymbol{d}_1 \cdot \boldsymbol{R}/R)(\boldsymbol{d}_2 \cdot \boldsymbol{R}/R)}{R^3}, \tag{3.24}$$

where $\boldsymbol{d}_1, \boldsymbol{d}_2$, and $\boldsymbol{R}$ denotes the dipole moment of atom 1, 2 and the interatomic distance, respectively. Let us consider the interaction between a pair of atoms both in $|nj\rangle$ state. j denotes all
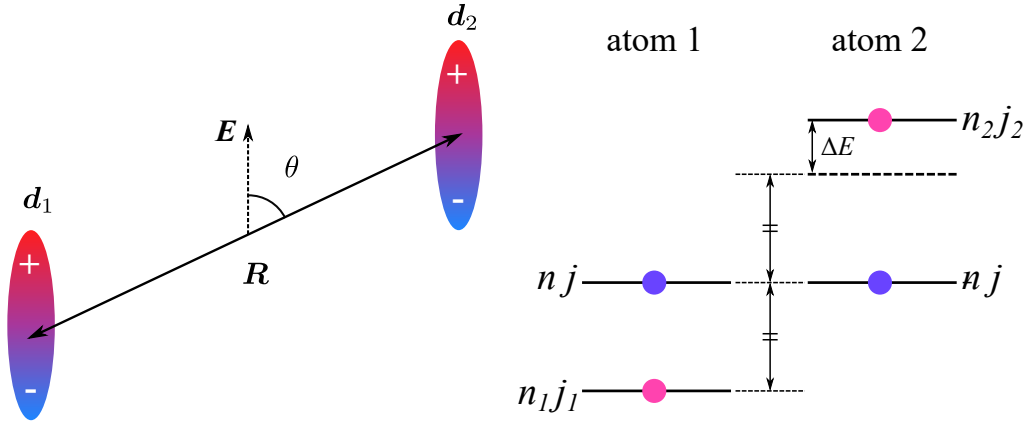
Figure 3.4: (Left) The geometry of two atoms with dipole moments $\boldsymbol{d}_1$ and $\boldsymbol{d}_2$ aligned along the electric field $\boldsymbol{E}$, and relative position vector $\boldsymbol{R}$. θ is an angle between $\boldsymbol{R}$ and $\boldsymbol{d}_1, \boldsymbol{d}_2$. (Right) Relevant energy levels of unperturbed states appears in the second order perturbation.

quantum numbers except n as well as in the previous section. When there are no degeneracies, that is to say, when unperturbed energy of all pairs of atom's states is not equal to that of $|nj; nj\rangle$ state, the perturbed energy up to the second order is

$$E_{\text{dd}}^{(2)} = \underbrace{\langle nj; nj| V_{\text{dd}} |nj; nj\rangle}_{\to 0} + \sum_{n_1 j_1; n_2, j_2} \frac{|\langle nj; nj| V_{\text{dd}} |n_1 j_1; n_2 j_2\rangle|^2}{\Delta E}, \tag{3.25}$$

$$\Delta E \equiv 2E_{nj} - (E_{n_1 j_1} + E_{n_2 j_2}), \tag{3.26}$$

where all braket vectors and E_{nl} denote unperturbed states and energy, respectively. The first order perturbation vanishes because the parity of V_{dd} is odd likewise in the previous section. One can

find the scaling law of this interaction as

$$E_{\mathrm{dd}}^{(2)} = \frac{C_6}{R^6} \sim \frac{1}{R^6} \frac{(n^2 \cdot n^2)^2}{n^{-3}} = \frac{n^{11}}{R^6} \equiv E_{\mathrm{vdW}}, \tag{3.27}$$

which is referred as **van der Waals interactions**.

The assumption of non-degeneracy, however, sometimes breaks. In other words, there may exist a pair of states satisfies resonant condition $\Delta E = 0$, or more precisely, $\Delta E \ll |\langle nj; nj| V_{\mathrm{dd}} |n_1 j_1; n_2 j_2\rangle|$. In this case the first order perturbation does not vanish and it becomes

$$E_{\mathrm{dd}}^{(1)} = \frac{C_3}{R^3} \sim \frac{n^4}{R^3}, \tag{3.28}$$

and this is called the **resonant dipole–dipole interaction** or **Förster resonance**. While this condition is rarely satisfied for bare atoms, DC-stark shifts can tune pair states into degeneracy. We call such technique **Stark-tuned Förster resonance**.

Lastly we discuss the angular dependency of the interaction strength. V_{dd} is decomposed by spherical basis as following [102]:

$$V_{\mathrm{dd}} = \frac{1}{R^3} \Big(A_0(\theta) \left(d_{1(1)} d_{2(-1)} + d_{1(-1)} d_{2(1)} + 2 d_{1(0)} d_{2(0)} \right) \tag{3.29}$$

$$+ A_1(\theta) \left(d_{1(1)} d_{2(0)} - d_{1(-1)} d_{2(0)} + d_{1(0)} d_{2(1)} - d_{1(0)} d_{2(-1)} \right) \tag{3.30}$$

$$- A_2(\theta) \left(d_{1(1)} d_{2(1)} + d_{1(-1)} d_{2(-1)} \right) \Big). \tag{3.31}$$

Here $d_{i(q)} \equiv d_i Y_1^q(\theta, \phi)$ and

$$A_0(\theta) = \frac{1 - 3\cos^2\theta}{2}, \ A_1(\theta) = \frac{3\sin\theta\cos\theta}{\sqrt{2}}, \ A_2(\theta) = \frac{3\sin^2\theta}{2}. \tag{3.32}$$

The term containing A_0, A_1, A_2 (Eq. (3.29), Eq. (3.30), Eq. (3.31)) correspond to the coupling of pair states of which difference of the total magnetic quantum number ΔM is $0, \pm 1, \pm 2$, respectively. When $\Delta M = 0$, the angular dependence of the interaction become equivalent to that between the permanent dipole moment : $\propto (1 - 3\cos^2\theta)/2$. This is actually demonstrated and exploited using a Förster resonance

$$|59\mathrm{D}_{3/2}, m = 3/2\rangle \otimes |59\mathrm{D}_{3/2}, m = 3/2\rangle \leftrightarrow |61\mathrm{P}_{1/2}, m = 1/2\rangle \otimes |57\mathrm{F}_{5/2}, m = 5/2\rangle \tag{3.33}$$

of Rb atoms by Institut d' Optique [103]. As just described, the calculation of angular dependence of the resonant dipole–dipole interaction is straightforward and simple. On the other hand, for van der Waals interaction, we need to sum up all the possible channels and it makes the calculation difficult. In general, however, the interaction become nearly isotropic by averaging each channel's angular dependencies unless close to Förster resonance which only one channel dominate the interaction.

3.2.4   Entanglement between Rydberg atoms

The strength of interactions between Rydberg atoms few μm apart are typically in the order of $h \times 100\,\mathrm{MHz}$. This enables generation of entanglement of atoms. The simplest example is a CNOT

gate operation on qubits defined by the Rydberg state $|0\rangle \equiv |r\rangle$ and the ground state $|1\rangle \equiv |g\rangle$. Here we assume that we can excite an atom to a Rydberg state individually (though this is challenging, actually). X gate on a single qubit corresponds to applying a π-pulse: $|0\rangle \rightarrow |1\rangle$, $|1\rangle \rightarrow |0\rangle$. When the control qubit is in the ground state, the situation is the same as that of non-interacting system. When the control atom is in the Rydberg state, however, this π-pulse does not change the qubit state anymore, due to the resonance shift by the strong interaction (Fig. 3.5). This is exactly the CNOT gate
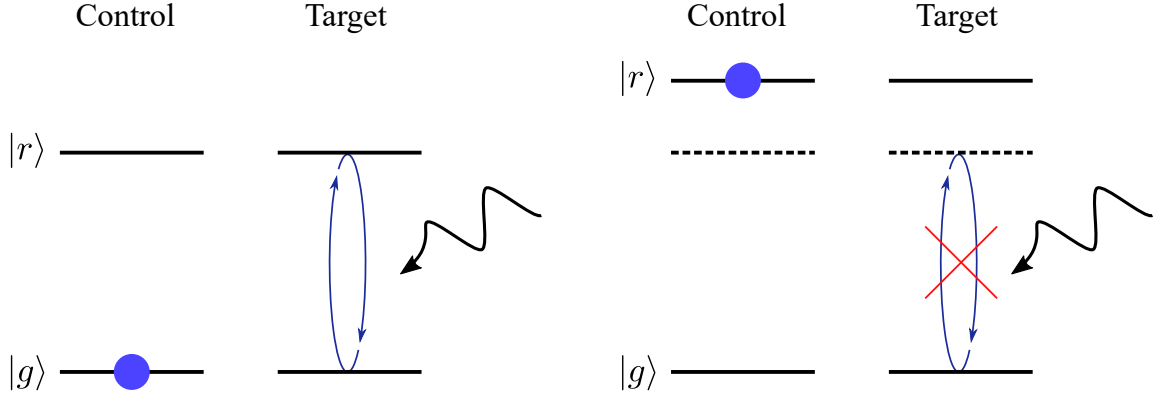

Figure 3.5: Illustration of a scheme to implement CNOT gate using interactions between Rydberg state. The strong interaction shifts the energy of Rydberg states and suppress π-pulse between $|g\rangle$ and $|r\rangle$.

operation. The suppression of simultaneous excitation by the strong interaction described above is called **Rydberg blockade**, the core phenomenon for applications of Rydberg states to quantum computation and quantum simulation.

Let us discuss this blockade effect more quantitatively. The hamiltonian of two atoms under exposure to a laser resonant to the bare $|g\rangle \leftrightarrow |r\rangle$ transition (Left side of Fig. 3.6) is

$$\mathcal{H} = \frac{\Omega}{2} \left(|r\rangle \langle g| \otimes \mathbf{1} + \mathbf{1} \otimes |r\rangle \langle g| + \text{h.c.} \right) + V |rr\rangle \langle rr| \tag{3.34}$$

$$= \frac{\sqrt{2}\Omega}{2} \left(\frac{|gr\rangle + |rg\rangle}{\sqrt{2}} \langle gg| + |rr\rangle \frac{\langle gr| + \langle rg|}{\sqrt{2}} + \text{h.c.} \right) + V |rr\rangle \langle rr|, \tag{3.35}$$

where V is the interaction between Rydberg states. One finds this is equivalent with ladder three-level system consists of $|gg\rangle$, $|rr\rangle$, and $|\psi\rangle \equiv (|gr\rangle + |rg\rangle)/\sqrt{2}$, where the rabi frequency for both transitions is $\sqrt{2}\Omega$ and the detuning is zero for the lower transition and V for the upper transition (Right side of Fig. 3.6). Note this equivalence holds only when the laser detuning is zero. Remember that the modulation depth of the two-level system with the rabi frequency Ω and the detuning Δ is given by $1/(1 + \Delta^2/\Omega^2)$, $V \gtrsim \Omega$ should be a criteria whether the blockade occur. From Eq. (3.27), we obtain a boundary distance for the blockade effect to occur:

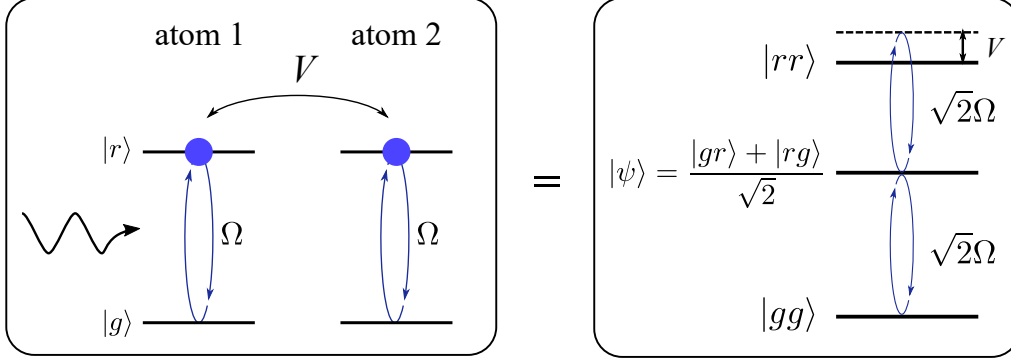$$R_b = \left(\frac{C_6}{\hbar \Omega} \right)^{1/6}, \tag{3.36}$$

Figure 3.6:   The system of two atoms and laser resonant to bare Rydberg transition is equivalent to three-level system composed of $|gg\rangle$, $|rr\rangle$, and $|\psi\rangle$. The rabi frequency of both transitions is enhanced to $\sqrt{2}\Omega$ and the detuning of upper transition corresponds to interaction V.

which is called **blockade radius**. This discussion can also be extended to interacting N-atom system. Let the interaction between i-th atom and j-th atom be V_{ij}. The hamiltonian is described as

$$\mathcal{H} = \frac{\Omega}{2} \sum_{i=1}^{N} \left(\mathbf{1}_1 \otimes \cdots \otimes (\sigma_i + \sigma_i^\dagger) \otimes \cdots \otimes \mathbf{1}_N \right) + \sum_{\forall|\phi\rangle} \sum_{i\neq j} V_{ij} \langle\phi| \sigma_i^\dagger \sigma_i \sigma_j^\dagger \sigma_j |\phi\rangle |\phi\rangle \langle\phi| \tag{3.37}$$

$$= \sqrt{N}\frac{\Omega}{2} \left(|\psi_N\rangle \langle G| + |G\rangle \langle\psi_N| \right) \tag{3.38}$$

$$+ \frac{1}{2} \sum_{\substack{\forall i, \forall|\phi\rangle \\ |\phi\rangle, \sigma_i|\phi\rangle \neq |G\rangle}} \left(\Omega \left(\sigma_i |\phi\rangle \langle\phi| + \text{h.c.} \right) + \sum_j V_{ij} \langle\phi| \sigma_i^\dagger \sigma_i \sigma_j^\dagger \sigma_j |\phi\rangle \sigma_i |\phi\rangle \langle\phi| \sigma_i^\dagger \right), \tag{3.39}$$

where we have defined

$$|\psi_N\rangle \equiv \frac{1}{\sqrt{N}} \sum_{i=1}^{N} |g_1 \cdots r_i \cdots g_N\rangle, \tag{3.40}$$

$$|G\rangle \equiv |g_1 g_2 \cdots g_n\rangle, \tag{3.41}$$

$$\sigma_i \equiv |g_i\rangle \langle r_i|. \tag{3.42}$$

The first and the second term of Eq. (3.39) corresponds to the resonant rabi oscillation between $|G\rangle$ and $|\psi_N\rangle$, and the summation of detuned rabi oscillations between $|\phi\rangle$ and $\sigma_i |\phi\rangle$ by $\Delta = \sum_j V_{ij} \langle\phi| \sigma_i^\dagger \sigma_i \sigma_j^\dagger \sigma_j |\phi\rangle$, respectively. The second term is suppressed by strong interactions V_{ij} and only the first term appears. The rabi frequency of the first term is enhanced to $\sqrt{N}\Omega$ by entanglement and this is (sometimes) called the **blockade-enhanced rabi frequency**.

3.2.5 Two-electron Rydberg atoms

Two-electron Rydberg atoms have desirable properties for quantum computing and quantum simulation arising from the inner velance electron, as we note in section 1.2. In this section, we give short introductions to two of them: Auto-ionization (AI) and optical dipole trap of Rydberg states, taking Yb atom as an example.
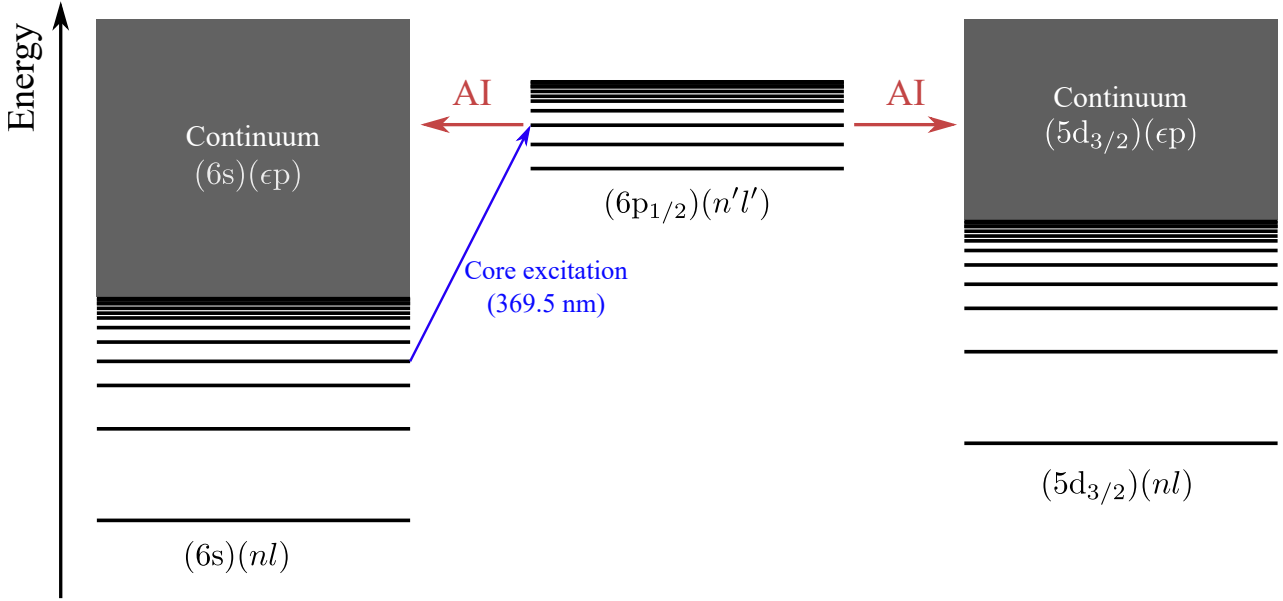
3.2.5.1 Auto-ionization

Figure 3.7: Core excitation of a (6s)(nl) Rydberg state to a doubly excited state ($6p_{1/2}$)(nl) results in decays into continua (6s)(ϵp) and ($5d_{3/2}$)(ϵp).

Singly excited Rydberg states (6s)(nl) of Yb atoms have an transition to a doubly excited Rydberg ($6p_{1/2}$)($n'l'$) state likewise the (6s)$\leftrightarrow$(6p) transition of Yb$^+$ ions. This doubly excited state evolves into a continuum state $|\epsilon\rangle$ (Fig. 3.7) in the time-dependent picture with a rate

$$\Gamma_{\mathrm{AI}} = \sum_{\epsilon} |\langle\epsilon| V_{\mathrm{ee}} |(6p_{1/2})(n'l')\rangle|^2 \tag{3.43}$$

from the Fermi's golden rule. V_{ee} is the interaction hamiltonian between the Rydberg and the inner electron. The summation is taken over all continuum states coupled with ($6p_{1/2}$)($n'l'$): (6s)(ϵp) and ($5d_{3/2}$)(ϵp). Though this doubly excited state seems to be a bound state, because the total energy exceeds the binding energy (first ionization limit), the spectrum of photon absorption of this transition is continuous but "lumpy" with several peaks corresponding to the eigenenergies for the (6p) channel potential (Feshbach resonances) [61, 104]. This auto-ionization process has been used for high-fidelity detection of Rydberg states of Sr atoms [38]. The core excitation transition of Yb atoms has been used to induce energy shifts to Rydberg state [62, 63].

3.2.5.2 Optical trapping of Rydberg state

A energy of a free electron in the presence of an oscillating electromagnetic field with ω and the amplitude E shifts by $E^2/(4\omega^2)$ (in atomic units), which is always positive and called **ponderomotive shift**. The light shift of alkali Rydberg states, therefore, is repulsive and it cannot be trapped directly.

For the case of AE(L)As, however, the contribution from the ionic core transition can make the dipole force attractive. Because the typical radius of the Rydberg electron is comparable with the op-

tical wavelengths, we should take into account the spatial distribution of the electron's wavefunction $\psi_{nl}(r)$ and the laser intensity $I(r)$ for sub-micron optical traps. The resulting potential at position R is given by

$$V(R) = -\frac{\alpha_{\text{ion}}}{4}I(R) + \frac{1}{\omega^2}\int |\psi_{nl}|^2(r)I(r + R)\mathrm{d}r^3, \tag{3.44}$$

where I_0 and α_{ion} is the laser intensity at the atomic core and the ionic polarizability, respectively.

3.2.6   Quantum Defect Theory

The basic idea of quantum defect theory is to characterize the wavefunction of non-hydrogenic atoms by how "defective" it is from hydrogen atom to simplify the problem. The difference between a hydrogen atom and a non-hydrogenic atom is interactions (V_{ee}) between the outermost electron and core electrons. As is experimentally observed by pulse laser spectroscopy [105], this interaction arises when the outermost electron get closer to the atomic core. When the outermost electron is far enough from the core, it is justified to treat the electron similarly as the hydrogen atom. Let this boundary distance be r_0. The space can be divided into two regions (i) $r \leq r_0$: interacting region and (ii) $r > r_0$: hydrogenic region. The quantum defect theory does NOT try to calculate the wavefunction in interacting region. It extracts parameters from boundary conditions at $r = r_0$ and $r \to 0$ which simplifies the experimentally obtained data or *ab initio* calculations. For the detailed discussion, see [104, 106, 107].

3.2.6.1   One electron atoms — Single channel

Alkali atoms has only a single internal state (single channel) of core electrons. We just consider boundary conditions at $r = r_0$ and $r \to \infty$ of that channel.

In the hydrogenic part, the wavefunction of the outermost electron ($u_{E,l}(r)$) is given as a linear combination of two independent solutions of Eq. (3.10). It is convenient to choose regular and irregular coulomb wavefunctions f and g which behaves as

$$f_{E,l}(r) \to \begin{cases} r^{l+1} & (r \to 0), \\ \sqrt{n^*/\pi}\left(\sin\beta D^{-1}r^{-n^*}e^{r/n^*} - \cos\beta Dr^{n^*}e^{-r/n^*}\right) & (r \to \infty), \end{cases} \tag{3.45}$$

$$g_{E,l}(r) \to \begin{cases} r^{-l} & (r \to 0), \\ -\sqrt{n^*/\pi}\left(\cos\beta D^{-1}r^{-n^*}e^{r/n^*} + \sin\beta Dr^{n^*}e^{-r/n^*}\right) & (r \to \infty), \end{cases} \tag{3.46}$$

where we have defined $\beta = \pi(n^* - l)$. The energy E and the effective principal quantum number n^* are related as $E = -1/2n^{*2}$. D is a constant dependent on E and l. We impose two boundary conditions to the wavefunction $u_{E,l}(r)$:

$$\begin{cases} \dfrac{W(f, u_{E,l})}{W(g, u_{E,l})} = \tan\pi\delta_l & (r = r_0) \\ u_{E,l}(r) \to 0 & (r \to \infty). \end{cases} \tag{3.47}$$

Here W denotes the Wronskian

$$W(y_1, y_2) \equiv \begin{vmatrix} y_1 & y_2 \\ y_1' & y_2' \end{vmatrix}. \tag{3.48}$$

The second boundary condition comes from the physical requirement to be bound state ($E < 0$). The first requirement, which seems arbitrary at first glance, is just a expression that the wavefunction $u_{E,l}(r)$ is given as

$$u_{E,l}(r) \propto \cos \pi \delta_l f_{E,l}(r) + \sin \pi \delta_l g_{E,l}(r) \quad (r > r_0). \tag{3.49}$$

Note that the ratio of Wronskians Eq. (3.47) is a constant value for $r > r_0$. Eq. (3.49) means that the radial phase is shifted from the hydrongen's wavefunction. By substituting Eq. (3.49), we obtain

$$\sin(\beta + \pi \delta_l) = 0 \tag{3.50}$$

$$\Leftrightarrow n^* + \delta_l = n \quad (n = 0, 1, 2, \ldots) \tag{3.51}$$

The n-th eigenenergy is

$$E_n = -\frac{1}{2n^{*2}} = -\frac{1}{2(n - \delta_l)^2}. \tag{3.52}$$

n^* and δ_l is called **effective principal quantum number** and **quantum defect**, respectively. Because the change of eigenenergy $E_{n+1} - E_n \sim 0.01$ eV is quite small compared with electron's kinetic energy ~ 10 eV, the radial phase shift is almost independent on E and n. We therefore obtain a single parameter to characterize the spectrum of Rydberg series.

3.2.6.2 Two electron atoms — Multi channel

In the case of two electron atoms, we need to consider multiple channels as the effective potential of Rydberg electrons depends on the internal state of ionic core. For each channel the similar discussions as in alkali atoms can be applied. We consider only hydrogenic region of Rydberg electron. The wavefunction of the atom $|\psi\rangle$ is given as a summation of all channel wavefunctions

$$|\psi_\alpha\rangle = \sum_i |\Phi_i\rangle |u_{i\alpha}\rangle. \tag{3.53}$$

The subscript α distinguishes linearly independent degenerate eigenstates in energy. i denotes the channel. $|\Phi_i\rangle$ is the wavefunction "orthogonal" to the radial coordinate of Rydberg electron, namely eigenstates of the inner electron hamiltonian and angular momentum operator of Rydberg electron. $u_{i\alpha}$ is a radial wavefunction rescaled by r. Wavefunction $u_{i\alpha}$ is a summation of regular and irregular coulomb wavefunction

$$u_{i\alpha}(r) = f_{E_i,l_i} I_{i\alpha} - g_{E_i,l_i} J_{i\alpha}, \tag{3.54}$$

where E_i is a asymptotic kinetic energy of Rydberg electron in the i-th channel: $E_i = E - I_i$, where I_i is the ionization limit for i-th channel. We define K matrix as

$$K = IJ^{-1}, \tag{3.55}$$

which can be diagonalized by an unitary matrix U

$$K = U\text{diag}(\tan \pi\delta_1, \tan \pi\delta_2, \ldots)U^\dagger. \tag{3.56}$$

This can be regarded as a boundary condition at r_0, counterpart of Eq. (3.47). μ_α indicates phase shift of the i-th channel. From the boundary condition at $r \to 0$, we obtain

$$|K + \text{diag}(\tan \pi n_1^*, \tan \pi n_2^*, \ldots)| = 0, \tag{3.57}$$

where principal quantum number for i-th channel n_i^* is defined similarly as in Eq. (3.52):

$$E_i = -\frac{1}{2n_i^{*2}} \iff E = I_i - \frac{1}{2n_i^{*2}} \tag{3.58}$$

The aim of MQDT model is to solve K matrix which satisfies Eq. (3.57) and Eq. (3.58) simultaneously, and agrees additional information obtained by *ab initio* calculations or experimental data.

Apparatuses and techniques of the experiments

4.1 Experimental Apparatuses

4.1.1 Vacuum chamber

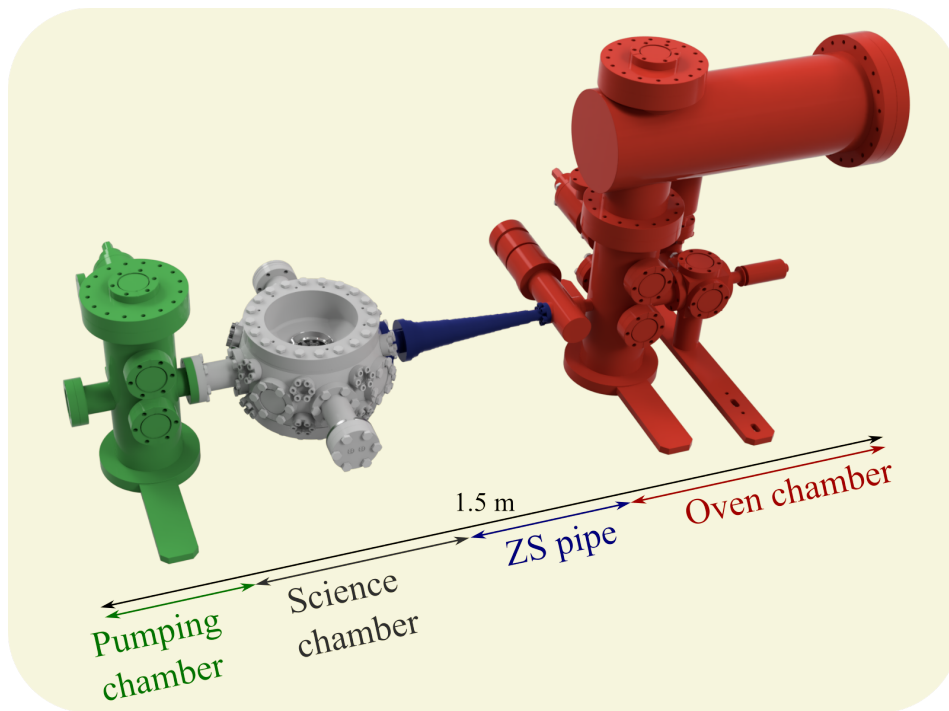Figure 4.1: View of whole vacuum chamber system. The vacuum chamber is consist of four sections: pumping chamber (Green), science chamber (gray), Zeeman slower pipe (blue), and the oven chamber (red). The whole length is about 1.5 m.

Our vacuum chamber system is based on a rather standard system for producing Yb quantum gases, and it comprises four sections: oven chamber, Zeeman slower pipe, science chamber, and

pumping chamber, as depicted in Fig. 4.1. In particular, the science chamber is specially designed for experiments of the Rydberg atom detection and optical tweezer arrays, based on a commercial chamber (Kimball Physics, MCF800-ExtOct-G2C8A16) with two ICF203, eight ICF70 and sixteen ICF34 flanges. Two reentrant viewports are mounted on the ICF203 flanges on top and bottom, hosting high-NA objective lenses for high-resolution imaging, optical tweezer arrays, and site-resolved manipulation (Section 4.1.3). Electrical feedthroughs and a MCP (Hamamatsu photonics F4655-11) for Rydberg state detection are attached to the chamber (Section 4.1.4). Many viewports allow optical access for laser cooling, internal state excitation, absorption and fluorescence imaging, and further optical trapping.

The science chamber is maintained at ultra-high vacuum as 3.5×10^{-11} Torr by two ion pumps and two Ti:sublimation pumps. The pressure at the pumping chamber and the oven chamber is measured by an ion gauge.

4.1.2   Magnetic field

For generation of magnetic field, one pair of anti-helmholtz coils for MOT, three coils for Zeeman slower, and three pairs of helmholtz coils for magnetic compensation is installed. The design value of the magnetic field at the center of the chamber is summarized in Table 4.1. The direction of current for compensation coils is switchable by an H-bridge circuit.

Table 4.1: Design values of magnetic coils used for experiments are summarized. Number of turns indicates that of one side coil. The row for MOT coil includes values for both anti-helmholtz and helmholtz configurations.

	Number of turns	Configuration	Magnetic field
xy compensation	70	Helmholtz	$0.5\,\mathrm{G/A} \times I$
z compensation	40	Helmholtz	$3.4\,\mathrm{G/A} \times I$
MOT coil	42×14	Anti-helmholtz	$11.6\,\mathrm{(G/cm)/A} \times I$
		Helmholtz	$42.7\,\mathrm{G/A} \times I$

4.1.3   Objective lens

For the collection of fluorescence photons and focusing of the trap beam, an objective lens from Special Optics is held below the science chamber. This lens is designed to achieve diffraction limited performance for 532 nm and 556 nm light. The numerical aperture (NA) and working distance (WD) is 0.60 and 20.25 mm, respectively. The drawing provided by Special Optics is shown in the upper left of Fig. 4.2. Because the high-NA lens needs subtle adjustment of alignment, we mounted it on an assembly of two stages, one for pitch and yaw adjustment (Newport 9082-V-M), and the other for 3 axis translation (Suruga B71-80-C), as depicted in the left of Fig. 4.2.

We assess the performance of the lens in prior to the installation using a pinhole with the radius 500 nm. We illuminate back side of the pinhole by 532 nm laser and collect and focus the
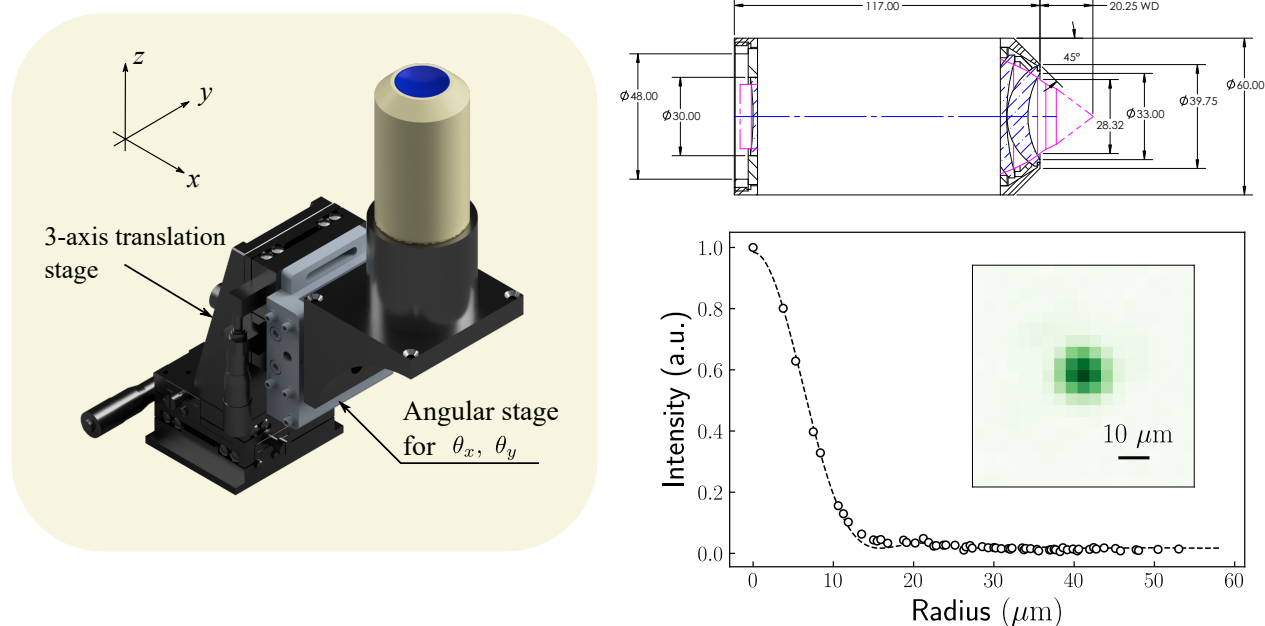
Figure 4.2: (Left) Illustation of the objective lens mounted on stages for adjustment. Five-axis stage for adjustment of angular direction and three-axis stage is assembled. (Right) The upper panel shows the drawing of the objective lens. This drawing is offered from Special Optics. The lower panel shows the the image of light scattered from a pinhole with a radius 500 nm. The inset shows the radial dependence of the PSF and fitted curve by the airy disk function.

scattered light onto a CCD camera (FLIR Chameleon3). We use a $f = 500$ nm lens for focusing. The magnification of the imaging system is 25. We fit the obtained point spread function (PSF) by the airy disk function (Eq. (4.21)) and get the estimation value of NA 0.51. Though this value is not as high as the specification value, it is still enough high for our situation of imaging $1 \sim 10\,\mu$m apart atoms.

4.1.4 Electrodes and Micro-channel plate

Eight electrodes are equipped inside the chamber in order to control electric fields (Fig. 4.3). They compensate for stray electric fields at the position of the atoms as well as ionize Rydberg atoms, enabling high sensitive detection of Rydberg states by the MCP (Hamamatsu Photonics, F4655–11). The center of the chamber is shielded from electric fields created by the MCP and the feedthroughs with a grounded mesh on the MCP side and an aluminum plate on the feedthrough side. The eletrodes are connected to a digital–analog converter through the feedthroughs (Access I/O, USB-AO16-8E-10B). We adjust each voltages to compensate or apply weak electric fields. For ionization of Rydberg atoms, we use another high-voltage supply which is switchable with DAC output by a TTL, using an analog switch (Analog Devices, MAX319). We apply -15 V to four electrodes in MCP side and 30 V to left four in the other side, which creates about 18 V/cm electric fields
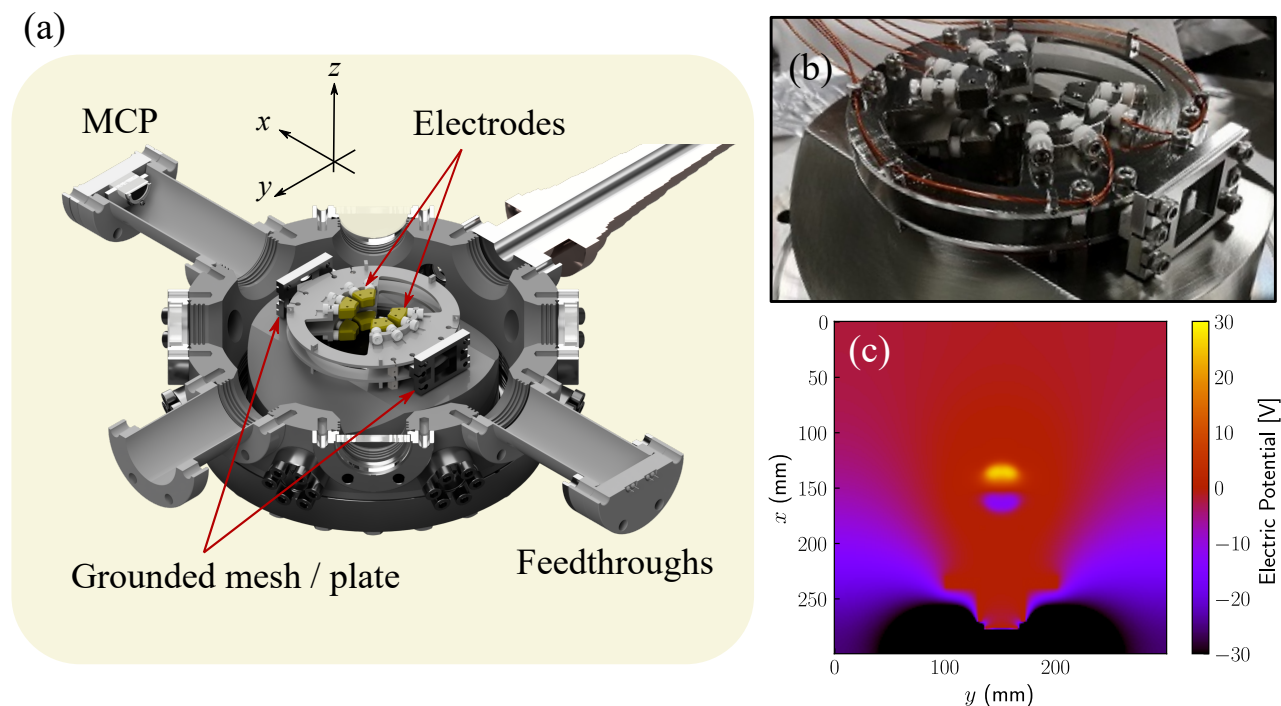
Figure 4.3:   (a) CAD graphic of inside of the chamber. Eight electrodes, two grounded meshes, MCP, and feedthroughs are equipped to the science chamber. (b) Corresponding photograph taken before the installation to the chamber. (c) Electric potential map in xy-plane when the voltages for each electrodes are adjusted to ionization settings: $-15\,\mathrm{V}$ for four electrodes in MCP side and $30\,\mathrm{V}$ for four in the other side.

toward MCP direction at the atom position. Fig. 4.3.(c) shows the electric potential map in xy-plane calculated by SIMION®. The relation between the applied voltages and strength of electric fields is also simulated. Figure 4.4 shows the electric field dependence on each x, y, z direction when $\pm 1\,\mathrm{V}$ voltages are applied to oppositing four electrodes along that direction. The computed electric fields at the atom position is $E_x = 79.7\,\mathrm{mV/mm}$, $E_y = 58.1\,\mathrm{mV/mm}$ and $E_z = 44.7\,\mathrm{mV/mm}$. As is already discussed in section 3.2.2, Rydberg atoms are highly sensitive to electric fields. In our setups, the dielectric window is close to the atom and it may cause fluctuation of electric fields by charging effects. In order to prevent this, both windows on top and bottom side of the chamber is processed with Indium-Tin-Oxide (ITO) coating. The inside surface of windows and the metal chamber is electrically connected by aluminum foils before the installation.

4.1.5   Acousto-Optic Deflectors

We use an acousto-optic deflector (AOD, A&A DTSX-400-532) to generate a tweezer array. AOD diffracts an input beam by angle θ linearly dependent on the applied frequency: $\theta = (\mathrm{d}\theta/\mathrm{d}f)f$. The linear coefficient is measured to be $0.8\,\mathrm{mrad/MHz}$, which agrees with specification data from the company. When the RF contains multiple frequency components, the beam branches to corresponding angles, as depicted in Fig. (4.5). This multitone RF is generated by an arbitrary waveform
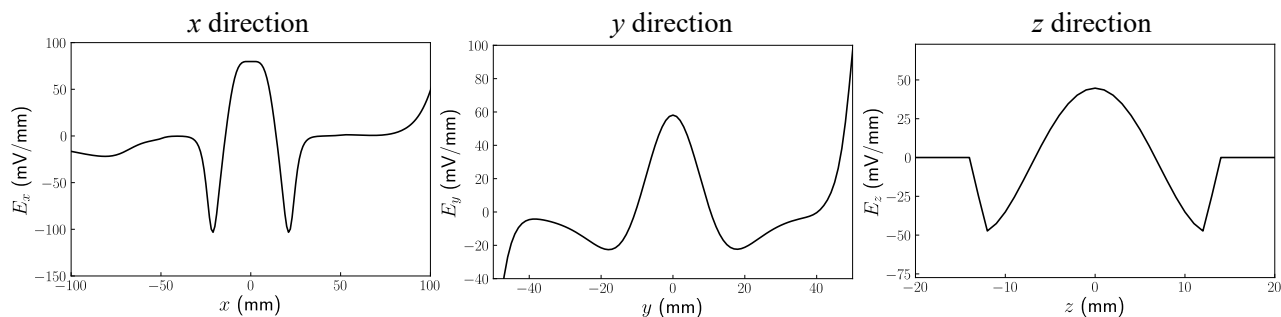
Figure 4.4: Electric field strength dependence on position when ±1 V voltages are applied to oppositing electrodes along each axis.
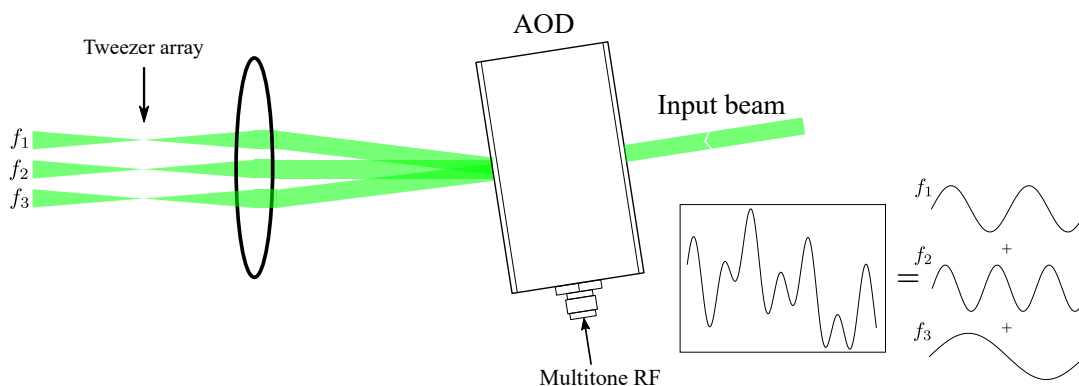

Figure 4.5: Shematic illustration of principle of generation of tweezer array by AOD. Input beam is diffracted by an angle linearly dependent on a frequency of the applied RF.

generator (AWG, Spectrum M4i.6622-x8) directly connected to a computer's motherboard through a PCIe slot. The AWG outputs voltage with sampling rate 625 MHz and 16-bit resolution. The output voltage can be written as

$$V(t) = \sum_{k=1}^{N} A_k \cos(2\pi f_k t + \phi_k) \tag{4.1}$$

A_i and f_i determine the power and the position of the tweezer array, respectively. Though the tweezer beams are not explicitly related to the relative phase ϕ_k, we must take care because it can change the efficiency of the diffraction. The limitation on maximum voltage by AWG or AOD requires low peak-to-average power ratio (PAPR) defined as $\max(V^2)/\langle V^2 \rangle$. For example, if amplitudes and phases for all the freuquencies are chosen to be constant ($A_k = A, \phi_k = 0$), the peak voltage is AN and thus the amplitudes and power for each frequencies decays as $1/N$ and $1/N^2$ respectively. This results in decay of total diffraction efficiency as $N \times 1/N^2 = 1/N$.

Several algorithms to reduce the PAPR for equally separated frequencies and constant amplitudes ($f_k = f_0 + k\delta f, A_k = A$) are known whilst algorithms to achieve analytically minimum value for
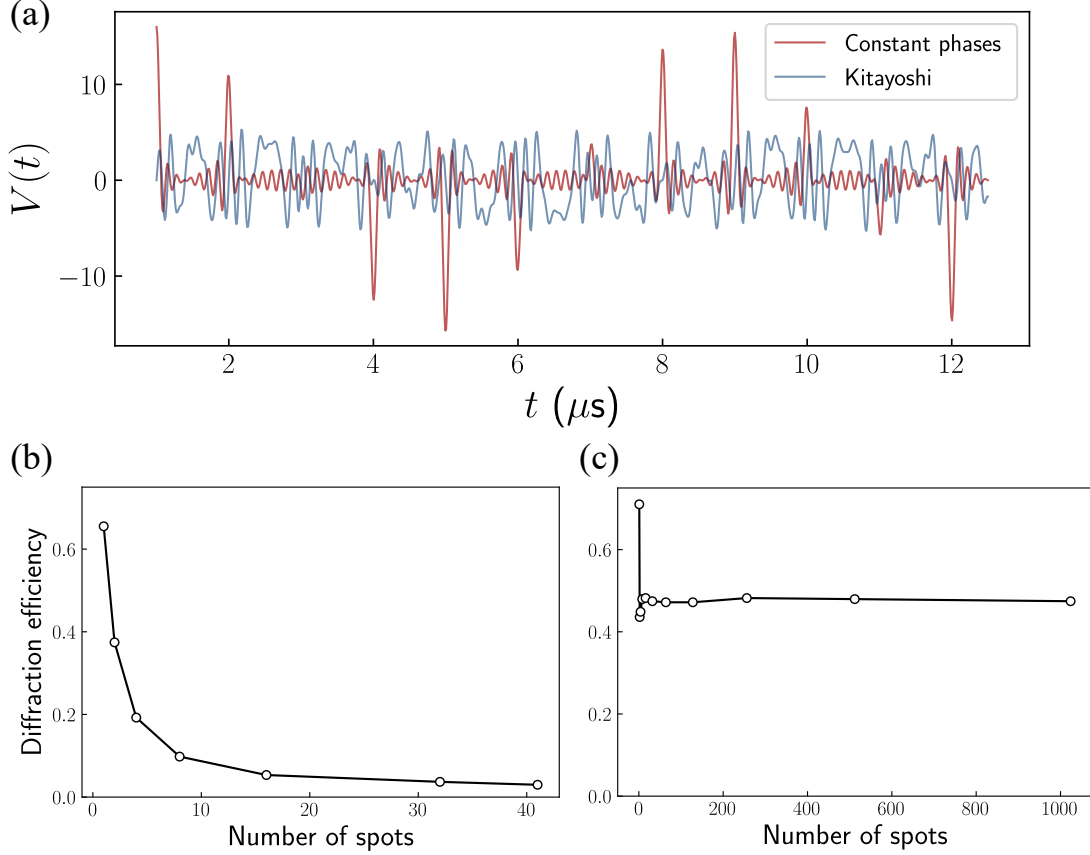
Figure 4.6:   (a)Calculated voltage amplitudes for $N = 16, f_0 = 80\,\mathrm{MHz}, \delta f = 1\,\mathrm{MHz}$ and (red) constant phases $\phi_k = 0$ or (blue) Kitayoshi algorithm $\phi_k = \pi k(k+1)/N$. (b) and (c) shows the measured diffraction efficiency against the number of spots of lights for constant phases and kitayoshi algorithm, respectively.

general cases are not known. For the calculation we use complex representation of the amplitude

$$V(t) = A \sum_{k=1}^{N} \exp(2\pi \mathrm{i}(f_0 + \delta f k)t + \mathrm{i}\phi_k). \tag{4.2}$$

We note Eq. (4.1) and Eq. (4.2) should be distinguished, while we ignore the difference for the sake of simplicity. PAPR is given by

$$\max_t \left(1 + \frac{2}{N} \sum_{l>k} \cos\left(2\pi(l-k)\delta f t + \phi_l - \phi_k \right) \right). \tag{4.3}$$

The basic idea is to make the summation from $l = k + 1$ terms in Eq. (4.3)

$$\sum_{k=1}^{N-1} \cos(2\pi \delta f t + \phi_{k+1} - \phi_k) \tag{4.4}$$

minimum by making the phase term $\phi_{k+1} - \phi_k$ equally separated in $[0, 2\pi)$:

$$(\phi_{k+1} - \phi_k) - (\phi_k - \phi_{k-1}) = \frac{2\pi}{N}. \tag{4.5}$$

This leads to the choice of initial phases

$$\phi_k = \frac{\pi}{N}k(k+1), \tag{4.6}$$

which is known as **Kitayoshi algorithm** [108]. Figure 4.6(a) shows the calculated $V(t)$ for $N = 16$, $f_0 = 80\,\mathrm{MHz}$, $\delta f = 1\,\mathrm{MHz}$ for constant phases (red) and the Kitayoshi algorithm (blue). In our experiments this algorithm is adopted to acquire a higher efficiency of diffractions. Figure 4.6(b) and (c) shows the measured diffraction efficiency of AOD for constant phases and the Kitayoshi algorithm, respectively. One can see significant improvements of diffraction efficiency by Kitayoshi algorithm which keeps almost 48% while it decays as $1/N$ in the case of constant phases as discussed above.

4.2 Laser sources

4.2.1 398.9 nm ($^1S_0 \leftrightarrow {}^1P_1$)

Zeeman slower

The 398.9 nm laser for Zeeman slowing beam is obtained by second harmonic generation (SHG) of 797.8 nm from Toptica TA-Pro. A bow-tie ring cavity with a $\mathrm{LiB_3O_5}$ (LBO) crystal is used for the SHG (Fig. 4.7). The calculated finnese of the cavity $\mathcal{F}_{\mathrm{calc}}$ is

$$\mathcal{F}_{\mathrm{calc}} = \frac{\pi\sqrt{R}}{1 - R} = 368, \tag{4.7}$$

$$R = R_1 R_2 R_3 R_4 T_{\mathrm{LBO}}, \tag{4.8}$$

where R_i is the reflectance of the M_i mirror and T_{LBO} is the transmittance of the LBO crystal. The specification of R_i and T_{LBO} is $R_1 = 99\%$, $R_2 = R_3 = R_4 = 99.85\%$, and $T_{\mathrm{LBO}} = 0.1\%$. The distance between M_1 and M_2 (L_1), M_2 and M_3 (L_2), and M_3 and M_4 (d) is 237 mm, 177 mm, and 114 nm, respectively. The free spectrum range (FSR) of the cavity is calculated to be 420 MHz. Beam radius at the center of the LBO is 36 μm. The finesse of the cavity is also estimated from the transimission signal of the cavity: $\mathcal{F}_{\mathrm{exp}} = 375 \pm 25$. The cavity length is locked to the resonance by piezo controlled M_2 mirror using Hänsch–Couillaud technique. The relation between the power of the input fundamental laser P_{in} and obtained second harmonic laser power P_{SHG} is given by

$$P_{\mathrm{SHG}} = E_{\mathrm{nl}} P_{\mathrm{ic}}^2 \tag{4.9}$$

$$P_{\mathrm{ic}} = \frac{T_1 \eta P_{\mathrm{in}}}{\left(1 - \sqrt{(1 - T_1)(1 - l_{\mathrm{cav}})(1 - E_{\mathrm{nl}} P_{\mathrm{ic}})}\right)^2}, \tag{4.10}$$
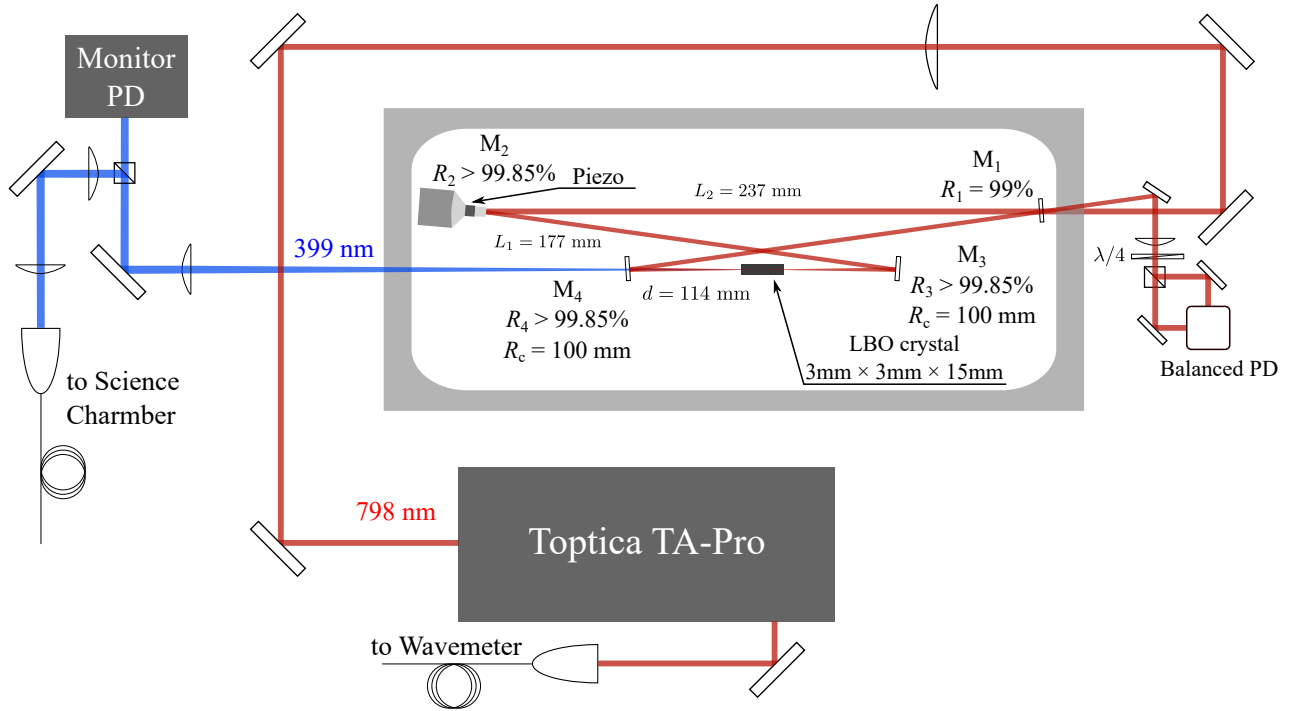
Figure 4.7: Optical system for generation of 399 nm laser from 798 nm laser output from Toptica TA-Pro. LBO crystal is placed at the center of the bow-tie ring cavity to generate second-harmonic wave.

where P_{ic}, l_{cav}, η, E_{nl}, T_1 is the intra-cavity power of the fundamental laser, the loss caused from except M_1, the cavity coupling efficiency, the nonlinear coupling efficiency of the crystal, and transmittance of M_1, respectively. η is $79 \pm 5\,\%$. The cavity is contained inside a box evacuated by a scroll pump, in order to prevent aging of the crystal by a chemical reaction with dust particles fostered by UV light.

The input and the output power just after the initial installation were $P_{in} = 1.8\,$W and $P_{SHG} = 500\,$mW. We note the performance of SHG get worse gradually day by day and typical values for experiments in this thesis are $P_{in} = 1.5\,$W and $P_{SHG} = 250\,$mW.

The frequency of the laser is stabilized with a commercial wavemeter (High-Finesse, WS-8) by piezo actuator of the grating of seed laser.

Probe beam

The $^1S_0 \leftrightarrow {}^1P_1$ transition is also used for the probe of absorption imaging, two-photon excitation to Rydberg states, and removal of the $^1S_0$ atoms. We use SHG of home-made external-cavity diode laser (ECLD) and tapered-amplifier (TA) system for these purposes. Commercial waveguided Periodically Polarized Lithium Niobate (PPLN) crystal (NTT electronics) is used for the SHG. The frequency is stabilized with a wavemeter, as well as the Zeeman slowing beam.

4.2.2 555.8 nm ($^1S_0 \leftrightarrow {}^3P_1$)

The 555.8 nm laser for $^1S_0 \leftrightarrow {}^3P_1$ transition is derived by a SHG of tapered-amplified diode laser (Toptica TA-Pro). A waveguided PPLN crystal is used for the SHG. This laser is used for the MOT and fluorescence imaging. The frequency of the fundamental laser with a tunable offset by a fiber Electro-Optic Modulator (EOM) is stabilized to a Ultra-low expansion (ULE) glass cavity by a Pound–Drever–Hall (PDH) technique. The measured finesse of the cavity for 1112 nm by cavity-ring-down method is 19,000. The FSR of this cavity is 1.5 GHz. A simplified optical setup before the fiber to the science chamber is shown in Fig. 4.8. The MOT laser for the horizontal directions (xy-axis) and the vertical direction (z-axis) is separated before the fiber by a polarized-beam splitter (PBS) and controlled individually by two Acousto-Optic Modulators (AOMs). For the AOM for probe laser, double-pass configuration is adopted to widely tune the frequency.

4.2.3 507 nm ($^1S_0 \leftrightarrow {}^3P_2$)

The excitation laser from $^1S_0$ to $^3P_2$ state with wavelength 507 nm is derived by SHG (waveguided PPLN crystal) of tapered-amplified home-made ECLD. The frequency of the laser is stabilized to a high-finesse ULE cavity to achieve ultranarrow linewidth of the transition. This cavity is the same as the one for 1112 nm. The finesse for 1014 nm calculated from the reflectance of mirrors is 500,000, which well agrees with measurement by cavity-ring-down method. The error signal generated by PDH technique is feedbacked to current and piezo voltage controller of seed laser from Vescent Photonics. The laser couples to the cavity is modulated by two EOMs. One is a fiber EOM to add an offset frequency and the other is a bulk EOM for generation of PDH error signal (QuBIG). The bulk EOM is used to avoid residual amplitude modulation (RAM) which can cause fluctuation of frequency set point. The linewidth is estiamted to be 200 Hz from the PDH error signal at 1014 nm.

4.2.4 325 nm ($^3P_2$ to Rydberg states)

For the excitation from $^3P_2$ atoms to Rydberg states, an Ultra-Violet laser with a wavelength of 325 nm is used. This laser is derived by SHG of tapered-amplified ECDL. We use interference filter for tuning of lasing wavelength. We call such a diode laser Interference Filter type external cavity Diode Laser (IFDL). The seed laser is pre-amplified before the TA by an injection locking to about 25 mW as shown in Fig. 4.9. The second-harmonic wave is generated by a bow-tie ring cavity and a non-linear crystal similarly as the Zeeman slowing beam. In this case $Ba_2B_2O_4$ (BBO) crystal is used[1]. The calculated and measured Finesse of the cavity is $\mathcal{F}_{calc} = 447$ and $\mathcal{F}_{exp} = 431$.

4.2.5 770 nm ($^3P_2 \leftrightarrow {}^3S_1$)

770 nm laser for repumping of $^3P_2$ atoms to the ground state is emitted by a commercial IFDL (OptoQuest). The frequency of the laser is stabilized with a wavemeter.

---

[1]We tried LBO crystal first, but we could not get enough conversion efficiency.
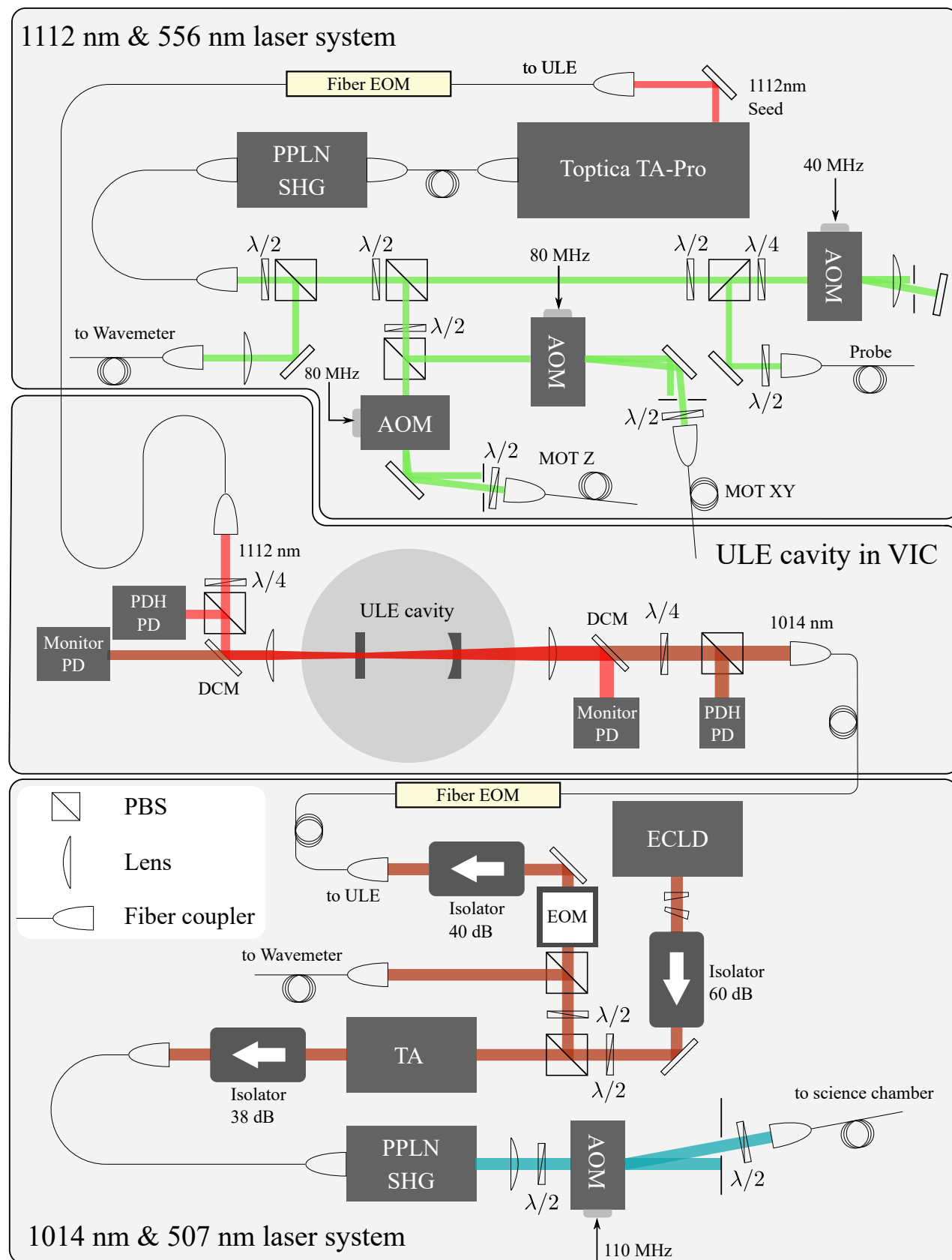
Figure 4.8: Simplified optical setups for the 1112 nm–555.8 nm laser system and 1014 nm–507.4 nm laser system, both of which is locked to the same ULE cavity. The frequencies of the AOM for 556 nm laser in the figure shows the typical values for the loading of MOT.
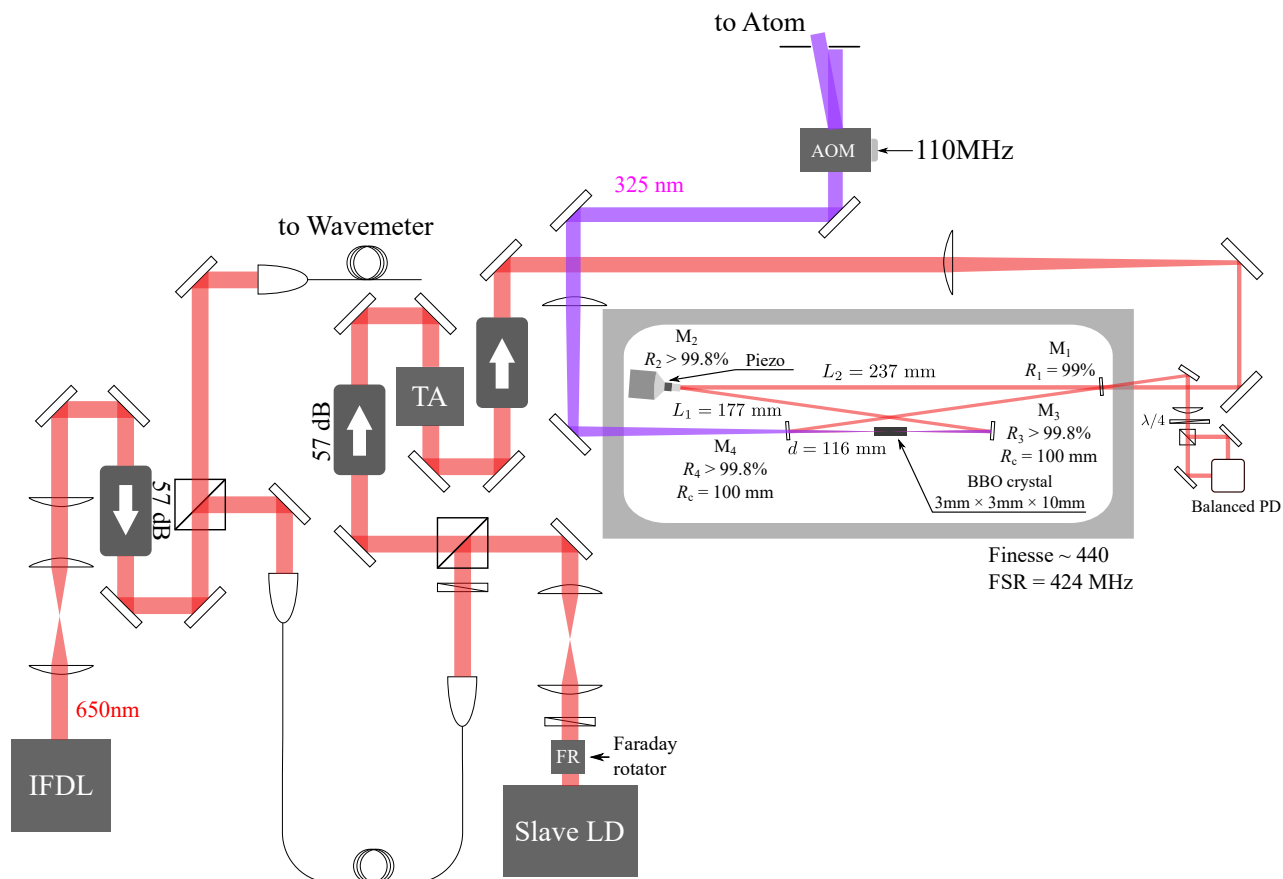
Figure 4.9: Simplified optical setups for the 650 nm–325 nm laser system. The 325 nm laser is obtained as the second harmonic of 650 nm laser. 650 nm light from home–made IFDL is amplified by injection lockng and TA. FR in the figure denotes Faraday rotator.

4.2.6 394 nm (^{1}P$_1$ to Rydberg states)

394 nm laser is used for two-photon excitation to the Rydberg states via ^{1}P$_1$ state. This UV laser is derived from an ECDL directly. The frequency is stabilized with a wavemeter.

4.3 Optical tweezer array

4.3.1 Optical dipole traps

An oscillating external laser field $e^{i\omega t} \boldsymbol{E}$ induces the dipole moment of atom as $\boldsymbol{d} = \alpha(\omega)\boldsymbol{E}$ where $\alpha(\omega)$ is the polarizability of the atom. The atom feels the potential from the interaction between the dipole and the field which is given by

$$V_{\text{dip}} = -\frac{\eta_0}{2} \text{Re}\left(\alpha(\omega)\right) I(\boldsymbol{r}).$$

$$(4.11)$$

$\eta_0 \equiv 1/\epsilon_0 c \simeq 377\,\Omega$ and $I(r)$ are vacuum wave impedance and intensity of the laser, respectively [90]. The gaussian beam therefore gives the potential such as

$$V(r,z) = \frac{V_0}{1 + (z/z_r)^2} \exp(-r^2/2w_0^2) \tag{4.12}$$

where w_0 and $z_r = \pi w_0^2/\lambda$ is the beam radius at the focus and the rayleigh length, respectively. The beam radius w_0 and the NA of the focusing lens is related as $w_0 = \lambda/\pi\mathrm{NA}$ in the difraction-limited condition, which becomes comparable to the wavelength λ for high-NA lenses. By expanding V by r and z up to the second order, we are able to define radial and axial trapping frequency ν_r and ν_z as

$$V(r,z) = V_0 + \frac{m\nu_r^2}{2}r^2 + \frac{m\nu_z^2}{2}z^2 + O(r^2)O(z^2), \tag{4.13}$$

$$\nu_r = \sqrt{\frac{4V_0}{mw_0^2}}, \nu_z = \sqrt{\frac{2V_0}{mz_r^2}}, \tag{4.14}$$

where m is the mass of the atom.

4.3.2 Light-assisted collision
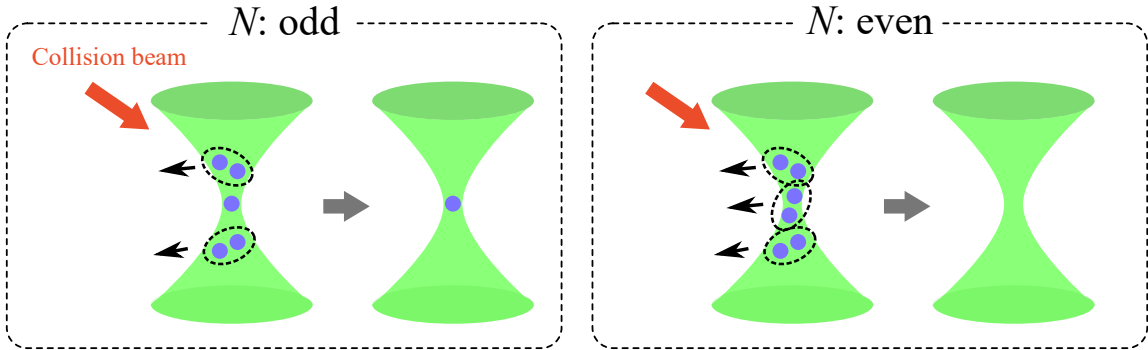
Figure 4.10: Illustration of the principle of light assisted collision to prepare a single atom. Two-body losses makes the the number of atoms 0 or 1 reflecting the initial parity.

To prepare a single atom in an optical trap, inelastic collisions between S state and P state are caused by red-detuned light which removes pair of atoms, so called collisional blockade effect. The rate for this event to occur is given by βN^2 where N denotes the number of atoms inside a trap. β is a collisional loss coefficient. It is known that β is proportional to inverse of the trap volume: $\beta \propto 1/V$ [109]. If the trap volume is small enough like the case in wavelength-scaled optical tweezers, this collisions become the dominant loss mechanics. This pairwise losses lead to a resultant zero or single atoms reflecting the parity of the initial number of atoms (Fig. 4.10) [110].

Figure 4.11: $4f$-setup of absorption imaging optical system used in our experiments. Absorption of resonant light by atoms is imaged on the conjugate plane (camera plane).

4.4 Detection of atoms

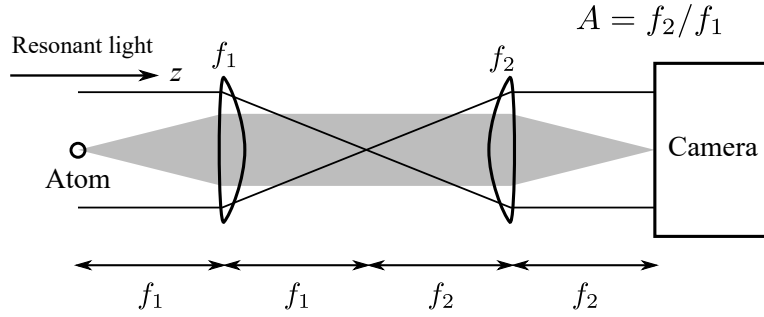### 4.4.1 Absorption imaging

Absorption imaging technique is widely used in cold atom experiments to acquire the information of spatial distribution of density of atomic clouds. Though our target of studies is single atoms in a tweezer array, we frequently use absorption imaging of atomic clouds for adjustment or preliminary spectroscopies. In our experiments, we use $4f$-configuration optical setup for imaging as depicted in Fig. 4.11. The intensity distribution $I_0(x, y)$ of the probe laser with the wavelength λ changes to $I(x, y)$ by absorption by atoms, which is given by

$$I(x, y) = I_0(x, y) \exp\left(-\sigma_0 \int n(\boldsymbol{r})\mathrm{d}z\right), \tag{4.15}$$

where $\sigma_0 = 3\lambda^2/2\pi$ is the absorption cross section for a resonant light and $n(\boldsymbol{r})$ is the density of atom at a point $\boldsymbol{r}$. The camera at the image plane observe the same distribution of the probe intensity except a magnification of $A \equiv f_2/f_1$:

$$I_{\mathrm{cam}}(x, y) = \frac{1}{A^2}I(\frac{x}{A}, \frac{y}{A}). \tag{4.16}$$

The density distribution integrated along z axis (probe laser axis) is derived by dividing two images taken with (trans image) and without (flat image) atoms as

$$\int n(\frac{x}{A}, \frac{y}{A})\mathrm{d}z = -\frac{1}{\sigma_0}\ln\left(\frac{I_{\mathrm{cam}}^{\mathrm{w}}(x, y)}{I_{\mathrm{cam}}^{\mathrm{w/o}}(x, y)}\right). \tag{4.17}$$

As a experimental protocol, we get discretized data of $I_{\mathrm{cam}}^{\mathrm{w}}$ and $I_{\mathrm{cam}}^{\mathrm{w/o}}$ by taking background image of the camera without probe light (dark image) in addition to trans and flat images. Let us denote the counts of the trans, flat, and dark images at the (i, j)-th pixel as $T_{i,j}$, $F_{i,j}$, and $D_{i,j}$. The density distribution corresponding to the (i, j)-th pixel is given by

$$\int n(\frac{x_i}{A}, \frac{y_j}{A})\mathrm{d}z = -\frac{1}{\sigma_0}\ln\left(\frac{T_{i,j} - D_{i,j}}{F_{i,j} - D_{i,j}}\right). \tag{4.18}$$

x_i, y_j indicates the physical coordinate of (i, j)-th pixel. The total number of atoms N is calculated by summing up all the density distribution of each pixels:

$$N = \int n(\boldsymbol{r}) \mathrm{d}\boldsymbol{r}^3 \tag{4.19}$$

$$= -\frac{\Delta s}{A^2} \sigma_0 \sum_{i,j} \ln\left(\frac{T_{i,j} - D_{i,j}}{F_{i,j} - D_{i,j}}\right), \tag{4.20}$$

where Δs is the area of a pixel.

4.4.2   Fluorescence imaging

$4f$-optical setup depicted in Fig. 4.11 is also used for the fluorescence imaging. The shadow in this case corresponds to the fluorescence from atoms. Arising from the diffraction of lights, the light emitted from an ideal point light source is broadened by to a function with a finite width, which is called a **Point Spread Function** (PSF). The obtained image on the camera becomes the convolution between the ideal image and the PSF. In other words, PSF is a green function of the propagation of light through an imaging system. The intensity of PSF under a paraxial approximation $\sin\theta \sim \theta$ and $\cos\theta \sim 1$ and assumption that the dipole is oriented perpendicular to the objective lens is

$$\text{const.} \times \frac{J_1(r/r_0)^2}{(r/r_0)^2}, \tag{4.21}$$

$$r_0 = \frac{M\lambda}{2\pi\mathrm{NA}} \tag{4.22}$$

where θ and $J_1(\cdot)$ denotes the the maximal half-angle of the cone of light that can enter the lens and first-order Bessel function, respectively [111]. Equation (4.21) is known as the **airy disk function**.

   The finite width of the PSF set the lowest limit of a distance between two point light sources that can be distinguished. There are several criteria whether two images are distinguishable or not. One of the most frequently addressed one is the **Rayleigh's criterion**, in which the first minimal point of the PSF is the resolvable minimum distance. Consequently, assuming incoherence of two light sources, the resolution of the imaging system is given by

$$0.61\frac{\lambda}{\mathrm{NA}}. \tag{4.23}$$

Here we used that the first minimal point of the airy disk function $(J_1(x)/x)^2$ is $x = 3.83$.

4.4.3   Ionization detection of Rydberg atoms

For the detection of Rydberg states, a strong electric field $E = 17\,\mathrm{V/cm}$, or $E = 3.3 \times 10^{-9}$ in atomic units, is applied to atoms along the x-drection. The potential of the Rydberg electron is given by

$$V = -\frac{1}{r} - Ex, \tag{4.24}$$

which create a saddle point of the potential with a height $-2\sqrt{E}$.

Roughly speaking, if the energy of the electron exceeds this peak, the electron escapes and the atom is ionized. Assuming a hydrogenic atom and neglecting the Stark shift, the n-th eigenenergy of the electron is $E_n = -1/(2n^2)$, and thus we obtain the field-ionization condition:

$$-2\sqrt{E} < -\frac{1}{2n^2} \Rightarrow E > \frac{1}{16n^4}. \tag{4.25}$$

For $E = 17\,\text{V/cm}$, the minimum n satisfies Eq. (4.25) is 66. In practice, interactions between the Rydberg electron and the inner electrons, the electric field (Stark shift), and ions (Penning ionization [112]) should be also taken into account, but we don't here. In fact, we observed ionization of $n = 50$ Yb Rydberg states for atomic ensembles by the $E = 17\,\text{V/cm}$ electric field.

We apply $-2\,\text{kV}$ to the MCP to detect ions, supplied from Stanford Reseach Systems PS325/2500V-25W. This $-2\,\text{kV}$ is also divided to 1/5 and applied to between the anode and the MCP. We apply a voltage lower than the specification value $-2.5\,\text{kV}$, with which the gain of the MCP is 5×10^7, to avoid the aging of the MCP. The output from the MCP is amplified by a differential amplifier (NF electronics 5307) by 50 times. The amplified signal is acquired by a field programmable gated array (NI PXI-6733) and sent to a computer. Figure 4.12 shows the electrical setup of the MCP.

When the gain of the MCP is 5×10^7, the number of detected ions N_{ion} and the amplified signal voltage V_{MCP} are related as

$$(5 \times 10^5) \times 50 \times e N_{\text{ion}} = \int \frac{V_{\text{MCP}}}{R} dt, \tag{4.26}$$

$$\Rightarrow N_{\text{ion}} = \alpha S \tag{4.27}$$

where $R = 50\,\Omega$ and e is the impedance of the system and the charge of an electron ($1.602\,176\,634 \times 10^{-19}\,\text{C}$). $S \equiv \int V_{\text{MCP}} dt$ is the ionization signal. The conversion coefficient α is calculated to be

$$\alpha = 49.93\,(\text{V} \cdot \mu\text{s})^{-1} \tag{4.28}$$
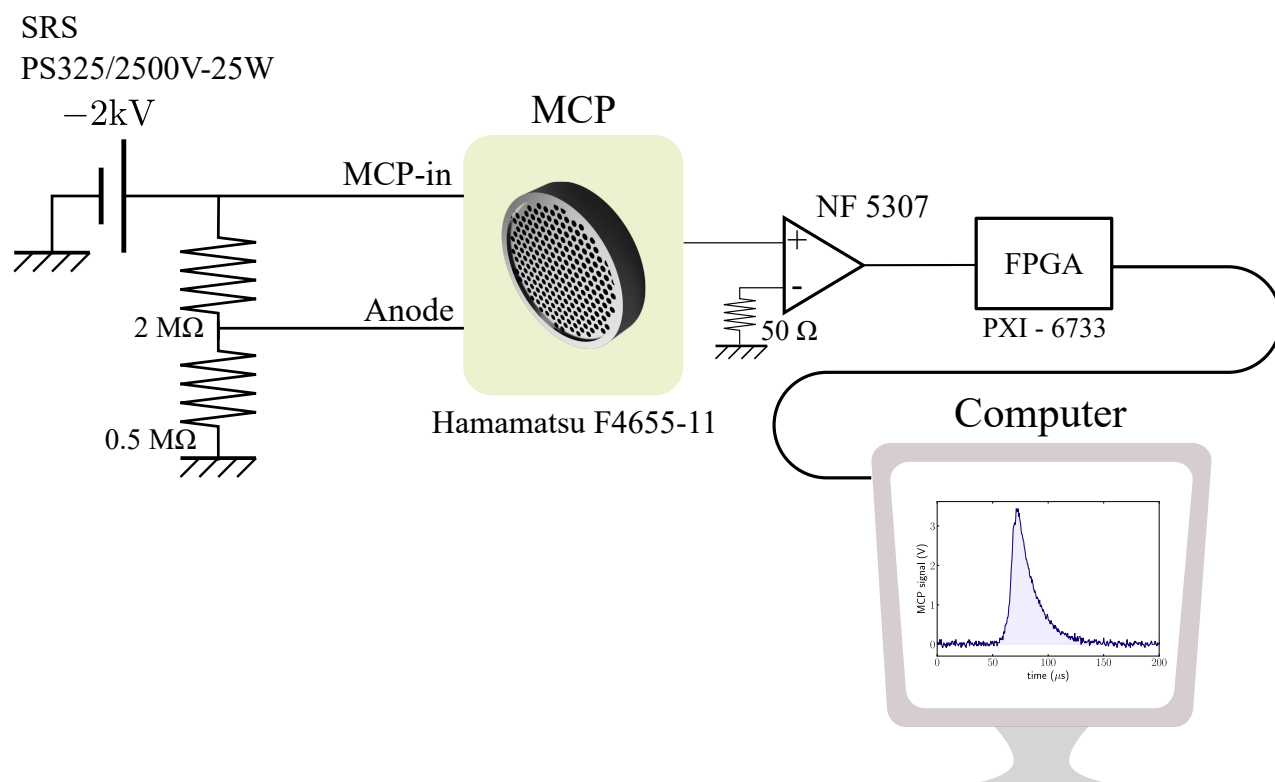
Figure 4.12: An electrical configuration around the MCP. $-2\,\mathrm{kV}$ and $0.4\,\mathrm{kV}$ supplied from Stanford Reseach Systems PS325/2500V-25W is applied to MCP in and anode. The output from the MCP is amplified by a differential amplifier (NF 5307) and acquired by a DAC (NI PXI-6733).

Trapping and imaging of single atoms

5.1 Optical setups for trapping and imaging

We describe the optical setup regarding the trapping and imaging of single atoms. The OT with a wavelength of 532 nm is derived from a diode-pumped solid-state laser (Coherent, Verdi V-10). The laser passes through a single-mode fiber in order to filter the spatial mode and stabilize the pointing. An AOM is placed before the fiber for the purpose of switching and controlling the overall power of OTs. After the fiber, two AODs are placed horizontally (AOD(H)) and vertically (AOD(V)) at the imaging plane of the standard $4f$ configuration, consisting of lens pairs with a focal length of 100 mm and 150 mm, and 150 mm and 1000 mm. The deflection angle of the AOD is 0.8 mrad/MHz, resulting in 2.4 μm/MHz at the position of the atoms. The mirror after the $f = 1000$ lens is mounted on a finely adjustable mount (Agilis, M100-L). The next mirror transmits tiny fraction of the light and it is used for a monitor of the pointing and power homogeneities of the array. The beam is then launched toward the objective lens passing through a dichroic mirror, and focused down to a sub-micron waist. OTs pass through a PBS for the cleaning of the polarization, which transmits the polarization along the Zeeman slower direction. The mirror for launching and the previous mirror is mounted on an assembly of two translation stages (stage(L) and stage(S)) for orthogonal directions, which allows the lateral shift of OT beams. The optical elements for OT beams are placed on the ground vibration isolation table, which we call 1F for convenience.

The fluorescence from the atoms is collected by the objective lens and reflected by the dichroic mirror. After that, half of the photons are reflected by a non-polarizing beam splitter (NPBS) and focused on the EMCCD camera by a lens with a focal length of 400 mm. The focal length of the objective lens is 20 mm, and therefore the magnification of the imaging system is 20. The NPBS combines the vertical axis of the MOT beam. This MOT beam is focused on the principal plane of the objective lens to collimate the beam on the atom position. The beam waist is about 1 mm. These systems are constructed on a custom breadboard which we call 2F breadboard.

Figure. 5.1 shows an illustration of the whole optical setups on 1F and 2F and cut-view of the vertical plane.
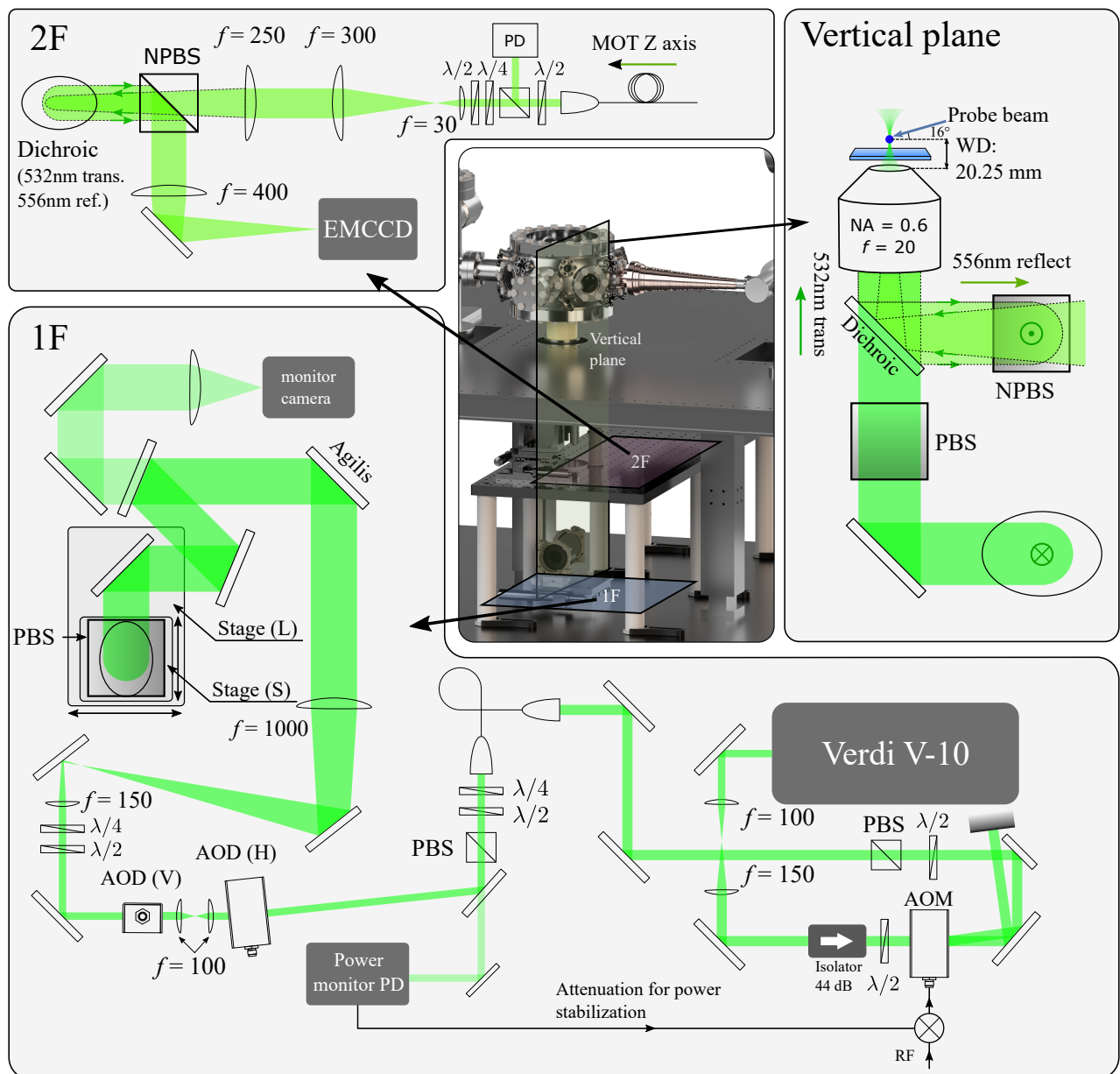
Figure 5.1: Optical paths for the OT beam, fluorescence from the atoms, and the vertical axis of the MOT beam. The OT beam mainly runs on the vibration isolation table (1F), and finally it is launched toward the objective lens passing through a dichroic mirror. The fluorescence from the atoms are reflected by the dichroic mirror and focused on the EMCCD camera on the custom bread board (2F). The path of the tweezer beams and the fluorescence on the vertical plane is also presented here.

5.2   Initial alignemnt

5.2.1   Alignment of OT beam

Figure 5.2: An assembly of the objective lens and its holders. A mirror and an iris is incorporated for the alignment of OT beams temporarily before the installation, which is highlighted by purple squares.

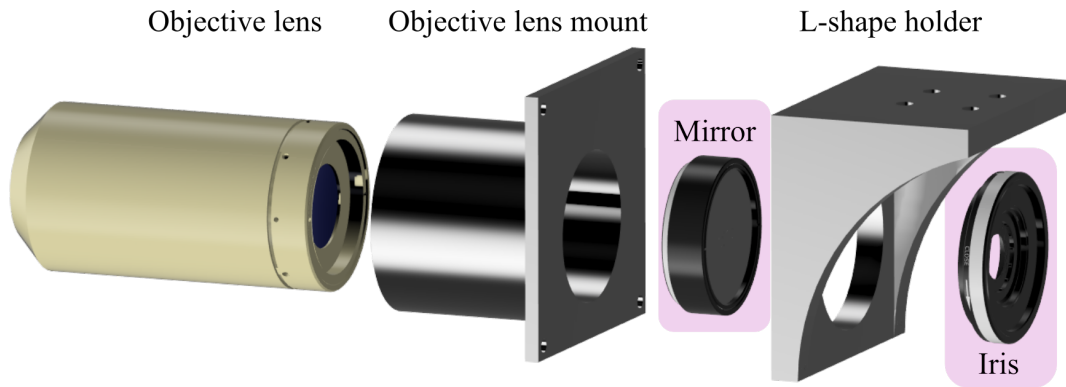The high-NA objective lens is quite sensitive to misalignment of the input beam. The axis of the objective lens and the OT beam should be the same and perpendicular to the window of the chamber. As an initial alignment, we used a mirror and an iris temporarily and aligned the path according to following procedures:

1. Before installing the 2F breadboard, we checked the angle of the window using a guiding beam. We launched the beam to the window and adjusted the angle so that the reflection from the window and the incident beam become overlap. We used an incoherent light source at 532 nm (Thorlabs, CPS32) for this purpose. The whole optical system of the guiding beam is constructed on a small breadboard, allowing us to move it keeping the angle of the beam.

2. We adjusted the angle of the objective lens on the 2F breadboard to be perpendicular to the guiding beam. We used a mirror incorporated to the assembly of the objective lens and holders (Fig. 5.2) to check the reflection. The center of the objective lens and the guiding beam is matched by checking the iris. The guiding beam is expected be the same as the axis of the objective lens by this process. We placed two additional irises on the 2F breadboard to save the axis of the objective lens. This process of the alignment was done before the installation of the 2F breadboard.

3. The mirror and the iris attached to the objective lens were removed. We installed the 2F breadboard below the science chamber.

4. The OT beam is aligned so that it passes through the two irises.

We note the relative position between the objective lens and the science chamber is not taken care much.
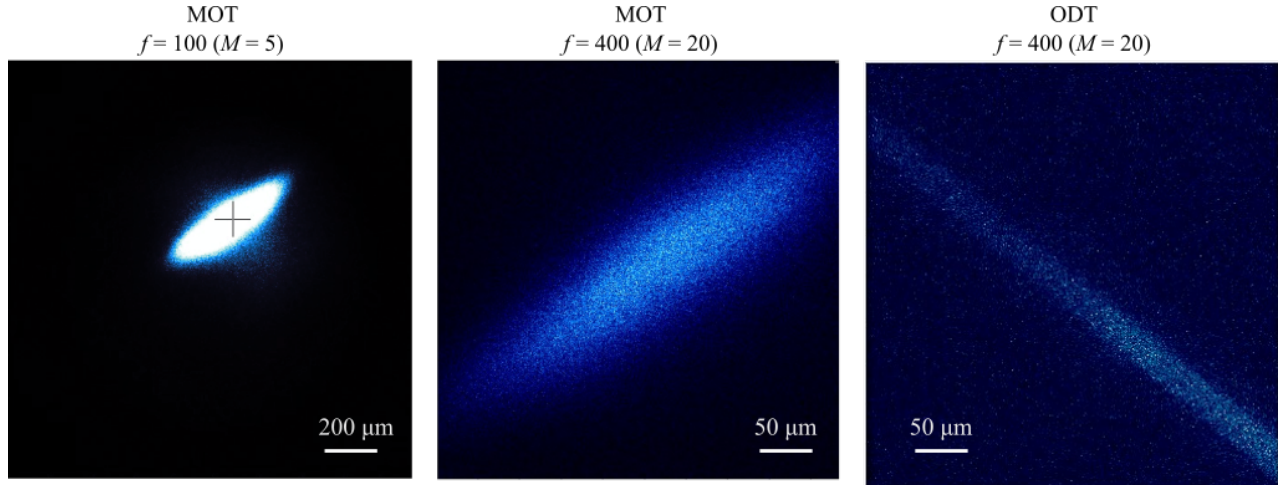
5.2.2   Fluorescence imaging of MOT

Figure 5.3: The obtained fluorescence images of atoms in MOT and an ODT. The left and middle panel shows the image of MOT taken with 5 and 20 magnification. The right panel shows the image of atoms in the ODT with 20 magnification. A crosshair in the left panel shows the position of the guiding beam, corresponds to OT beam position on the camera.

We tried to take a image of MOT by its fluorescence first. Within our setup, however, the reflection of the MOT vertical light also enters the EMCCD camera, as shown in Fig. 5.1. We turn off only the vertical axis of MOT beams and took an image. We tried lower magnification first by using a focusing lens with $f = 100$ mm ($M = 5$). We used the guiding beam again which overlaps the OT beam but propagates downward so that small fraction of light enters the camera. We moved the position of the MOT to the guiding beam on the camera by changing the current of coils. We then changed the lens to $f = 400$ mm. In order to more finely adjust the focus position of the objective lens, we also tried imaging of atoms trapped in optical dipole trap (ODT) with a beam waist of 30 μm and the wavelength 1070 nm. The taken images are shown in Fig. 5.3.

5.3   Background light

To shield the camera from environmental light, we cover the imaging light path and mount two band-pass filters for 556 nm and one notch filter for 532 nm to the camera. We use different two band-pass filters: one is for 532 nm-556 nm (Semrock, FF01-544/24-25) and the other is for 554 nm-568 nm (Semrock, FF01-561/14-25). This combination enables narrow range of transmission 554 nm-556 nm. The majority of background light comes from OT beams. We confirmed this by comparing the background in the presence and the absence of them. We also confirmed that they include 556 nm wavelength, using notch filters for 532 nm and 556 nm. J. D. Thompson's group also observed the same fluorescence and they claims that it comes from the housing of the objective lens [47], which

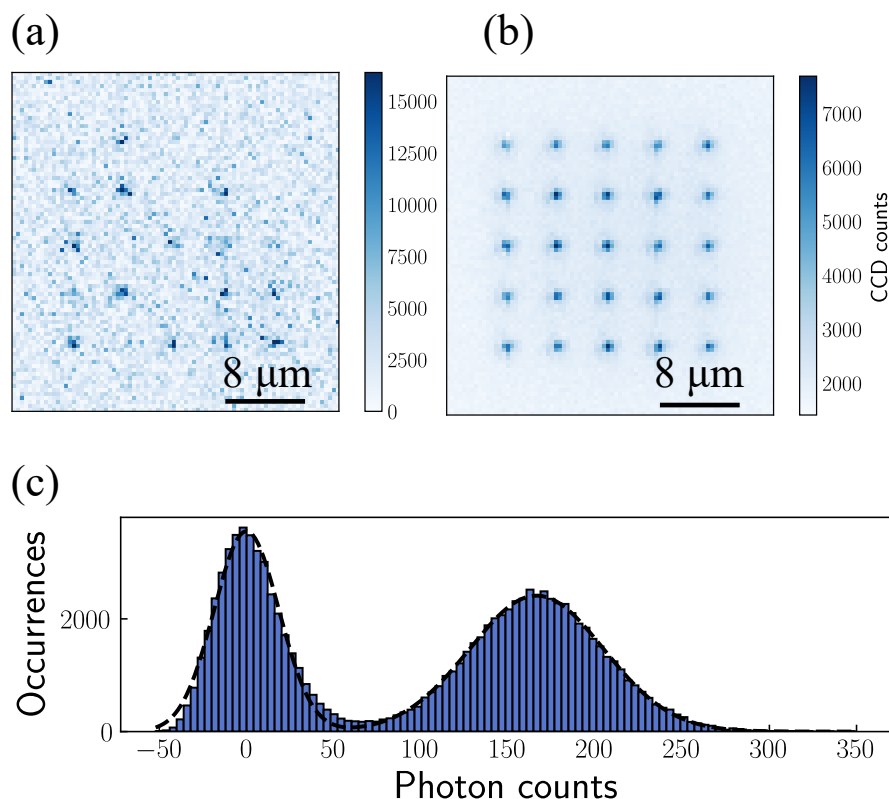is made of polyetherimide, so is ours. [1]

5.4 Single atom imaging

Figure 5.4: (a) Single-shot and (b) 400-average image of atoms in a 5×5 tweezer array with the spacing $4.8\,\mu$m (60 ms exposure time). (c) Histogram of photons detected by the CCD camera in each 3×3 pixel^2 region around the atom positions. The dashed line represents the fitted curve by a double gaussian distribution. The dark count is set to be zero for clarity.

We aligned the OT beam further and finally observed single atoms fluorescence. Atoms are loaded into a MOT from a Zeeman-slowed atomic beam for 500 ms. The atoms collected in the MOT are then compressed by increasing the magnetic field gradient and further cooled by decreasing the detuning and the power of the MOT beams. Typical temperature and the number of atoms at this stage are $\sim 20\,\mu$K and 10^5, respectively. Some of the atoms are trapped in the optical tweezers after turning off the MOT beams. We apply a red-detuned 556 nm light to induce losses of pairs of atoms by light-assisted collisions (Section 4.3.2). Single atoms are detected with fluorescence imaging with the $^1S_0 \leftrightarrow {}^3P_1$ transition. The imaging light is tilted by 16° from the horizontal plane

---

[1]We asked an engineer of Special Optics about this. They are not sure but they think it is possible that 556 nm fluorescence come from the housing. The glass material of the lens (Fused silica) and its coating are unlikely to cause such fluorescence from their experience.

and horizontally polarized. Photons emitted from the atoms are collected for 60 ms on a charge-coupled device camera through the objective lens (Fig. 5.1). 150 photons per single atom are typically detected. Single shot and 400-averaged images of a 5×5 tweezer array with a 4.8 μm spacing are shown in Fig. 5.4(a) and (b), respectively. We evaluated the NA of the imaging system by fitting the
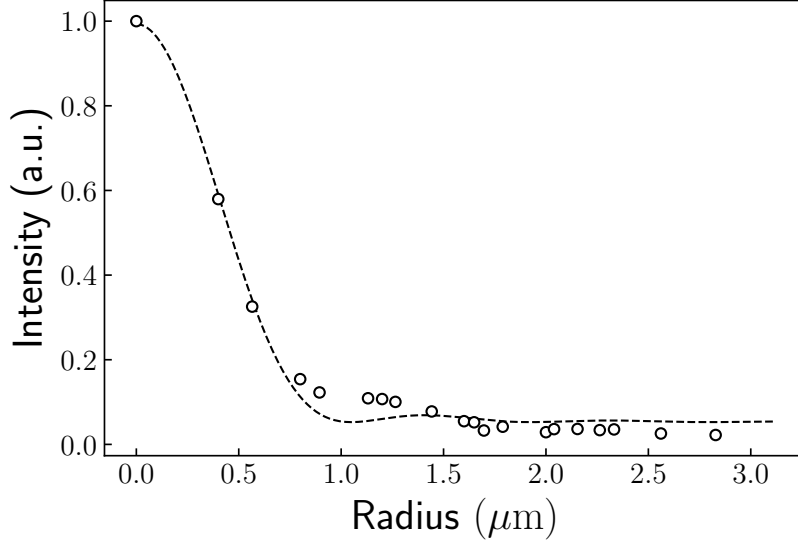

Figure 5.5:   The extracted PSF from the obtained images of atoms, fitted by the airy disk function. We evaluated the NA to be 0.31.

obtained image of the atoms to the airy disk function (Eq. (4.21)). The extracted PSF and the fitted curve are shown in Fig. 5.5. The resultant NA is 0.31, much less than the specification value. This implies imperfections of our imaging optical system.

A binarized behavior of the detected photon counts is clearly observed in the histogram as shown in Fig. 5.4(c). The photon count N_{ph} is converted from the CCD count N_{CCD} by a relation:

$$N_{\text{ph}} = N_{\text{CCD}} \times (\text{Q.E.}) \times (\text{Gain})/(\text{Sensitivity}). \tag{5.1}$$

(Q.E.) is a quantum efficiency of the sensor. The specification value of our camera for 556 nm wavelength is about 60%. We evaluated it actually using a testing system and deduced it to be 25%. This value is unexpectedly much worse than the specification. We attribute it to aging of the camera. Gain and sensitivity in our experiments are 1000 and 0.9, respectively. We determine the count threshold to distinguish between filled and empty sites by a double Gaussian fit:

$$\sum_{i=0,1} \frac{N_i}{\sqrt{2\pi}\sigma_i} \exp\left(-\frac{(x-\mu_i)^2}{2\sigma_i^2}\right) \tag{5.2}$$

$$\equiv \left(N_0 p_0(x) + N_1 p_1(x)\right), \tag{5.3}$$

where $i = 0$ or 1 indicates empty or filled sites, respectively. $p_{0(1)}(x)$ corresponds to the probability to detect x photons when the site is empty (filled). We distinguish whether the site is empty or

filled when we detect x photons by comparing $p_0(x)$ and $p_1(x)$: $p_0(x) > p_1(x) \rightarrow$ (empty) and $p_1(x) > p_0(x) \rightarrow$ (filled). In other words, we determine the threshold photon counts x_{th} as which satisfies $p_0(x_{th}) = p_1(x_{th})$ and regard a site as empty (filled) when $x < x_{th}$ ($x > x_{th}$). A false undetection and a false detection error probability is calculated as

$$\int_{x_{th}}^{\infty} p_0(x) \mathrm{d}x = 0.21\% \quad \text{(False undetection)},$$ (5.4)

$$\int_{-\infty}^{x_{th}} p_1(x) \mathrm{d}x = 0.13\% \quad \text{(False detection)}.$$ (5.5)

The loading probability is deduced from this double-Gaussian distribution as $N_1/(N_0 + N_1) =$ 58.4 %. We also take a second image and compared with the first one to evaluate the loss probability caused by the probe light. The obtained loss probability q over 400-shots is 5%.

5.5 Parametric loss spectroscopy
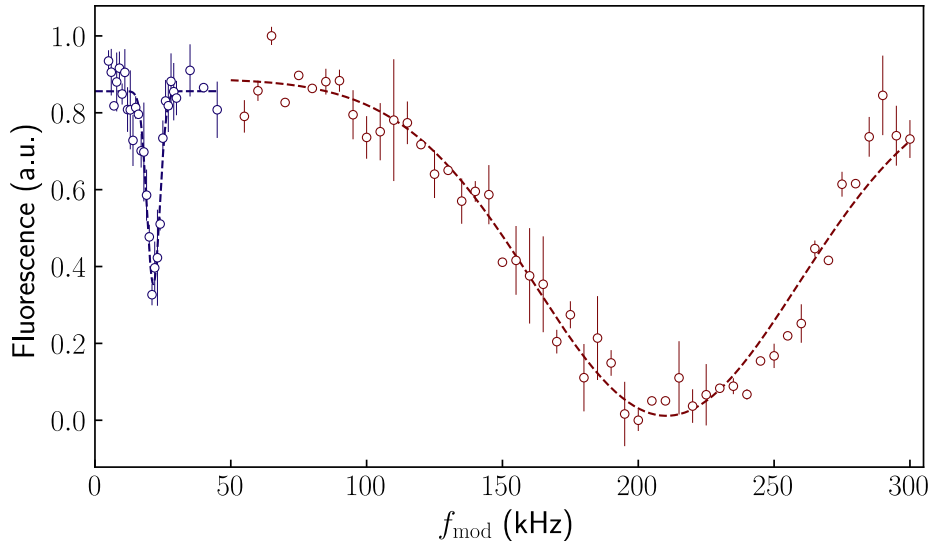
Figure 5.6: The obtained spectrum of loss by parametric heating is shown. The vertical axis shows the mean fluorescence from the atoms. The blue and red data are taken with different parameters: $V_{mod}/V_0 = 6\%, T_{mod} = 500\,\mathrm{ms}$ (blue) and $V_{mod}/V_0 = 3\%, T_{mod} = 50\,\mathrm{ms}$ (red), of which dips corresponds to axial and radial trapping frequency, respectively.

The trapping frequency of the atoms is measured by a parametric loss spectroscopy. We modulated the potential depth for a duration T_{mod} with a frequency f_{mod}:

$$V(t) = V_{DC} + V_{mod} \sin(2\pi f_{mod} t).$$ (5.6)

The heating by this modulation become maximum when f_{mod} is equal to twice the trapping frequency [113]. We deduced the axial and radial trapping frequency ν_z, ν_r from the obtained spectrum

(Fig. 5.6) as

$$\nu_r/(2\pi) = 102\,\text{kHz},\ \nu_z/(2\pi) = 10\,\text{kHz}. \tag{5.7}$$

We note $V_{\text{mod}}/V_{\text{DC}}$ and T_{mod} for $f_{\text{mod}} < 50\,\text{kHz}$ (blue) and $f_{\text{mod}} > 50\,\text{kHz}$ (red) is adjusted separately to observe dips by axial and radial trapping frequencies clearly. Using Eq. (4.14), the wait w_0 and the rayleigh length z_r of the OT beam is calculated as

$$w_0 = 1.0\,\mu\text{m},\ z_r = 5.9\,\mu\text{m}. \tag{5.8}$$

The obtained w_0 and z_r agrees the relation $z_r = \pi w_0^2/\lambda$ ($\lambda = 532\,\text{nm}$).

5.6   Cooling of atoms
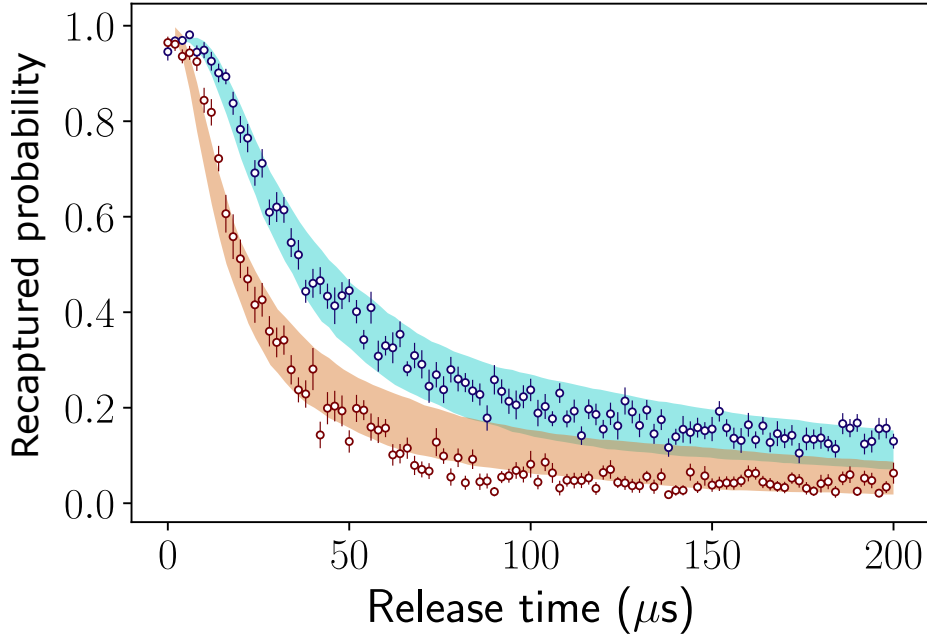
Figure 5.7: Recapture probability as a function of the release time t with (blue) and without (red) the cooling process. The error bars show the standard error of 16 repetitions. The shaded area indicates a 95% confidential interval from 100 trials of the Monte-Carlo simulation at the best fit temperature $T = 19.5\,\mu\text{K}$ (blue) and $T = 59.1\,\mu\text{K}$ (red).

Atoms heated by the probe light are cooled after the first image using the $^1S_0 \leftrightarrow {}^3P_1$ MOT lights in three directions for 10 ms, which is red-detuned by 1.9 times the natural linewidth. The cooling effect is verified by the release-and-recapture technique [114]. We first take an image of an atom array followed by the cooling. We then turn off the trap for a release time t and take the second image. We repeat this procedure 16 times for each t and obtain the probability of recapturing atoms as a function of t with and without the cooling as shown in Fig. 5.7. We fit the experimental data to

a Monte-Carlo simulated trajectories by the weighted least-square method 100 times and we deduce the temperature to be $19.5 \pm 2.1 \, \mu K$ for the data with the cooling and $59.1 \pm 5.4 \, \mu K$ for without the cooling, from the mean and the standard deviation of the fit results. The temperature with the cooling is close to that in the MOT. We note that the obtained temperature corresponds to that in the radial direction since the radial expansion is critical for the atoms to remain in the highly anisotropic recapture region.

5.7 Rearrangement of atoms

To obtain defect-free atom arrays, we demonstrate a rearrangement protocol in 1D and 2D arrays. We first prepare a sample randomly loaded in a 1D array of 25 sites and take an image. At this stage, we identify the filled and empty sites. We then turn off the RF components applied to the AODs corresponding to the empty trap sites, and move the remaining sites to the left by dynamically changing the multi-tone RF in 0.64 ms. To confirm the successful rearrangement, we finally take the second image. Figure 5.8(a) shows typical images before and after the rearrangement.

Figure 5.8(b) shows the probability to find an atom in each site obtained by 200 experimental runs before (blue circles) and after (red squares) the rearrangement. The probability to find an atom in the i-th site from the left edge after the rearrangement is given by

$$P_i = (1 - q) \times \sum_{\substack{j \\ i \le j \le N}} \binom{N}{j} p^j \, (1 - p)^{N-j}. \tag{5.9}$$

Here N is the number of total trap sites before the rearrangement, p is the loading probability, and q is the loss probability between the two images. The fit of Eq. (5.9) gives $p = 0.61$ and $q = 0.07$. The obtained value of p and $1 - q$ are close to the fully random case of $1/2$, and the survival probability of 0.95, which indicates the rearrangement process is performed with negligibly small error.

This rearrangement method using AODs is not limited to 1D arrays. Figure 5.8(c) shows an example for a 2D array. By only collecting defectless vertical lines of sites in a 3×8 array, we successfully prepare a defect-free 3×5 array of single atoms. As far as we know, this is the first demonstration of creating a defect-free 2D array only by AODs.

5.8 Conclusion

We succeeded in trapping of single atoms with a loading probability roughly 60% and detection with 0.3% error for 5×5 OT array. The loss caused by this imaging is about 5%. We cooled heated atoms by the imaging process and confirmed the cooling effect using a release-and-recapture technique. The cooling during the imaging are supposed to decrease the loss from the trap, though we were not able to do that due to our optical setups of MOT beams and imaging paths. We also performed the rearrangement of randomly loaded atom array to a defect-free array by a fast feedback program, for 25 sites 1D array and 3×8 sites 2D array. The result implies negligible losses during the
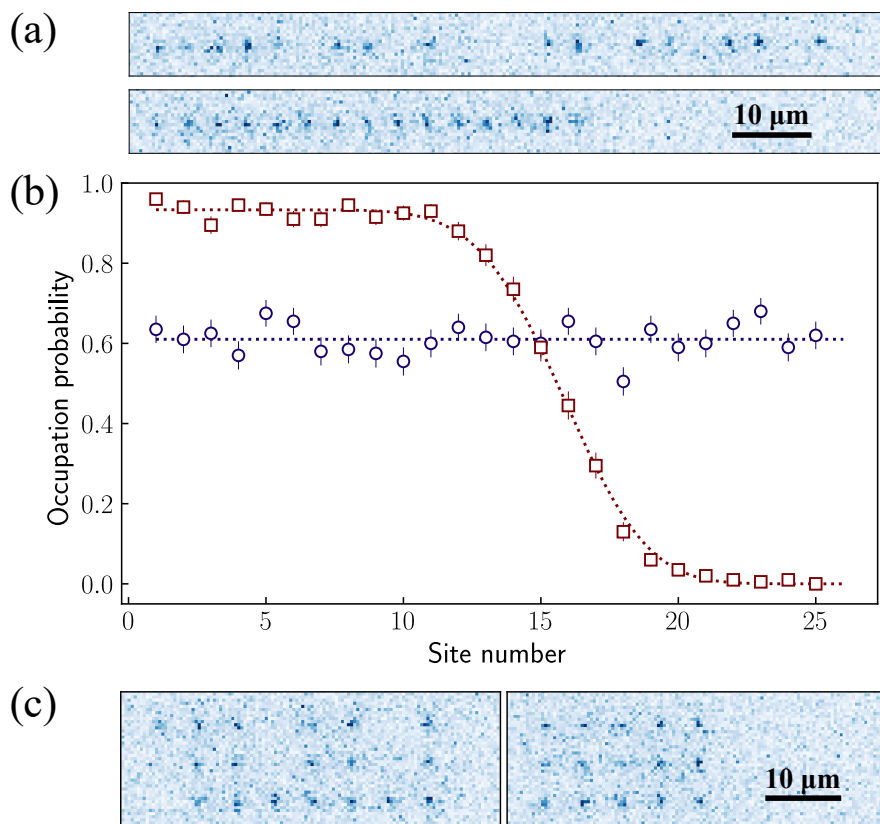
(a)

10 μm

(b)

(c)

10 μm

Figure 5.8: (a) Fluorescence images before (upper) and after (lower) the rearrangement of atoms for one-dimensional 25 tweezer array. (b) The occupation probability of each site before (blue circles) and after (red squares) the rearrangement averaged for 200-shots. (c) Fluorescence images before (left) and after (right) the rearrangement of the atoms for a two-dimensional 3×8 tweezer array. Only defectless columns are left and shifted to form a defect-free array.

rearrangement. These achievements are important foundations toward the large-scale atom array for the quantum computing.

For the future experiments, we are to use $^1S_0 \leftrightarrow {}^1P_1$ transition instead of $^1S_0 \leftrightarrow {}^3P_1$ transition. Though $^1S_0 \leftrightarrow {}^3P_1$ transition is convenient since it allows us to perform both trapping and imaging with only one objective lens, it's narrow linewidth requires fine tuning of polarization and magnetic field to reduce the potential shift between the ground and the excited state to ensure the high-performance of the imaging, which is expected to be difficult for fermionic isotopes with 532 nm wavelength [42]. On the other hand, broad-linewidth $^1S_0 \leftrightarrow {}^1P_1$ is insensitive to such energy differences. This also allows us to perform the cooling for three axis simultaneously during the imaging. In addition, we expect less background noises thanks to large difference of wavelengths between trapping and imaging light and fast cycle of transitions, resulting in short exposure time. We already installed another objective lens for UV light above the science chamber and succeeded in getting images of single atoms in an OT array at the time of writing this thesis.

High-resolution spectroscopy and single-photon Rydberg excitation

6.1 High-resolution $^1\mathrm{S}_0 \leftrightarrow {}^3\mathrm{P}_2$ spectroscopy

6.1.1 Spectroscopy for atomic clouds
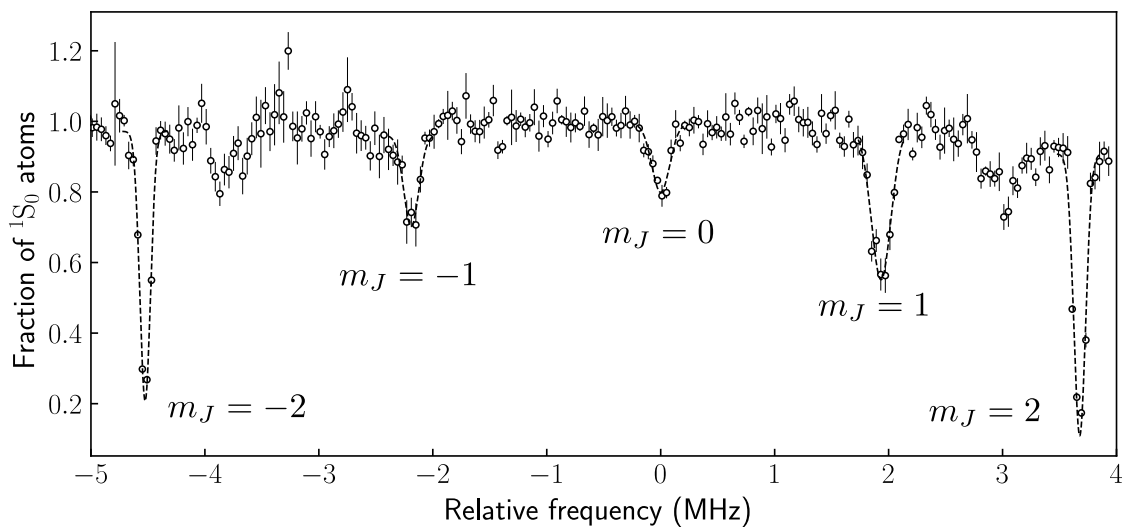
Figure 6.1: The obtained spectrum between $^1\mathrm{S}_0 \leftrightarrow {}^3\mathrm{P}_2$. The loss of $^1\mathrm{S}_0$ atoms corresponds to the excitation to the $^3\mathrm{P}_2$ state.

We first tried to find the resonance of $^1\mathrm{S}_0 \leftrightarrow {}^3\mathrm{P}_2$ transition using atomic clouds in an optical dipole trap (ODT) formed with a wavelength of 1070 nm. Atoms loaded in a MOT for 10 s are transferred into the ODT and evaporatively cooled. Finally we obtain 10^5 atoms with a temperatrue of 5 μK. We irradiated 507 nm laser to atom for 500 ms. The excitation to $^3\mathrm{P}_2$ is detected as a loss of the number of $^1\mathrm{S}_0$ atoms. To remove the long-term fluctuation of the number of atoms, we take two successive

absorption images with and without the irradiation, and we measured the ratio of the number of atoms between them. Figure 6.1 shows the obtained spectrum, indicating clear five splittings by Zeeman energy shifts. We unexpectedly observe small peaks in between $|m_J| = 2$ and $|m_J| = 1$ resonances, which we attribute to the laser frequency noise.

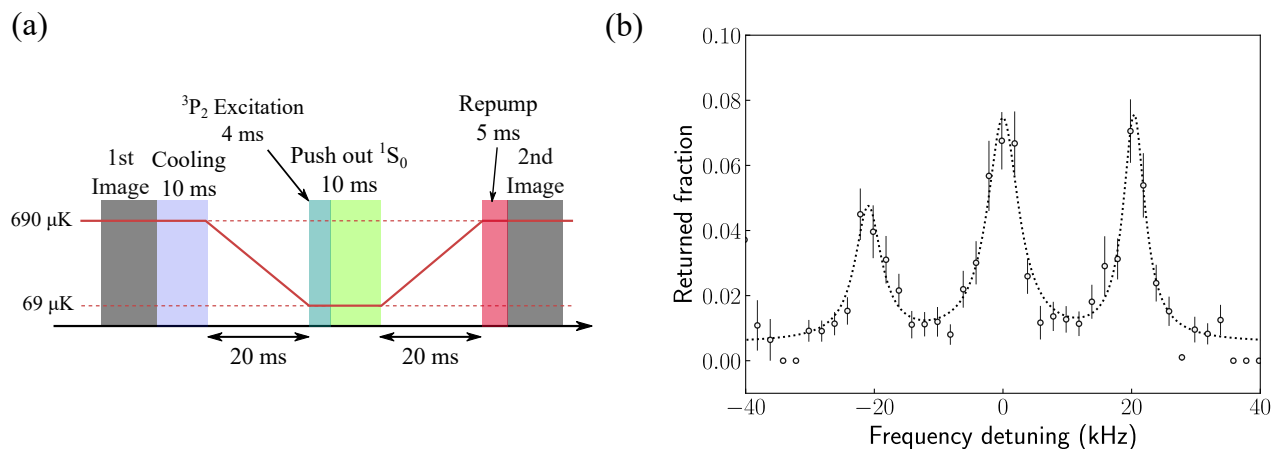### 6.1.2 Sideband-resolved spectroscopy for single atoms

(a) (b)

Figure 6.2: (a) Pulse sequence for $^3P_2$ state spectroscopy. (b) A $^3P_2$ ($m_J = 0$) spectrum for single atoms in the 5×5 tweezer array. The dotted line is a fit by three Lorentzian functions. The peak height ratio of the red to the blue sidebands yields the temperature $1.90 \pm 1.02\,\mu$K and the mean vibrational number occupation $n = 1.46 \pm 1.01$.

We perform spectroscopy of the $m_J = 0$ state of single atoms in a 5×5 array. The experimental sequence proceeds as shown in Fig. 6.2(a). We first take an image of single atoms randomly loaded in a 5×5 array followed by the cooling as described in section 4.4.2. The potential depth at this stage is $690\,\mu$K. The tweezer potential is adiabatically ramped down to $1/10$ to further reduce inhomogeneous broadening of the $^1S_0 \leftrightarrow {}^3P_2$ resonance. We apply a 507 nm laser pulse for 4 ms followed by a 556 nm laser pulse for 10 ms to remove the remaining atoms in the ground state from the array. After the 507 nm excitation, we ramp the tweezer potential back to the initial value and apply a 770 nm light for 5 ms. We note that the $^3S_1$ state spontaneously decays into all the ^3P_J ($J = 0, 1, 2$) with the branching ratio a_J, where $a_0 = 13\%, a_1 = 37\%, a_2 = 50\%$ (Section 3.1.2.4). $^3P_2$ atoms return to the $^1S_0$ state through the $^3S_1$ state, with the probability calculated as

$$a_1 + a_2 \times a_1 + a_2^2 \times a_1 \cdots = a_1 \sum_{n=0}^{\infty} a_2^n = \frac{a_1}{1 - a_2} = 73.5\%. \tag{6.1}$$

Nearly $3/4$ of $^3P_2$ atoms, therefore, return to the $^1S_0$ state without the other repumper of $^3P_0$ atoms. Finally, we take the second fluorescence image and obtain the return fraction by comparing with the first image.

Figure 6.2(b) shows a typical spectrum. The carrier resonance and the blue and red sidebands are well resolved, promising for the sideband cooling to the vibrational ground state in the optical

tweezers. The radial trap frequency $\nu_r/(2\pi)$ deduced from the sidebands is 20.7 ± 0.3 kHz, from which we evaluate the waist of the tweezer beams to be $0.89\,\mu$m. The ratio of the peak heights of the red sideband A_R to the blue A_B gives the temperature T and the mean vibrational number occupation $\bar{n}$ by a relation $A_R/A_B = \exp\left(-\hbar\nu_r/(k_B T)\right) = \bar{n}/(1 + \bar{n})$, and we find $T = 1.90 \pm 1.02\,\mu$K and $\bar{n} = 1.46 \pm 1.01$. The obtained value of $\bar{n}$ is in agreement with the theoretical expectation that $\bar{n}$ is reduced to 1.05 at most by the cooling process taking into account the sideband transitions, using Eq. (2.92). The assumption of the same distribution of the occupation for trap depth before the ramping down of the potential suggests the temperature of $6.01 \pm 3.24\,\mu$K. We attribute the difference between the value obtained with the release-and-recapture method in the previous section to the assumption of isotropic temperatures in the Monte-Carlo simulation. Note that the saturation effect would contribute to reduction of the peak height of the carrier resonance.

6.2 Rydberg excitation

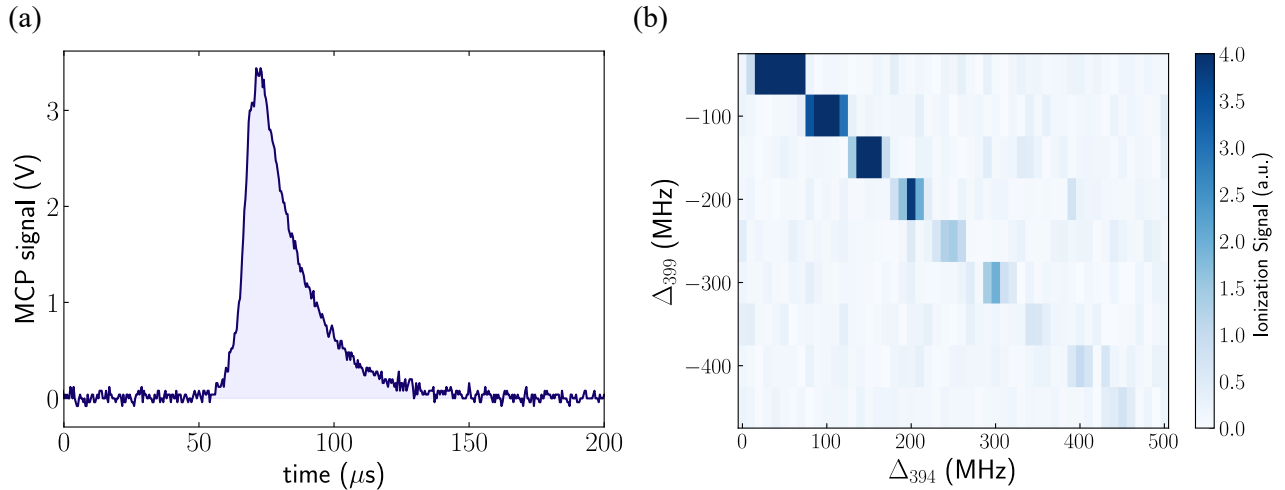### 6.2.1 Two-photon Rydberg excitation via $^1P_1$ state

Figure 6.3: (a) Typical signal detected by the MCP. The shaded area corresponds to the number of ions detected. (b) Obtained two-dimensional spectrum of two-photon excitation to $(6s)(78d)^1D_2$ as $^1P_1$ an intermediate state. Relative frequencies of 399 nm (Δ_{399}) and 394 nm (Δ_{394}) laser are scanned.

As a preliminary experiment, we first tried two-photon Rydberg excitation using $^1P_1$ as an intermediate state and ionization detection of them. We irradiate 399 nm and 394 nm lasers simultaneously for 1 ms to atoms in MOT, and then apply an electric field. Figure 6.3(a) shows a typical averaged MCP signal. We chose $(6s)(78d)\,^1D_2$ as a target state, of which resonance is reported by a laser and microwave spectroscopy [94]. We scanned both laser frequencies Δ_{399} and Δ_{394}, and observed a resonance where the total energy of two photons coincides the energy gap between the ground and the Rydberg state: $\Delta_{399} + \Delta_{394} = $ const. (Fig. 6.3(b)). $\Delta_{399} = 0$ corresponds to the resonance of the $^1S_0 \leftrightarrow ^1P_1$ transition. We confirmed our MCP and electrodes work fine by this

experiments.

6.2.2 Rydberg spectroscopy from the $^3P_2$ state for atomic clouds
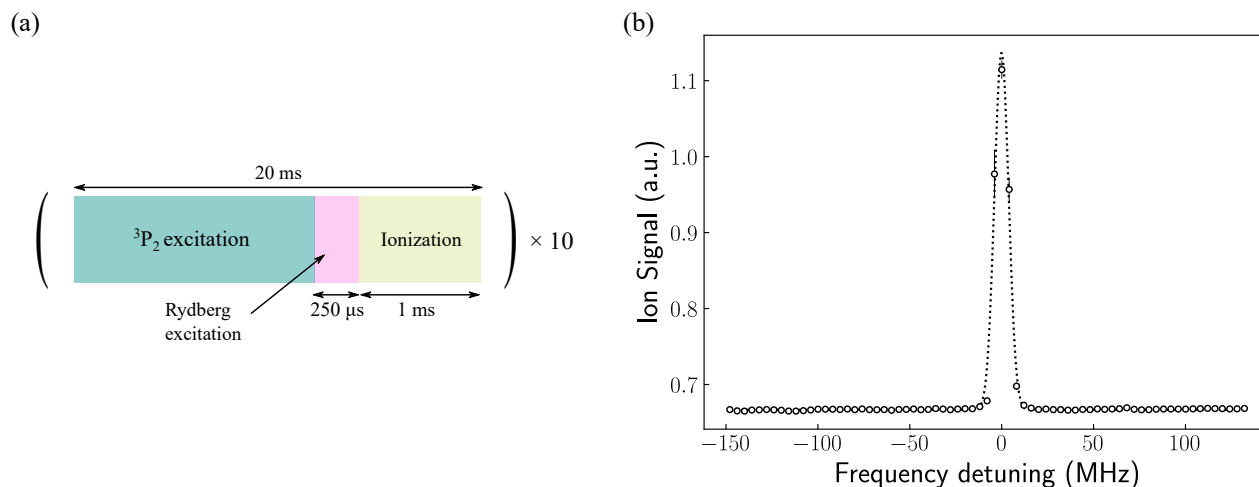
6.2.2.1 $^3S_1$ series

Figure 6.4: (a) Pulse sequence for the Rydberg state ionization spectroscopy. (b) A spectral data between the $^3P_2$ ($m_J = 2$) and (6s)(80s)$^3S_1$ state. The dashed line shows the fitted curve by a Gaussian function.

We then tried to observe a spectrum of single-photon excitation to Rydberg $^3S_1$ states from the $^3P_2$ state. We first apply a 507 nm pulse resonant to the $^1S_0 \leftrightarrow {}^3P_2$ ($m_J = 2$) transition for 18.75 ms followed by a 325 nm pulse for 250 μs. Immediately after the 325 nm pulse we ramp up the electric field to 17 V/cm to detect the Rydberg states on the MCP by the field ionization method. This excitation and ionization process is repeated for 10 times and the MCP signals are averaged. Figure 6.4(a) and (b) show the pulse sequence and a spectrum for (6s)(80s)$^3S_1$, respectively. The dashed line shows a fitted curve by a Gaussian function. We note a Lorentzian function does note fit the data well. The full-width half maximum (FWHM) of the resonance is 6.0 MHz, comparable to the uncertainty of the wavemeter: 10 MHz. The frequency of the 325 nm photon at the resonance is 1 511 669 013 MHz, corresponds to 50 423.850 67 cm^{-1} using the measured transition frequency between the $^1S_0$ and the $^3P_2$ $m_J = 0$ state: 590 902 342 562 $\pm$ 3 $\pm$ 60kHz [52]. This value well agrees with the reported value of the resonant frequency using a two-photon excitation via the $^3P_1$ state: 50 423.8507 cm^{-1} = 1 511 669 014 MHz.

We also observed a response of the resonant energy to an electric field. A weak electric field is applied during the excitation along the x-direction in Fig 4.3. Quadratic DC stark shifts and a splitting to two peaks corresponds to $|m_J| = 0, 1$ are observed and shown in Fig. 6.5. We deduce the
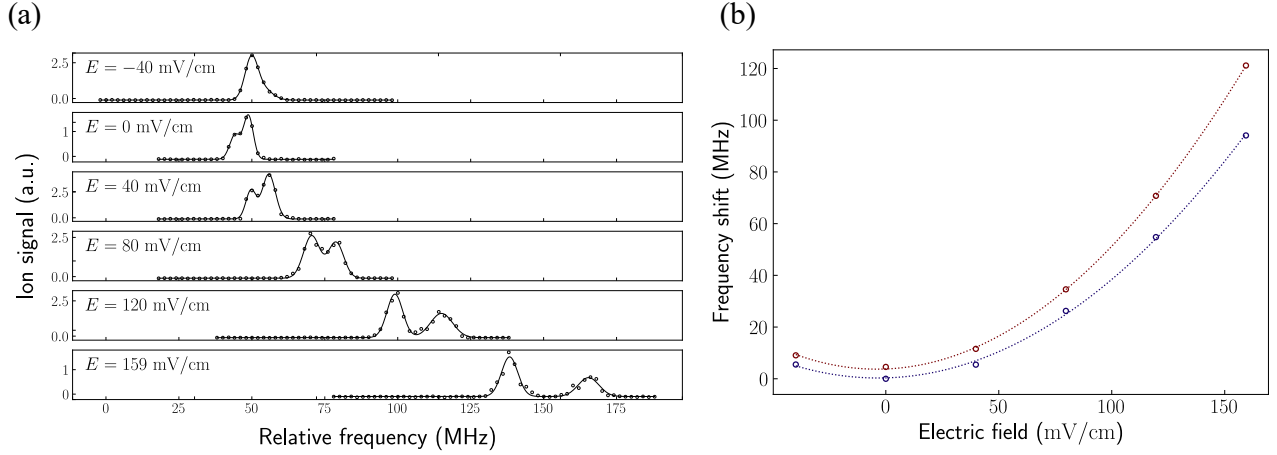
(a)

(b)

Figure 6.5: (a)Obtained spectra with a weak electric field applied during the excitation. (b)DC stark shifts by an electric field and fitted curves are shown for each splittings corresponding to $|m_J| = 0, 1$.

polarizability for $|m_J| = 0$ and 1 as

$$\alpha_0/h = -7.12\,\text{kHz/(mV/cm)}^2, \tag{6.2}$$

$$\alpha_1/h = -8.80\,\text{kHz/(mV/cm)}^2, \tag{6.3}$$

from the obtained data (Eq. (3.21)).

6.2.2.2 ^{3}D series

D-series Rydberg states also have dipole-allowed transitions from the $^3P_2$ state: $^3D_1$ and $^3D_3$. The value of energy of the $^3D_1$ and the $^3D_2$ states are reported using two-photon laser and microwave spectroscopy, as well as $^1D_2$ states [94]. We scanned the frequency of 325 nm laser around the resonance of $^3D_1$ and the $^3D_2$ states and observed complex spectra ranging from $n = 65$ to 80. The pulse sequence is the same as that for $^3S_1$. Note we used $^3P_2$ $m_J = 2$ in this case.

We observe up to eight resonances in the range of ∼ 1 GHz as shown in Fig. 6.6. The resonances indexed as 2 and 7 are newly observed in this work, while the rest have been observed in the previous works and 3, 5 and 8 were assigned to be $^3D_1$, $^3D_2$ and $^1D_2$ states, respectively [94]. The peaks of 1, 4, and 6 were also observed in [115], but not assigned. We consider the strongest resonance 7 to be the $^3D_3$ state because of the selection rule of the dipole transition. This assignment is supported by the fact that the resonance splits into four corresponding to $|m_J| = 0, 1, 2, 3$ manifolds by applying electric fields along the x-direction due to the electric-field-induced quadruple splitting (Fig. 6.8. Assignment and references which observed the resonances are summarized in Table 6.1.

We deduce the quantum defect of each resonance and plot them against the principal quantum number in Fig. 6.7. Here the quantum defect δ is defined similarly as Eq. (3.52) by the following relation

$$E = I - \frac{R_{\text{Yb}}}{(n - \delta)^2}, \tag{6.4}$$
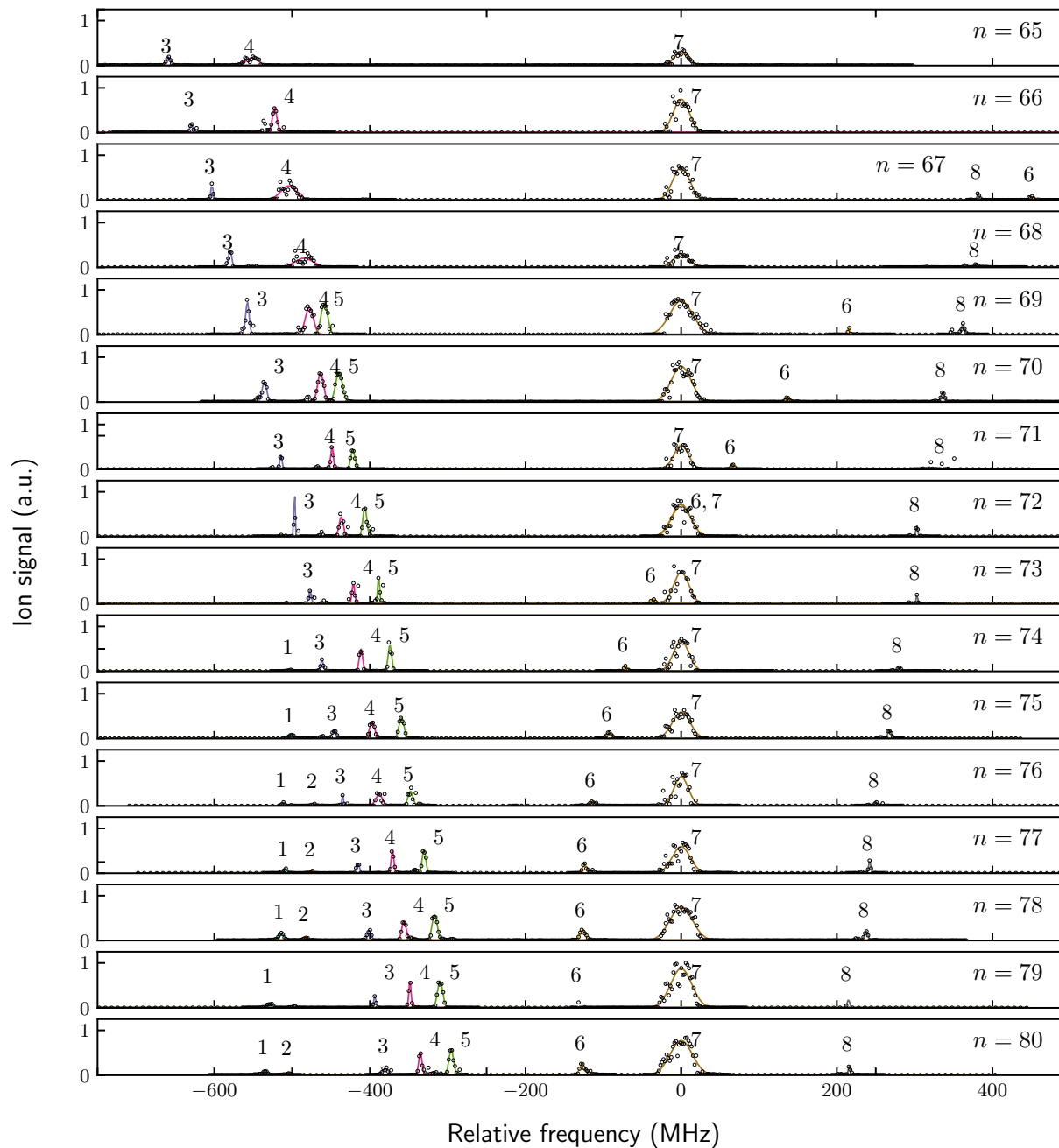
Figure 6.6: Spectra around the $^3P_2$ ($m_J = 2$) $\leftrightarrow$ ^3D transition for $n = 65$–80. We label the resonances by numbers from lower to higher energies in the $n = 80$ spectrum. The horizontal axis is relative freuqency from the strongest resonance 7. The resonances 3, 5 and 8 correspond to $^3D_1$, $^3D_2$ and $^1D_2$ states, respectively. The peaks 2 and 7 are the new observations, and 7 is assigned as $(6s)(nd)^3D_3$. Note that the peaks of 1, 4, and 6 were also observed in [115] but not assigned.

Table 6.1: Assignment of resonances and references which reports the corresponding resonance is summarized.

	1	2	3	4	5	6	7	8
Assigned state	^3P?	^3P?	$^3D_1$	$^3D_2$?	$^3D_2$	^3P?	$^3D_3$	$^1D_2$
Ref.	[115]		[64]	[94]	[94]	[115]		[94]
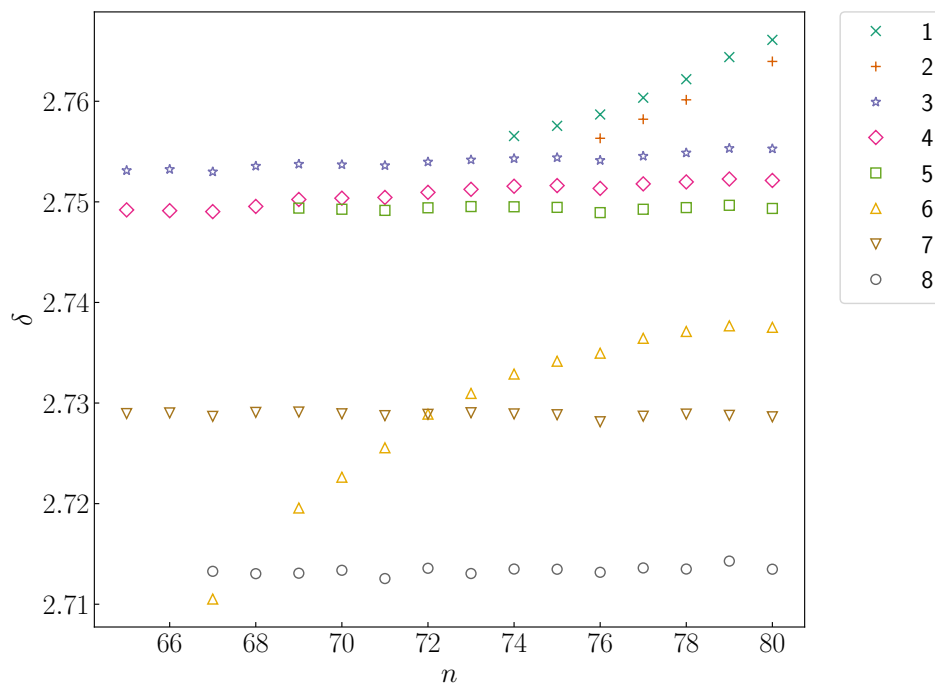
Figure 6.7: The quantum defect δ of the resonances against the principal quantum number.

where $I = 50\,443.070\,41\,\mathrm{cm}^{-1}$ and $R_{\mathrm{Yb}} = 10\,973.696\,959\,\mathrm{cm}^{-1}$ are the energy of the first ionization limit and the Rydberg constant of ^{174}Yb, respectively [94]. The quantum defects for the low-lying $^3D_3$ state of $n = 10$ and 12–15 were deduced in [116]. We confirm that the deduced quantum defects for the high-lying $^3D_3$ Rydberg states are in good agreement with the values for the low-lying ones. Table 6.2 summarizes the energies and the quantum defects obtained by our measurement.

Table 6.2: Energy and quantum defect values of the observed resonances for n = 65–80. Index numbers indicate the number assigned to each peak in Fig.6.6. Typical uncertainty of the resonance frequency is about 10 MHz coming from the uncertainty of the wavemeter.

| n	index	δ	E/h (MHz)	n	index	δ	E/h (MHz)
65	3	2.753 118 00	1 511 396 147	74	6	2.732 881 65	1 511 597 475
	4	2.749 201 30	1 511 396 253		7	2.728 919 37	1 511 597 547
	7	2.728 954 75	1 511 396 805		8	2.713 498 12	1 511 597 827
66	3	2.753 233 55	1 511 422 780	75	1	2.757 558 00	1 511 614 846
	4	2.749 123 37	1 511 422 887		3	2.754 396 71	1 511 614 902
	7	2.729 019 84	1 511 423 410		4	2.751 617 38	1 511 614 950
67	3	2.752 989 91	1 511 448 189		5	2.749 453 21	1 511 614 988
	4	2.749 030 83	1 511 448 288		6	2.734 156 93	1 511 615 255
	6	2.710 514 77	1 511 449 242		7	2.728 839 26	1 511 615 347
	7	2.728 676 00	1 511 448 792		8	2.713 478 24	1 511 615 615
	8	2.713 271 53	1 511 449 174	76	1	2.758 686 17	1 511 631 923
68	3	2.753 556 14	1 511 472 419		2	2.756 319 39	1 511 631 963
	4	2.749 545 81	1 511 472 514		3	2.754 128 63	1 511 631 999
	7	2.729 072 10	1 511 472 999		4	2.751 338 22	1 511 632 046
	8	2.713 037 07	1 511 473 378		5	2.748 931 06	1 511 632 086
69	3	2.753 751 90	1 511 495 570		6	2.734 955 80	1 511 632 320
	4	2.750 236 53	1 511 495 649		7	2.728 140 55	1 511 632 434
	5	2.749 379 75	1 511 495 669		8	2.713 174 28	1 511 632 685
	6	2.719 565 11	1 511 496 343	77	1	2.760 353 76	1 511 648 306
	7	2.729 107 78	1 511 496 127		2	2.758 213 71	1 511 648 341
	8	2.713 083 52	1 511 496 489		3	2.754 547 05	1 511 648 400
70	3	2.753 698 45	1 511 517 700		4	2.751 787 62	1 511 648 444
	4	2.750 364 04	1 511 517 772		5	2.749 265 15	1 511 648 485
	5	2.749 266 63	1 511 517 796		6	2.736 433 65	1 511 648 691
	6	2.722 625 17	1 511 518 372		7	2.728 692 66	1 511 648 815
	7	2.728 931 74	1 511 518 236		8	2.713 606 30	1 511 649 057
	8	2.713 374 54	1 511 518 572	78	1	2.762 192 34	1 511 664 039
71	3	2.753 606 97	1 511 538 866		2	2.760 144 54	1 511 664 071
	4	2.750 438 77	1 511 538 932		3	2.754 872 56	1 511 664 152
	5	2.749 153 25	1 511 538 958		4	2.751 981 88	1 511 664 197
	6	2.725 552 12	1 511 539 446		5	2.749 430 08	1 511 664 236
	7	2.728 750 50	1 511 539 380		6	2.737 113 54	1 511 664 426
	8	2.712 551 98	1 511 539 715		7	2.728 904 26	1 511 664 553
72	3	2.753 973 35	1 511 559 112		8	2.713 498 64	1 511 664 791
	4	2.750 944 03	1 511 559 172	79	1	2.764 389 69	1 511 679 153
	5	2.749 409 48	1 511 559 203		3	2.755 316 70	1 511 679 287
	6	2.728 897 38	1 511 559 609		4	2.752 270 80	1 511 679 333
	7	2.728 880 20	1 511 559 609		5	2.749 658 77	1 511 679 371
	8	2.713 575 35	1 511 559 912		6	2.737 673 32	1 511 679 549
73	3	2.754 176 31	1 511 578 503		7	2.728 778 71	1 511 679 681
	4	2.751 246 56	1 511 578 559		8	2.714 288 47	1 511 679 896
	5	2.749 532 47	1 511 578 592	80	1	2.766 103 81	1 511 693 691
	6	2.730 954 96	1 511 578 944		2	2.763 960 40	1 511 693 722
	7	2.729 037 71	1 511 578 980		3	2.755 277 19	1 511 693 846
	8	2.713 052 18	1 511 579 283		4	2.752 128 81	1 511 693 891
74	1	2.756 543 85	1 511 597 045		5	2.749 345 23	1 511 693 930
	3	2.754 300 03	1 511 597 085		6	2.737 524 41	1 511 694 099
	4	2.751 552 23	1 511 597 135		7	2.728 632 77	1 511 694 226
	5	2.749 510 64	1 511 597 172		8	2.713 481 34	1 511 694 442
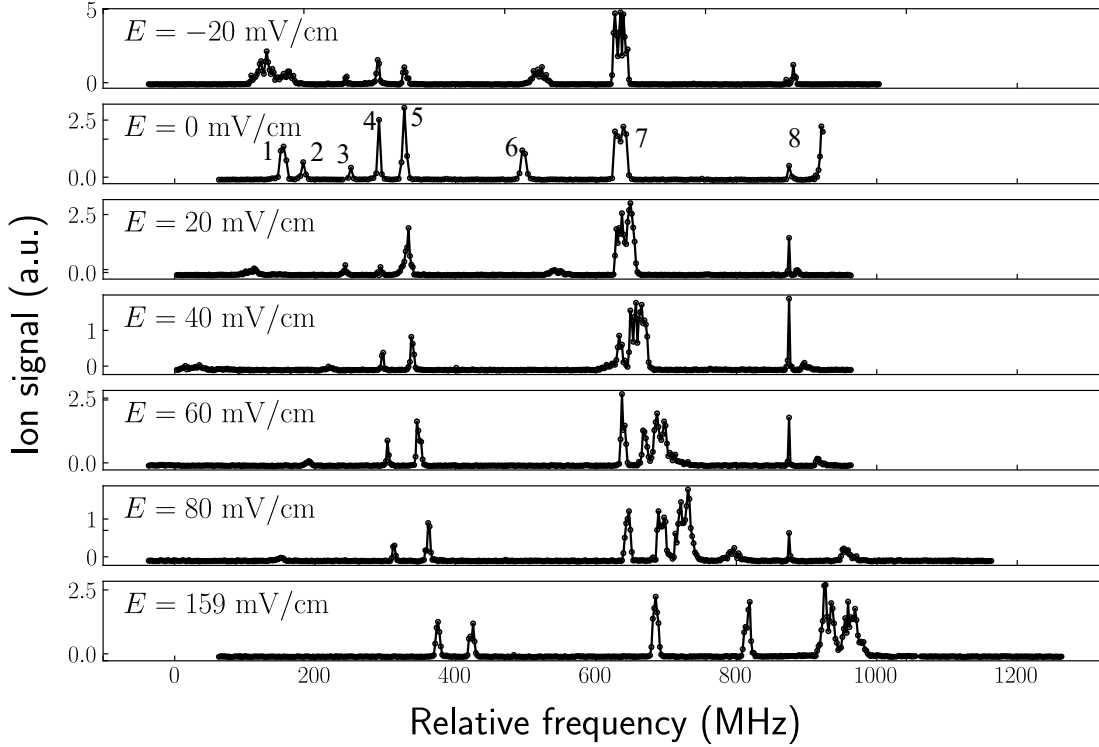
Figure 6.8: DC-stark shift by an applied electric field for (6s)(78d) Rydberg states are observed.

6.2.3   Single-photon Rydberg excitation of single atoms

We perform single-photon Rydberg state excitation spectroscopy from the $^3P_2$ state in single atom arrays. The $^3P_2$ state atoms are prepared by applying a 507 nm laser pulse for 20 ms on the carrier resonance in the shallow trap, yielding the excitation probability of 40%. After ramping back the trap potential we apply a 325 nm laser pulse for 10 ms followed by ionization. We then take the second image after a 5 ms pulse of the 770 nm laser (see Fig. 6.9(a)). Successful excitation to a Rydberg state is observed as a decrease of the return probability as shown in Fig. 6.9(b). The observed resonance corresponds to the (6s)(78d) $^3D_3$ state. This is the first demonstration of the single-photon Rydberg excitation of a single Yb atom array.

6.3   Conclusion

We succeeded in observing a sideband-resolved spectrum for single atoms in an OT array, which enables us to perform a sideband-cooling to the motional ground state with the aid of repumpers [117, 118]: $^3P_2 \rightarrow ^3S_1$ (λ = 770 nm and $^3P_0 \rightarrow ^3S_1$ (λ = 649 nm). The mean occupation quantum number for the motional eigenstate along the radial direction is deduced from the spectrum as 1.46 ± 1.01, which agrees with a calculation of the cooling process.

We also performed a spectroscopy of single-photon excitation to Rydberg states from the $^3P_2$
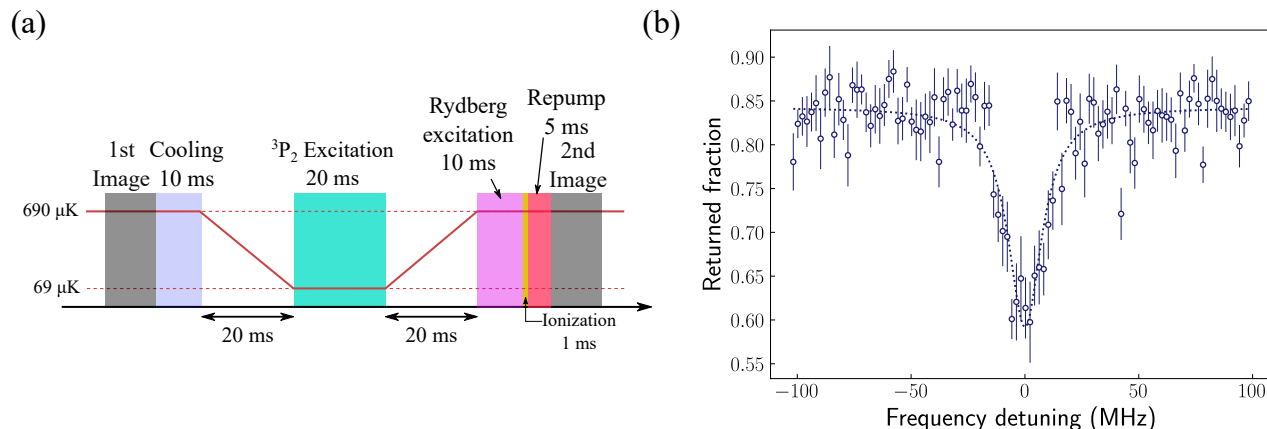
(a)

(b)

Figure 6.9: (a) Pulse sequence for the Rydberg spectroscopy from the $^3P_2$ state for single atoms. (b) A spectrum of the $^3P_2$, $m_J = 0 \leftrightarrow$ (6s)(78d)$^3D_3$ transition for single atoms in the 5×5 tweezer array. Rydberg states are ionized by an electric field before the repumping of $^3P_2$ state and observed as a loss of the $^1S_0$ state.

state, as well as a two-photon spectroscopy with $^1P_1$ as an intermediate state, using atomic clouds in ODT or MOT. We observed resonances of ^3D and $^3S_1$ Rydberg series. Especially, $^3D_3$ states is newly observed in our work thanks to our choice of the $J = 2$ state as the initial state. It is notable that the energy of $^3D_3$ and the 8th peak cross at $n = 72$, from which we expect strong interactions between $^3D_3$ Rydberg state atoms by the Förster resonance. The exploitable states to generate the strong dipole–dipole interactions are not known for Yb atoms and this opens up new possibilities for quantum computing and simulations.

<div style="text-align: right;">CHAPTER 7</div>

Schemes for nondestructive detection of single atoms

7.1 Principle of homodyne Faraday detection

Before going to our proposal schemes for nondestructive imaging, we discuss the limitation of quantum gas microscopy with a dispersive Faraday interaction. Figure 7.1(a) shows the schematic setup [119]. We assume the transition $J_g = 0 \rightarrow J_e = 1$ with a wavelength λ for probing the atoms for simplicity, as shown in Fig. 7.1(b). When we set the frequency of the probe beam at the center of the $J_g = 0 \rightarrow J_e = 1, m_e = \pm 1$ transitions in the presence of a bias magnetic field B_0 applied along the probe propagation axis, the σ_+ and σ_- circular polarization components of the linearly polarized probe beam have different detunings $\pm \delta_B$ provided by the magnetic field. This causes different phase shifts in the two components and therefore induces the rotation of the axis of linear polarization of the probe beam, termed the Faraday effect. The polarization rotation signal for a single atom can be understood as an effect of interference between a linearly polarized input probe beam $\boldsymbol{E}_{\text{probe}}(r)$ and an elastically scattered electric field coherently induced by a single atom. Based on diffraction theory [111] and scattering theory [120], the scattered light field $\boldsymbol{E}_{\text{sc}}(r)$ is described [119] as

$$\boldsymbol{E}_{\text{sc}}(r) = \alpha \frac{2J_1(r/\sigma)}{r/\sigma} E_0 \left(\frac{\hat{\boldsymbol{e}}_+}{1 - i(2\delta_B/\Gamma)} + \frac{\hat{\boldsymbol{e}}_-}{1 + i(2\delta_B/\Gamma)} \right), \tag{7.1}$$

where Γ is the natural linewidth of the excited state. E_0 is the amplitude of the electric field of the input probe beam, $\alpha = -\sqrt{3\eta} A_N/2$, where $\eta \equiv [1 - (1 - A_N{}^2)^{1/2}(1 - A_N{}^2/4)]/2$ is the photon collection efficiency of an objective lens, A_N is the NA of the lens, $J_1(x)$ is the Bessel function of the first kind, $\sigma \equiv (kA_N)^{-1}$ is the diffraction-limited spatial resolution, k is the wavenumber of the probe light, and $\hat{\boldsymbol{e}}_\pm = (\hat{\boldsymbol{e}}_x \pm i\hat{\boldsymbol{e}}_y)$ is the polarization unit vector for $\sigma_\pm$ circularly polarized light. For large δ_B/Γ, the scattered light polarization is perpendicular to the initial polarization of the probe light and has the expected $1/\delta_B$ dependence.

After passing through the HWP and the PBS, only the component parallel to an appropriate linear unit vector $\hat{\boldsymbol{e}}_\theta = \cos\theta \hat{\boldsymbol{e}}_x + \sin\theta \hat{\boldsymbol{e}}_y$[1] arrives the CCD. The resulting intensity of the light at the

---

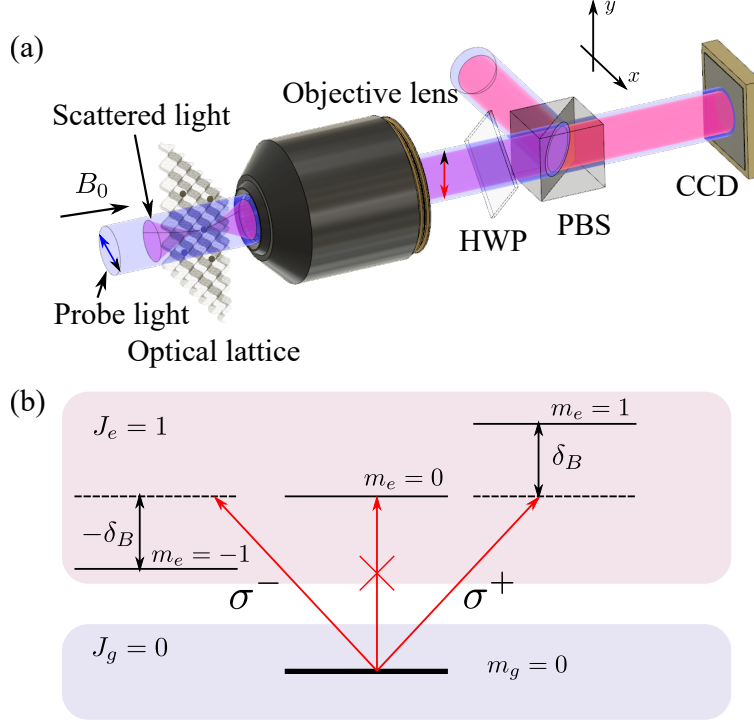[1]θ corresponds to twice the angle of the fast axis of the HWP from x axis.

Figure 7.1:   (a) Schematics of Faraday imaging of single atoms in an optical lattice [119].   Off-resonant linearly polarized probe light induces an elastically scattered coherent light field with the polarization orthogonal to that of the probe beam in the presence of a bias magnetic field B_0.   This results in the rotation of the polarization axis, which is detected at the charge-coupled-device (CCD) camera after a half-wave-plate (HWP) and a polarizing-beam-splitter (PBS). (b) Relevant energy level and transition diagram of Faraday imaging. The opposite sign of the detunings $\pm\delta_B$ of the $\sigma_{\pm}$ component of the probe light with respect to the associated $J_g = 0 \rightarrow J_e = 1, m_e = \pm 1$ transitions, respectively, in the presence of the magnetic field results in the rotation of the axis of the linear polarization.

CCD is given by

$$I_{\text{detect}} = \frac{\epsilon_0 c}{2} \left| (\boldsymbol{E}_{\text{sc}} + \boldsymbol{E}_{\text{probe}}) \cdot \hat{\boldsymbol{e}}_\theta \right|^2 , \tag{7.2}$$

where ϵ_0 and c are the vacuum permeability and speed of light, respectively. The signal of this detection S is the difference of the number of photoelectron of the CCD between in the presence and the absence of an atom:

$$S = \eta_{\text{det}} \frac{\epsilon_0 c}{2} \frac{\lambda \tau}{hc} \int_{\text{det}} \mathrm{d}A \left(\left| (\boldsymbol{E}_{\text{sc}} + \boldsymbol{E}_{\text{probe}}) \cdot \hat{\boldsymbol{e}}_\theta \right|^2 - \left| \boldsymbol{E}_{\text{probe}} \cdot \hat{\boldsymbol{e}}_\theta \right|^2 \right) \tag{7.3}$$

$$\simeq \eta_{\text{det}} \frac{\epsilon_0 c}{2} \frac{\lambda \tau}{hc} 2 \int_{\text{det}} \mathrm{d}A \left(\boldsymbol{E}_{\text{sc}} \cdot \hat{\boldsymbol{e}}_\theta \right) \left(\boldsymbol{E}_{\text{probe}} \cdot \hat{\boldsymbol{e}}_\theta \right) \tag{7.4}$$

where η_{det} is the total detection efficiency of the CCD. The parameter τ represents the temporal width of the probe pulse. The integral ranges the pixels of interests in this case. Here we assumed that the amplitude of the probe light is sufficiently larger than that of the scattered light: $|\boldsymbol{E}_{\text{probe}}| \gg |\boldsymbol{E}_{\text{sc}}|$.

Because the probe and the scattered light are both classical, each detection event obeys Poisson statistics, and thus the deviation of the number of photoelectrons is equal to square root of its mean value. Considering the error accumulation, the noise N is thus given by

$$N = \sqrt{\eta_{\text{det}} \frac{\epsilon_0 c}{2} \frac{\lambda \tau}{hc} \left(\int_{\text{det}} \left| (\boldsymbol{E}_{\text{sc}} + \boldsymbol{E}_{\text{probe}}) \cdot \hat{\boldsymbol{e}}_\theta \right|^2 + \int_{\text{det}} \left| (\boldsymbol{E}_{\text{probe}}) \cdot \hat{\boldsymbol{e}}_\theta \right|^2 \right) dA} \tag{7.5}$$

$$\simeq \sqrt{2\eta_{\text{det}} \frac{\epsilon_0 c}{2} \frac{\lambda \tau}{hc} \int_{\text{det}} |\boldsymbol{E}_{\text{probe}} \cdot \hat{\boldsymbol{e}}_\theta|^2 dA}. \tag{7.6}$$

We note that the noise from the probe with the presence and the absence of the atom is not correlated (different light), and we should take the root of the sum of squares.

Let us consider the case with $\theta = \pi/4$ and $\eta_{\text{det}} = 1$ (perfect detector). We denote $\boldsymbol{E}_{\text{sc}} \cdot \hat{\boldsymbol{e}}_{\pi/4}$ and $\boldsymbol{E}_{\text{probe}} \cdot \hat{\boldsymbol{e}}_{\pi/4}$ as $E_{\text{sc}}/\sqrt{2}$ and $E_{\text{probe}}/\sqrt{2}$, respectively. We can derive the expression for signal-to-noise ratio R_{SN} as follows:

$$R_{\text{SN}} = \sqrt{\frac{\epsilon_0 c}{2}} \frac{\int_{\text{det}} dA E_{\text{sc}} E_{\text{probe}}}{\sqrt{\int_{\text{det}} dA |E_{\text{probe}}|^2}} \sqrt{\frac{\lambda \tau}{hc}}. \tag{7.7}$$

For a large δ_B/Γ, R_{SN} becomes

$$R_{\text{SN}} = \sqrt{\frac{\Gamma \tau s \eta}{2}} C_{\text{sc,probe}}, \tag{7.8}$$

where

$$C_{\text{sc,probe}} = \int_{\text{det}} E_{\text{sc}} \cdot E_{\text{probe}} dA \left/ \sqrt{\int |E_{\text{sc}}|^2 dA} \sqrt{\int_{\text{det}} |E_{\text{probe}}|^2 dA} \right. \tag{7.9}$$

is the quantity representing the level of the spatial mode-matching between the probe beam $\boldsymbol{E}_{\text{probe}}(r)$ and the scattered light $\boldsymbol{E}_{\text{sc}}(r)$, and

$$s = \frac{I_0/I_{\text{sat}}}{1 + (2\delta_B/\Gamma)^2} \simeq \frac{I_0/I_{\text{sat}}}{(2\delta_B/\Gamma)^2} \qquad (\delta_B \gg \Gamma) \tag{7.10}$$

is the saturation parameter with a saturation intensity $I_{\text{sat}} = \pi hc\Gamma/(3\lambda^3)$ and the probe intensity $I_0 = (\epsilon_0 c/2)|E_0|^2$. The number of photon absorption N_{abs} is given for a large δ_B/Γ as follows:

$$N_{\text{abs}} = \frac{\Gamma \tau}{2} s. \tag{7.11}$$

From Eqs. (7.8) and (7.11), we obtain the important following relation:

$$N_{\text{abs}} = R_{\text{SN}}^2/(\eta C_{\text{sc,probe}}^2). \tag{7.12}$$

The maximum values of η and $C_{\text{sc,probe}}$ are $1/2$ for $A_N = 1$ and 1 for $\boldsymbol{E}_{\text{probe}}(r) = \boldsymbol{E}_{\text{sc}}(r)$ with a sufficiently large integration area, respectively. Note that this high level of mode matching is achieved only for a particular single site. If we consider the probe beam sufficiently broad compared to the lattice constant, $C_{\text{sc,probe}} = 0.85$ for the optimal integration area can be derived by a simple

calculation. From these considerations, we conclude that the number of photon absorptions of the probe beam is never less than 2 at $R_{SN} = 1$. We also remark that, in this detection, the signal appears as the DC component of the detector output, as a matter of course for imaging with a camera. However, the DC component suffers from a flicker noise, or $1/f$ noise, which prevents to achieve to the imaging condition given in Eq. (7.12).

7.2   Proposed Schemes for nondestructive detections

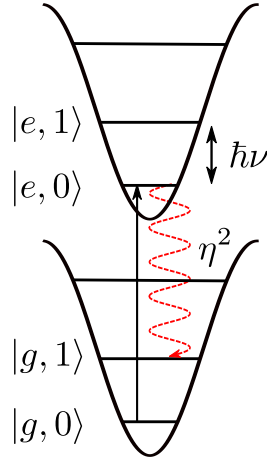### 7.2.1   Magic condition optical traps for the probe transition

Figure 7.2:   Vibrational level structure of an atom tightly confined in an optical lattice with a magic-wavelength condition ($\nu_e = \nu_g = \nu$) for the transition for probing. During the absorption process, the probe laser beam whose linewidth is much narrower than the trap frequency ν is tuned to the well-resolved resonance of the $|g, 0\rangle \rightarrow |e, 0\rangle$ transition. During the spontaneous emission process, the transition predominantly occurs between the vibrational ground states in the electronic ground $|g, 0\rangle$ and excited $|e, 0\rangle$ states, and the transition accompanying the change in one vibrational quantum number $|e, 0\rangle \rightarrow |g, 1\rangle$ is suppressed by the square of the Lamb-Dicke factor ζ compared to the transition $|e, 0\rangle \rightarrow |g, 0\rangle$.

We consider the two strategies to overcome the fundamental limitation derived in the previous section. The first, applicable to an atom that has an electronic ground state without spin degrees of freedom, is to utilize tight confinement of the atom under a magic-wavelength condition of the optical lattice for the transition for probing (See Fig. 7.2). In general, vibrational quantum number can change without any preference during the probe transition. If we irradiate the probe light to the atom tightly confined in the optical lattice site in three dimensions formed by the magic-wavelength light of the probe transition, the probe photon absorption and subsequent spontaneous emission process predominantly occur between the vibrational ground states in the electronic ground and excited states (carrier), and the transition accompanying the change in one vibrational quantum number (sideband) is suppressed by the square of the Lamb-Dicke factor $\zeta = \sqrt{E_R/(h\nu)}$ compared

to the transition between the same vibrational quantum numbers [121]. Here $E_R = \hbar^2 k_{\text{trap}}^2 / 2m$ is the recoil energy of the trapping light and ν is the trapping frequency. Here k_{trap} is the wavenumber of the trap laser and m is the atom mass. For simplicity, we consider the case where the trapping frequencies are the same for all three directions, and Γ and the linewidth of the probe light $\Delta\omega_{\text{probe}}$ are sufficiently narrow such that the probe laser is solely resonant to the carrier transition, which is well-resolved from the sideband transitions: $\Gamma, \Delta\omega_{\text{probe}} \ll \nu$. Then, we can repeat the photon absorption and subsequent spontaneous emission between the vibrational ground states before $N_{\text{abs}} \times 3\zeta^2$ reaches one, and therefore the criterion for "nondestructive" relaxes as $N_{\text{abs}} < 1/(3\zeta^2)$. We note this scheme does not require cooling procedure during the imaging, such as Raman sideband cooling. While the fidelities of the atom detection with some cooling methods could be now even higher than those in the first demonstrations [3, 5, 6], in our work, however, we specifically discuss more stringent probing condition in which the vibrational state of an atom in each lattice site minimally changes. Regarding Yb atoms, the realization of Lamb-Dicke confinement with $\zeta = 0.11$ in the "magic-like" lattice for the $^1S_0 \leftrightarrow {}^3P_1$ transition is already demonstrated using the 532-nm laser light with an appropriate polarization choice [15].

7.2.2 Scanning heterodyne Faraday detection with a squeezed vacuum

However, in general cases of atoms with spins in the ground state, the situation is not so simple. It is true that, in a magic-wavelength trap, we can think of a scheme of spin-preserving probing such as a closed, cyclic transition with appropriate polarization of probe light, or spin-non-preserving probing of one particular spin-component, say spin-up, and later performing optical pumping to the original spin-up state with shelving another spin-component, say spin-down, to states irrelevant for probing, and finally returning the atom to their original spin-down state. However, here we think of a much simpler scheme where no additional processes that influence the performance of the nondestructive detection are required other than probing. If the detection without photon absorption is possible, it is ideal for realizing nondestructive detection. For this purpose, we propose the second scheme of a scanning-type microscope in the confocal configuration with the use of a broadband squeezed vacuum and heterodyne detection. In this scheme, we use a coherent local oscillator beam in addition to the probe light with different frequencies. It enables detection of scattered light avoiding $1/f$ noise. An imaging system we consider is shown in Fig. 7.3.

Note that a squeezed vacuum is fragile to branching. Array detectors such as CCD cameras are not compatible with squeezed light because imaging with array detectors involves light branching to each detector segment. Therefore, measurement should be completed for each site with a single balanced detection mode scanning one-by-one as shown in Fig. 7.3. Mode-matching and scanning with the single site addressing level can be accomplished by a digital micromirror device and a galvano mirror system, for example.

The target site is selectively illuminated by an off-resonant weak probe laser beam with an angular frequency ω_L and vertical linear polarization through an objective lens 2 (OBJ2) and a polarizing
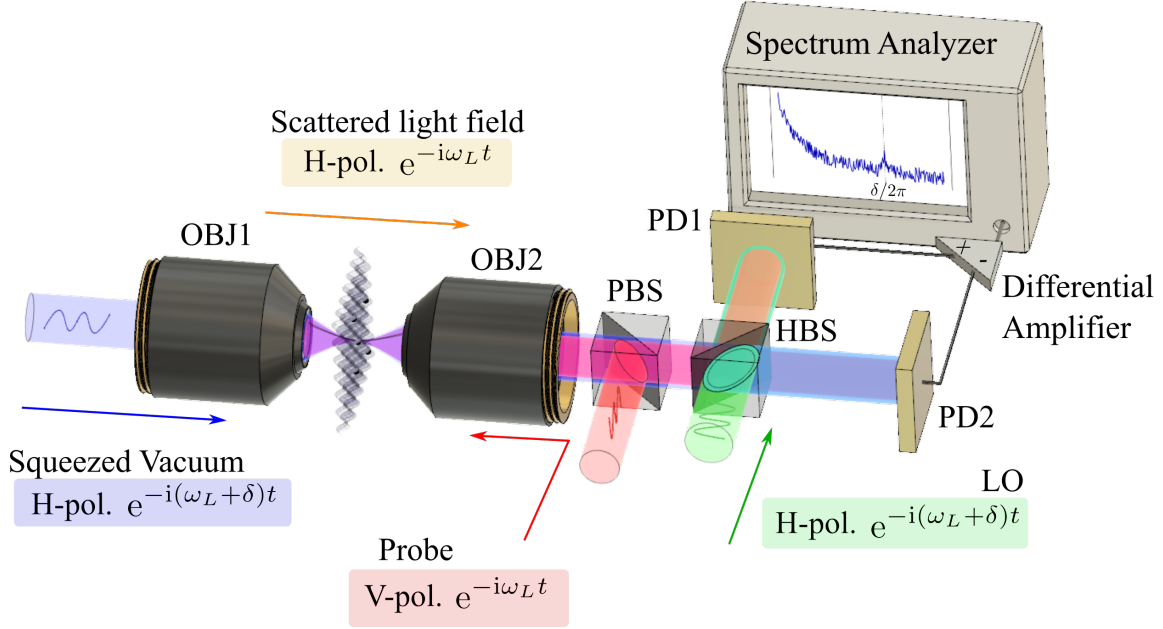
Figure 7.3: Scanning-type quantum gas microscope in the confocal configuration with the use of a broadband squeezed vacuum. An off-resonant vertically polarized probe laser beam is irradiated to a single atom through an objective lens OBJ2, inducing the horizontally polarized coherent elastic scattered light field. This light field is detected via the heterodyne measurement scheme consisting of the local oscillator beam LO, half-beam splitter HBS, two photo-detectors PD1 and PD2, and spectrum analyzer. At the same time, the horizontally polarized squeezed vacuum is focused to the single atom through an objective lens OBJ1 and is fed into the input of the HBS. With the aid of the squeezed vacuum, the signal for the atom is detected with enhanced sensitivity at a radio-frequency component of $\delta/(2\pi)$ below the shot noise level. PBS represents a polarizing-beam splitter. The angular frequency and the polarization of each light field are shown.

beam splitter (PBS). The probe light induces an electric field whose angular frequency ω_L is the same as that of the probe light [122], and its polarization is horizontal.

This elastically scattered coherent electric field is detected at the photo-detectors (PD1 and PD2) using the heterodyne method with the LO light with an angular frequency $\omega_L + \delta$ with δ within the squeezed bandwidth. A squeezed vacuum light beam having spectral components around the same angular frequency as the LO is focused to the same lattice site through an objective lens 1 (OBJ1). The ω_L and $\omega_L + 2\delta$ components of the squeezed vacuum reduce the shot noise in the detection around the frequency δ at the spectrum analyzer. Because the noise reduction requires exactly the same detuning and polarization as that of the signal light, the squeezed vacuum light cannot be separated from the scattered light and therefore a confocal configuration is inevitable. These three light beams are split by a half beam splitter (HBS) and then fall on two photo diodes PD1 and PD2 followed by signal subtraction via a differential amplifier.

Let us derive the R_{SN} for this scheme. Figure 7.4 shows an simplified illustration for the het-
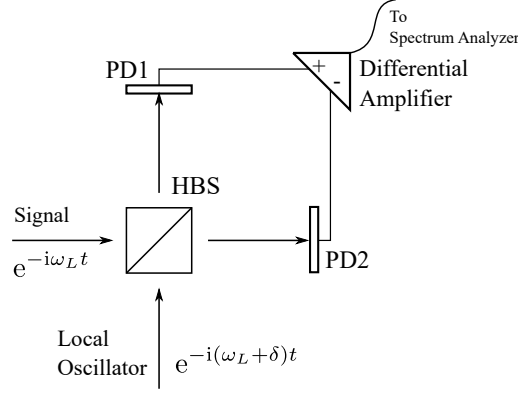
Figure 7.4: Simple schematic illustration of the heterodyne configuration.

erodyne detection of scattered light. We denote the annihilation operators for the scattered light, the local oscillator light, and the squeezed vacuum as $a_{\mathrm{sc}}(t) = a_{\mathrm{sc}}e^{-i\omega_L t}$, $B(t) = Be^{-i(\omega_L+\delta)t}$, and $a_{\mathrm{sv}}(t) = \int d\omega' \tilde{a}_{\mathrm{sv}}(\omega')e^{-i\omega' t}$, respectively. $\tilde{a}_{\mathrm{sv}}(\omega)$ is a frequency component of the annihilation operator for ω. Using the squeezing parameter for ω: $\xi(\omega)$, $\tilde{a}_{\mathrm{sv}}(\omega)$ is explicitly written as

$$\tilde{a}_{\mathrm{sv}}(\omega) = S^{\dagger}(\xi(\omega))a_{\mathrm{sv}}S(\xi(\omega)) \tag{7.13}$$

$$= a_{\mathrm{sv}}\cosh\xi - a_{\mathrm{sv}}^{\dagger}\sinh\xi, \tag{7.14}$$

$$S(\xi) \equiv \exp\left(\frac{\xi}{2}(a_{\mathrm{sv}}^2 - a_{\mathrm{sv}}^{\dagger\,2})\right), \tag{7.15}$$

where a_{sv} is the non-squeezed annihilation operator for the scattered light. We also define the state vector of each light and the vacuum as $|\alpha\rangle$, $|\beta\rangle$, and $|0\rangle$. $|\alpha\rangle$ and $|\beta\rangle$ are the coherent state: $a_{\mathrm{sc}}|\alpha\rangle = \alpha|\alpha\rangle$, $B|\beta\rangle = \beta|\beta\rangle$. The total state vector is $|\psi\rangle \equiv |\alpha\rangle|\beta\rangle|0\rangle$. In the Heisenberg picture, annihilation operators of the light arrives PD1 and PD2 are given by

$$c_{\pm} = \frac{1}{\sqrt{2}}\left(a_{\mathrm{sc}}(t) + a_{\mathrm{sv}}(t) \pm B(t)\right). \tag{7.16}$$

The heterodyne detection measures the δ-frequency component of $c_+^{\dagger}c_+ - c_-^{\dagger}c_-$:

$$R = \left(a_{\mathrm{sv}}^{\dagger}(\omega_L + 2\delta)B + a_{\mathrm{sv}}(\omega_L)B^{\dagger}\right) + a_{\mathrm{sc}}B^{\dagger}. \tag{7.17}$$

Remember broadband squeezing and here we assume $\xi(\omega + 2\delta) = \xi(\omega_L) = \xi$. The signal $\langle R\rangle$ and the noise $\sqrt{\langle R^2\rangle - \langle R\rangle^2}$ is derived as

$$\langle R\rangle = \alpha\beta^* \tag{7.18}$$

$$\sqrt{\langle R^2\rangle - \langle R\rangle^2} = |\beta|\sqrt{\left(e^{-2\xi}\cos^2\theta + e^{2\xi}\sin^2\theta\right)}, \tag{7.19}$$

where $\beta = |\beta|e^{i\theta}$. For $\theta = 0$, we can "squeeze" the noise. We let $\theta = 0$ in the following discussion.

We also should take the spatial mode of each field into account. The finite loss caused by real optical components as well as the imperfect spatial mode-matching between the LO and the

squeezed vacuum degrade the effective squeezing level. The effective squeezing parameter ξ_{eff}, the transmission of the optical system T, and the spatial overlap between the squeezed vacuum and the LO field $C_{\text{sv,LO}}$ are related as [123]

$$e^{-2\xi_{\text{eff}}} = 1 - (1 - e^{-2\xi})TC^2_{\text{sv,LO}}, \tag{7.20}$$

where

$$C_{\text{sv,LO}} = \int_{\text{det}} \boldsymbol{E}_{\text{sv}} \cdot \boldsymbol{E}_{\text{LO}} \mathrm{d}A \bigg/ \sqrt{\int |E_{\text{sv}}|^2 \mathrm{d}A} \sqrt{\int |E_{\text{LO}}|^2 \mathrm{d}A}. \tag{7.21}$$

We obtain the expression for R_{SN}:

$$R_{\text{SN}} = \sqrt{\frac{\Gamma \tau}{2}} s\eta \frac{C_{\text{sc,LO}}}{\sqrt{1 - (1 - e^{-2\xi})TC^2_{\text{sv,LO}}}}. \tag{7.22}$$

Note that in the expression of $C_{\text{sc,LO}}$, E_{probe} in Eq. (7.9) is replaced with E_{LO}. Substituting $\xi = 0$, this recovers Eq. (7.8) except a factor $\sqrt{2}$, which arises from the difference between the homodyne and the heterodyne detection. In the following calculation we assume a Gaussian mode for the squeezed vacuum. LO's spatial mode is the only adjustable one.

What is the optimized value of R_{SN}? The answer of this question can be revealed by a variational calculation, which immediately implies that the optimized E_{LO} takes the form of $uE_{\text{sc}} + vE_{\text{sv}}$, assuming the area of the detector is sufficiently large. The normalization of fields

$$\int |E_{\text{sc}}|^2 \mathrm{d}A = \int |E_{\text{sv}}|^2 \mathrm{d}A = \int |E_{\text{LO}}|^2 \mathrm{d}A = 1 \tag{7.23}$$

does not change R_{SN}. Then we obtain the following equations

$$u^2 + v^2 + 2uvC_{\text{sv,LO}} = 1, \tag{7.24}$$

$$F \equiv \frac{C_{\text{sc,LO}}}{\sqrt{1 - (1 - e^{-2\xi})TC^2_{\text{sv,LO}}}} = \frac{u + vC_{\text{sc,sv}}}{\sqrt{1 - (1 - e^{-2\xi})T(uC_{\text{sc,sv}} + v)^2}}. \tag{7.25}$$

This indicates that the mode-matching dependence of the R_{SN} is finally characterized by

$$C_{\text{sc,sv}} = \int \boldsymbol{E}_{\text{sv}} \cdot \boldsymbol{E}_{\text{sc}} \mathrm{d}A \bigg/ \sqrt{\int |E_{\text{sv}}|^2 \mathrm{d}A} \sqrt{\int |E_{\text{sc}}|^2 \mathrm{d}A}, \tag{7.26}$$

which represents the level of the spatial overlap between the squeezed vacuum and scattered light field. The necessary condition for the existence of solutions for Eqs. (7.24) and (7.25) is

$$\left(1 - (1 - e^{-2\xi})T\right)\left(1 - C^2_{\text{sc,sv}}\right)F^2 - \left(1 - C^2_{\text{sc,sv}}\right)\left(1 - (1 - e^{-2\xi})(1 - C^2_{\text{sc,sv}})T\right) \leq 0 \tag{7.27}$$

$$\Rightarrow F \leq \sqrt{1 + C^2_{\text{sc,sv}} \frac{T(1 - e^{-2\xi})}{1 - T(1 - e^{-2\xi})}}. \tag{7.28}$$

We thus obtain the following expression of the optimized R_{SN}

$$(R_{\mathrm{SN}})_{\mathrm{opt}} = \sqrt{N_{\mathrm{abs}}}\eta\sqrt{1 + C_{\mathrm{sc,sv}}^2 \frac{T(1 - e^{-2\xi})}{1 - T(1 - e^{-2\xi})}}. \tag{7.29}$$

Note that the optimal spatial mode of the local oscillator changes as the squeezing level changes, as shown in Fig. 7.5(a). By taking the maximum value of 0.9 for $C_{\mathrm{sc,sv}}$ and setting the $(R_{\mathrm{SN}})_{\mathrm{opt}} = 1$ in Eq. (7.29), we obtain the number of photon absorption events N_{abs} to maintain the R_{SN} equal to 1 as a function of the squeezing level. Figure 7.5(b) shows the results with the realistic condition of $A_N = 0.8$ and $T = 0.95$. The calculated squeezing level required to achieve nondestructive detection indicated by the shaded area in the figure ($N_{\mathrm{abs}} < 1$) is 7.7dB, which corresponds to average photon number of 1.0.

(a)

(b)
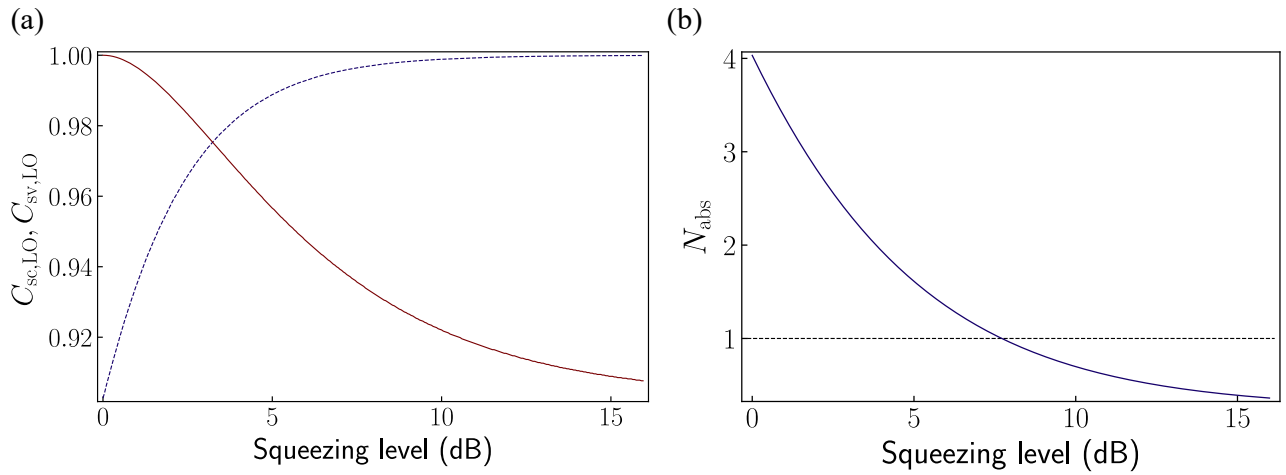
Figure 7.5: (a)Optimal values of $C_{\mathrm{sc,LO}}$ and $C_{\mathrm{sv,LO}}$ in the maximization of the R_{SN} via adjusting the LO field spatial mode. The optimal spatial mode of the local oscillator changes as the squeezing level changes. (b)Number of photon absorption events N_{abs} to maintain the R_{SN} equal to 1 plotted as a function of squeezing level. Conditions of $A_N = 0.8$, $T = 0.95$, and the optimal local oscillator light spatial mode are assumed.

7.3 Feasibility

The feasibility of the proposed scheme is discussed by considering an example of ultracold two-electron atoms in a metastable state. While the transition from the ground states of alkali atoms or two-electron atoms mostly lies in the visible region, a higher level of squeezing has been realized in the near-infrared region [124]. Notably, the transitions from the metastable states of two-electron atoms have optical transitions in the near-infrared region; for example, a Yb atom has an electric-dipole allowed transition between the $^3P_0$ and $^3D_1$ states with a corresponding wavelength of $\lambda = 1389$ nm. The transitions associated with the $^3P_0$ state can be used for probing a SU($\mathcal{N}$) symmetric Fermi Hubbard model realized in the metastable $^3P_0$ state for fermionic isotopes of Yb

atoms. A glass-cell system with an effective numerical aperture A_N of 0.7 of two objective lenses on both sides similar to our scheme is commercially available. Assuming 15 dB of squeezing and 95% transmittance of the optical system ($T = 0.95$) with $A_N = 0.8$ and $C_{sc,sv} = 0.9$, we expect the relation

$$N_{abs} = 0.39 \times R_{SN}^2, \tag{7.30}$$

which implies nondestructive detection of a single atom in a single site. As a typical experimental condition, we consider a probe beam with a pulse width of $\tau = 1010\,\mu s$, intensity of $I_0/I_{sat} = 1.03 \times 10^3$, and detuning of $\delta_B/\Gamma = 100$. With these parameters, the number of absorbed photons can be estimated to be $N_{abs} = 0.39$ from Eq. (7.11) and the signal-to-noise ratio $R_{SN} = 1.0$ from Eq. (7.29), consistent with Eq. (7.30), thus realizing nondestructive imaging for a single atom in a single site. The measurement time of $\tau = 10\,\mu s$ is sufficiently short to perform repetitive measurements for many sites in a scanning manner in a relatively shallow lattice. In fact, for example, when we consider 15 atoms in an optical lattice with a depth of $10E_R$, where the tunneling time $\tau_{hop} = \hbar/J$ is 8 ms for the lattice constant of 532 nm with J being the hopping energy, we can perform $N = 15$ measurements in $15\tau = 0.15$ ms, during which the number of hopping to adjacent sites for all 15 atoms $N_{hop} = 15 \times 0.15\text{ms}/\tau_{hop}$ is 0.28. Note that the excitation of the atoms caused by the 15-dB squeezed vacuum is negligible because of the weak intensity comparable to I_{sat} and the squeezed bandwidth is assumed to be sufficiently broad to cover the heterodyne frequency of $\delta/(2\pi) = 1$ MHz.

The above-mentioned feasibility of the scheme using a squeezed vacuum is still limited when we consider the usefulness on the many-body level such as 15 atoms. However, by combining the two proposed approaches in this work, we can provide the route to a high-fidelity nondestructive measurement on the many-body level. Namely, we consider the scheme in which we perform a probing with a squeezed vacuum, described in the second part of the section 3, for atoms without internal-degrees of freedom in the ground state trapped in an optical lattice with a magic-wavelength condition for the probe transition, as described in the section 7.2.1. Then the nondestructive condition is relaxed by $4 \times \zeta^2$ where the additional contribution ζ^2 comes from the excitation with a blue sideband in the present off-resonant-excitation scheme, different from the resonant-excitation scheme considered in the section 3. Since the condition of $\zeta = 0.11$ is already realized [15], we can improve the performance up to $R_{SN} = 25$ with a probability of changing the vibrational state of $p = 0.39$ for a single atom. In other words, with the condition of $R_{SN} = 1$, p will be 1.6×10^{-2}, and therefore the change of the vibrational state is negligible. On the many-body level of 15 atoms, this means that less than one photon is scattered for detecting 15 atoms nondestructively about the vibrational state.

7.4   Conclusion

In conclusion, we have proposed a quantum gas microscope capable of nondestructive detection of a single atom enabling a number of fascinating research inquiries. We derive the general relation between the R_{SN} and photon absorption of a probe beam for dispersive Faraday quantum gas microscopy and show that the detection of the atom with the R_{SN} greater than unity should be

accompanied by the absorption of the probe beam by more than one photon. For an atom that has an electronic ground state without spin degrees of freedom, we find that the magic-wavelength condition of the optical lattice for the transition for probing enables detection of an atom with avoidance of excitations to higher-band. We also consider a more general scheme to detect an atom with an absorption of less than one photon based on a squeezed vacuum in a scanning microscope configuration. An application to ultracold two-electron atoms is also discussed. The combined scheme of the proposed two approaches enables a nondestructive measurement on the many-body level of about 15 atoms.

Conclusion and outlook

8.1 Conclusion

This thesis presents the realization of an ytterbium tweezer atom array toward the quantum computing featuring their unique properties of two-electron atoms, and schemes for nondestructive detection of atoms. We briefly review the achievements of our work.

- *Trapping and imaging of single atoms in an optical tweezer array* (Chapter 5)

  We generate a two-dimensional OT array with a wavelength of 532 nm focused by an objective lens with NA= 0.6. We successfully observe the fluorescence from trapped single atoms with the loading efficiency roughly 60% as a result of light-assisted collision, deduced from the clearly binarized photon counts from empty and filled sites. The clear separation offers the error probability of detection as low as 0.3%. The loss probability by the imaging is 5%. We cooled atoms heated by the imaging process using $^1S_0\leftrightarrow^3P_1$ transition, which is verified by a release-and-recapture technique. We measure the trapping frequency of atoms by a parametric loss spectroscopy and deduce the waist of tweezers as $1.0\,\mu$m. The rearrangement of atoms to obtain a defect-free atom array by a fast feedback to multitone RF is also performed for both 1D and 2D array.

- *High-resolution spectroscopy and single-photon Rydberg excitation* (Chapter 6)

  We observe a sideband-resolved spectrum of the $^1S_0\leftrightarrow^3P_2$ ($m_J = 0$) transition for single atoms. The mean occupation quantum number for the motional eigenstate along the radial direction is deduced from the spectrum as 1.46 ± 1.01, which agrees with a calculation of the cooling process.

  Spectroscopy of Rydberg states by a single-photon excitation from the $^3P_2$ state is also present, as well as a two-photon spectroscopy with $^1P_1$ as an intermediate state. ^3D and $^3S_1$ series of Rydberg states are observed, including newly observed $^3D_3$ states thanks to our choice of the $J = 2$ state as the initial state.

Though we performed the above spectroscopy using atomic ensembles in an optical dipole trap, the single-photon excitation to Rydberg states of single atoms is also demonstrated.

- *Schemes for nondestructive detection of single atoms* (Chapter 7)

  We first derive the relation between the signal-to-noise ratio and the number of photon absorption of the dispersive homodyne Faraday imaging performed in our group previously [119], which results in the important consequence that this technique does not allow nondestructive detection. We then present two schemes: The first one uses a magic wavelength optical traps for the probe transition which well preserves the motional state of an atom. The second one is a heterodyne scanning Faraday imaging with the aid of a squeezed vacuum state. We derive the signal-to-noise ratio for this scheme and we show the detection without photon absorption is possible using this scheme.

8.2   Outlook

We present directions in our plan toward the large-scale and high-fidelity quantum computing below.

- Imaging with $^1S_0 \leftrightarrow {}^1P_1$ transition

  Though we have succeeded in imaging of single atoms using the $^1S_0 \leftrightarrow {}^3P_1$ transition, we are going to switch it to the $^1S_0 \leftrightarrow {}^1P_1$ transition for the following three reasons: First, the narrow linewidth of the $^1S_0 \leftrightarrow {}^3P_1$ transition requires small potential differences between the ground state and excited states to obtain high-performance of the imaging, which is not possible for ^{171}Yb atoms for $\lambda = 532$ nm trapping beam due to the interplay between the tensor shift and the hyperfine structure [42]. Working with the broad linewidth $^1S_0 \leftrightarrow {}^1P_1$ transition does not suffer from this problem. Second, the large difference of the wavelength allows the clear separation of the MOT beam ($\lambda = 556$ nm) and trapping beam ($\lambda = 532$ nm) from the fluorescence from atoms ($\lambda = 399$ nm). This also enables the cooling of atoms with the $^1S_0 \leftrightarrow {}^3P_1$ transition during the imaging with the $^1S_0 \leftrightarrow {}^1P_1$.

- Sideband cooling using the $^1S_0 \leftrightarrow {}^3P_2$ transition

  The clearly resolved sideband spectrum of the $^1S_0 \leftrightarrow {}^3P_2$ transition enables the cooling to the motional ground state of atoms, with the aid of repumpers: $^3P_2 \leftrightarrow {}^3S_1(\lambda = 770$ nm) and $^3P_0 \leftrightarrow {}^3S_1(\lambda = 649$ nm). The cooling to the motional ground state is a crucial factor for the realization of coherent excitation of atoms.

- Arbitrary two-dimensional array generated by a spatial-light-modulator

  Though our choice of AOD for generation of OT arrays is reasonable to obtain square and small size arrays, this does not offer arbitrary geometry of traps. We are going to use a spatial-light-modulator (SLM) instead of AODs for generation of OT arrays, which enables the arbitrary

geometry of traps. AODs will be also used to generate tweezers to move and rearrange atoms, because it is difficult to dynamically change the trap geometry using a SLM.

- Utilization of the $^3P_0$ state

  The $^3P_0$ state is another existing metastable state of AE(L)A. We are going to use this state in addition to the $^3P_2$ state. Because this state doesn't have the vector and tensor polarizability, we are able to realize robust magic-wavelength condition of optical trap by tuning to an appropriate wavelength: 759 nm for the case of Yb atoms, for example. 759 nm wavelength laser can be obtained from a Ti:Sapphire laser. The objective lens used for the trapping is also designed to be diffraction limited for 759 nm light.

Light shift and Zeeman shift

The degeneracy of magnetic sublevels m lifts by external fields such as a magnetic field (Zeeman shift) or an AC-stark shift (Light shift). In this appendix, we describe the hamiltonian and the calculation of its eigenenergies in the presence of Zeeman shift and light shift. Here we consider bosonic isotopes of Yb which does not have hyperfine structures, but the same discussion holds for fermionic isotopes.

A.1 Zeeman shift

The hamiltonian for the Zeeman effect by an applied magnetic field B is given by

$$\mathcal{H}_{ZS} = g_J \mu_B \boldsymbol{J} \cdot \boldsymbol{B}, \tag{A.1}$$

where $\boldsymbol{J}$ denotes the total electronic angular momentum, μ_B is the Bohr magneton. g_J is the g-factor of $\boldsymbol{J}$ and is related to the g-factor of orbital angular momentum $\boldsymbol{L}$ and the spin $\boldsymbol{S}$ as

$$g_J = g_L + (g_S - g_L)\frac{J(J+1) + S(S+1) - L(L+1)}{2J(J+1)} \tag{A.2}$$

$$\simeq \frac{3}{2} + \frac{S(S+1) - L(L+1)}{2J(J+1)}. \tag{A.3}$$

Here we used $g_L = 3/2$ and $g_S \simeq 2$.

A.2 Light shift

The light shift induced by a laser with a polarization unit vector $\boldsymbol{u}$ is given by

$$\mathcal{H}_{LS} = -\frac{h}{4}I\left(\alpha_{nJ}^{(S)} - i\alpha_{nJ}^{(V)}\frac{(\boldsymbol{u}^* \times \boldsymbol{u}) \cdot \boldsymbol{J}}{2J} + \alpha_{nJ}^{(T)}\frac{3\left((\boldsymbol{u}^* \cdot \boldsymbol{J})(\boldsymbol{u} \cdot \boldsymbol{J}) + (\boldsymbol{u} \cdot \boldsymbol{J})(\boldsymbol{u}^* \cdot \boldsymbol{J}) - 2J^2\right)}{2J(2J-1)}\right), \tag{A.4}$$

where $\alpha_{nJ}^{(S)}$, $\alpha_{nJ}^{(V)}$ and $\alpha_{nJ}^{(T)}$ are the scalar, vector and tensor polarizability, respectively [125]. We consider only linear polarization $\boldsymbol{u}^* = \boldsymbol{u}$ in which the second term vanishes. For the spinless state such as $^1S_0$, only the scalar polarizability gives the energy shift.

The scalar and tensor polarizabilities for the $^1S_0$, $^3P_1$, and $^3P_2$ state of ^{174}Yb are measured experimentally and summarized in Table A.1 [15, 126].

Table A.1: Measured scalar and tensor polarizabilities for the $^1S_0$, $^3P_1$, and $^3P_2$ states of ^{174}Yb.

	$\alpha^{(S)}$	$\alpha^{(T)}$	Unit
$^1S_0$	37.9		Hz/(W/cm^2)
$^3P_1$	22.4	-7.6	Hz/(W/cm^2)
$^3P_2$	46.0	7.5	Hz/(W/cm^2)

A.3   Calculation of eigenenergies

In the presence of both Zeeman shift and light shift, eigenenergies are derived by diagonalizing the total hamiltonian $\mathcal{H}_{tot} = \mathcal{H}_{ZS} + H_{LS}$. Figure A.1 shows the calculated shift of the eigenenergies from the bare resonance of Zeeman substates of the $^3P_1$ state for the potential depth 0.56 mK and the magnetic field aligned along the polarization of the trapping beam. The experimentally obtained spectrum for the same condition is also shown in the right panel. We irradiated 556 nm light before the imaging scanning the detuning and the strenght of the magnetic field. The resonance appears as the loss of atoms.
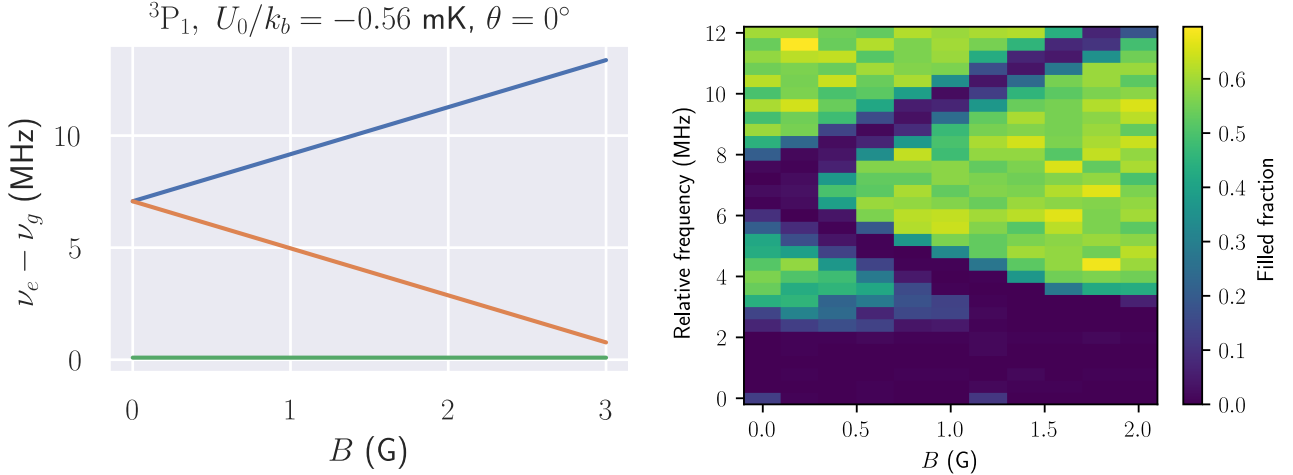
Figure A.1: The calculated and experimentally obtained spectrum of Zeeman substates of the $^3P_1$ state for the potential depth -0.56 mK with the magnetic field aligned along the polarization.

Bibliography

[1] Waseem S. Bakr, Jonathon I. Gillen, Amy Peng, Simon Fölling, and Markus Greiner. A quantum gas microscope for detecting single atoms in a Hubbard-regime optical lattice. *Nature*, 462(7269):74, 2009. `doi:10.1038/nature08482`.

[2] Jacob F. Sherson, Christof Weitenberg, Manuel Endres, Marc Cheneau, Immanuel Bloch, and Stefan Kuhr. Single-atom-resolved fluorescence imaging of an atomic Mott insulator. *Nature*, 467(7311):68, 2010. `doi:10.1038/nature09378`.

[3] Maxwell F. Parsons, Florian Huber, Anton Mazurenko, Christie S. Chiu, Widagdo Setiawan, Katherine Wooley-Brown, Sebastian Blatt, and Markus Greiner. Site-Resolved Imaging of Fermionic ^{6}Li in an Optical Lattice. *Physical Review Letters*, 114(21):213002, 2015. `arXiv:1504.04397`, `doi:10.1103/physrevlett.114.213002`.

[4] Elmar Haller, James Hudson, Andrew Kelly, Dylan A. Cotta, Bruno Peaudecerf, Graham D. Bruce, and Stefan Kuhr. Single-atom imaging of fermions in a quantum-gas microscope. *Nature Physics*, 11(9):738–742, 2015. `arXiv:1503.02005`, `doi:10.1038/nphys3403`.

[5] Lawrence W. Cheuk, Matthew A. Nichols, Melih Okan, Thomas Gersdorf, Vinay V. Ramasesh, Waseem S. Bakr, Thomas Lompe, and Martin W. Zwierlein. Quantum-Gas Microscope for Fermionic Atoms. *Physical Review Letters*, 114(19):193001, 2015. `arXiv:1503.02648`, `doi:10.1103/physrevlett.114.193001`.

[6] Ahmed Omran, Martin Boll, Timon A. Hilker, Katharina Kleinlein, Guillaume Salomon, Immanuel Bloch, and Christian Gross. Microscopic Observation of Pauli Blocking in Degenerate Fermionic Lattice Gases. *Physical Review Letters*, 115(26):263001, 2015. `doi:10.1103/physrevlett.115.263001`.

[7] Rajibul Islam, Ruichao Ma, Philipp M. Preiss, M. Eric Tai, Alexander Lukin, Matthew Rispoli, and Markus Greiner. Measuring entanglement entropy in a quantum many-body system. *Nature*, 528(7580):77–83, 2015. `doi:10.1038/nature15750`.

[8] G. J. A. Edge, R. Anderson, D. Jervis, D. C. McKay, R. Day, S. Trotzky, and J. H. Thywissen. Imaging and addressing of individual fermionic atoms in an optical lattice. *Physical Review A*, 92(6):063406, 2015. `arXiv:1510.04744`, `doi:10.1103/physreva.92.063406`.

[9] Martin Miranda, Ryotaro Inoue, Yuki Okuyama, Akimasa Nakamoto, and Mikio Kozuma. Site-resolved imaging of ytterbium atoms in a two-dimensional optical lattice. *Physical Review A*, 91(6):063414, 2015. `doi:10.1103/physreva.91.063414`.

[10] Martin Boll, Timon A. Hilker, Guillaume Salomon, Ahmed Omran, Jacopo Nespolo, Lode Pollet, Immanuel Bloch, and Christian Gross. Spin- and density-resolved microscopy of antiferromagnetic correlations in Fermi-Hubbard chains. *Science*, 353(6305):1257–1260, 2016. `arXiv:1605.05661`, `doi:10.1126/science.aag1635`.

[11] Maxwell F. Parsons, Anton Mazurenko, Christie S. Chiu, Geoffrey Ji, Daniel Greif, and Markus Greiner. Site-resolved measurement of the spin-correlation function in the Fermi-Hubbard model. *Science*, 353(6305):1253–1256, 2016. `arXiv:1605.02704`, `doi:10.1126/science.aag1430`.

[12] Daniel Greif, Maxwell F. Parsons, Anton Mazurenko, Christie S. Chiu, Sebastian Blatt, Florian Huber, Geoffrey Ji, and Markus Greiner. Site-resolved imaging of a fermionic Mott insulator. *Science*, 351(6276):953–957, 2016. `arXiv:1511.06366`, `doi:10.1126/science.aad9041`.

[13] Lawrence W. Cheuk, Matthew A. Nichols, Katherine R. Lawrence, Melih Okan, Hao Zhang, Ehsan Khatami, Nandini Trivedi, Thereza Paiva, Marcos Rigol, and Martin W. Zwierlein. Observation of spatial charge and spin correlations in the 2D Fermi-Hubbard model. *Science*, 353(6305):1260–1264, 2016. `arXiv:1606.04089`, `doi:10.1126/science.aag3349`.

[14] Lawrence W. Cheuk, Matthew A. Nichols, Katherine R. Lawrence, Melih Okan, Hao Zhang, and Martin W. Zwierlein. Observation of 2D Fermionic Mott Insulators of ^{40}K with Single-Site Resolution. *Physical Review Letters*, 116(23):235301, 2016. `arXiv:1604.00096`, `doi:10.1103/physrevlett.116.235301`.

[15] Ryuta Yamamoto, Jun Kobayashi, Takuma Kuno, Kohei Kato, and Yoshiro Takahashi. An ytterbium quantum gas microscope with narrow-line laser cooling. *New Journal of Physics*, 18(2):023016, 2016. `doi:10.1088/1367-2630/18/2/023016`.

[16] Martin Miranda, Ryotaro Inoue, Naoki Tambo, and Mikio Kozuma. Site-resolved imaging of a bosonic Mott insulator using ytterbium atoms. *Physical Review A*, 96(4):043626, 2017. `arXiv:1704.07060`, `doi:10.1103/physreva.96.043626`.

[17] Peter T. Brown, Debayan Mitra, Elmer Guardado-Sanchez, Peter Schauß, Stanimir S. Kondov, Ehsan Khatami, Thereza Paiva, Nandini Trivedi, David A. Huse, and Waseem S. Bakr. Spin-imbalance in a 2D Fermi-Hubbard system. *Science*, 357(6358):1385–1388, 2017. `arXiv:1612.07746`, `doi:10.1126/science.aam7838`.

[18] Christian Gross and Waseem S. Bakr. Quantum gas microscopy for single atom and spin detection. *Nature Physics*, 17(12):1316–1323, 2021. `doi:10.1038/s41567-021-01370-5`.

[19] Adam M. Kaufman and Kang-Kuen Ni. Quantum science with optical tweezer arrays of ultracold atoms and molecules. *Nature Physics*, pages 1–10, 2021. `doi:10.1038/s41567-021-01357-2`.

[20] Nicolas Schlosser, Georges Reymond, Igor Protsenko, and Philippe Grangier. Sub-poissonian loading of single atoms in a microscopic dipole trap. *Nature*, 411(6841):1024–1027, 2001. `doi:10.1038/35082512`.

[21] Manuel Endres, Hannes Bernien, Alexander Keesling, Harry Levine, Eric R. Anschuetz, Alexandre Krajenbrink, Crystal Senko, Vladan Vuletic, Markus Greiner, and Mikhail D. Lukin. Atom-by-atom assembly of defect-free one-dimensional cold atom arrays. *Science*, 354(6315):1024–1027, 2016. `doi:10.1126/science.aah3752`.

[22] Daniel Barredo, Sylvain de Léséleuc, Vincent Lienhard, Thierry Lahaye, and Antoine Browaeys. An atom-by-atom assembler of defect-free arbitrary two-dimensional atomic arrays. *Science*, 354(6315):1021–1023, 2016. `arXiv:1607.03042`, `doi:10.1126/science.aah3778`.

[23] Antoine Browaeys and Thierry Lahaye. Many-body physics with individually controlled Rydberg atoms. *Nature Physics*, 16(2):132–142, 2020. `arXiv:2002.07413`, `doi:10.1038/s41567-019-0733-z`.

[24] Christian Gross and Immanuel Bloch. Quantum simulations with ultracold atoms in optical lattices. *Science*, 357(6355):995–1001, 2017. `doi:10.1126/science.aal3837`.

[25] Pascal Scholl, Michael Schuler, Hannah J. Williams, Alexander A. Eberharter, Daniel Barredo, Kai-Niklas Schymik, Vincent Lienhard, Louis-Paul Henry, Thomas C. Lang, Thierry Lahaye, Andreas M. Läuchli, and Antoine Browaeys. Quantum simulation of 2D antiferromagnets with hundreds of Rydberg atoms. *Nature*, 595(7866):233–238, 2021. `arXiv:2012.12268`, `doi:10.1038/s41586-021-03585-1`.

[26] Sepehr Ebadi, Tout T. Wang, Harry Levine, Alexander Keesling, Giulia Semeghini, Ahmed Omran, Dolev Bluvstein, Rhine Samajdar, Hannes Pichler, Wen Wei Ho, Soonwon Choi, Subir Sachdev, Markus Greiner, Vladan Vuletić, and Mikhail D. Lukin. Quantum phases of matter on a 256-atom programmable quantum simulator. *Nature*, 595(7866):227–232, 2021. `doi:10.1038/s41586-021-03582-4`.

[27] M. Saffman, T. G. Walker, and K. Mølmer. Quantum information with Rydberg atoms. *Reviews of Modern Physics*, 82(3):2313–2363, 2010. `arXiv:0909.4777`, `doi:10.1103/revmodphys.82.2313`.

[28] David S Weiss and Mark Saffman. Quantum computing with neutral atoms. *Physics Today*, 70(7):44–50, 2017. `doi:10.1063/pt.3.3626`.

[29] I. I. Beterov, I. N. Ashkarin, E. A. Yakshina, D. B. Tretyakov, V. M. Entin, I. I. Ryabtsev, P. Cheinet, P. Pillet, and M. Saffman. Fast three-qubit Toffoli quantum gate based on three-body Förster

resonances in Rydberg atoms. *Physical Review A*, 98(4):042704, 2018. `arXiv:1808.03473`, `doi:10.1103/physreva.98.042704`.

[30] Harry Levine, Alexander Keesling, Giulia Semeghini, Ahmed Omran, Tout T. Wang, Sepehr Ebadi, Hannes Bernien, Markus Greiner, Vladan Vuletić, Hannes Pichler, and Mikhail D. Lukin. Parallel Implementation of High-Fidelity Multiqubit Gates with Neutral Atoms. *Physical Review Letters*, 123(17):170503, 2019. `arXiv:1908.06101`, `doi:10.1103/physrevlett.123.170503`.

[31] A. Omran, H. Levine, A. Keesling, G. Semeghini, T. T. Wang, S. Ebadi, H. Bernien, A. S. Zibrov, H. Pichler, S. Choi, J. Cui, M. Rossignolo, P. Rembold, S. Montangero, T. Calarco, M. Endres, M. Greiner, V. Vuletić, and M. D. Lukin. Generation and manipulation of Schrödinger cat states in Rydberg atom arrays. *Science*, 365(6453):570–574, 2019. `arXiv:1905.05721`, `doi:10.1126/science.aax9743`.

[32] T. M. Graham, M. Kwon, B. Grinkemeyer, Z. Marra, X. Jiang, M. T. Lichtman, Y. Sun, M. Ebert, and M. Saffman. Rydberg-Mediated Entanglement in a Two-Dimensional Neutral Atom Qubit Array. *Physical Review Letters*, 123(23):230501, 2019. `arXiv:1908.06103`, `doi:10.1103/physrevlett.123.230501`.

[33] T. M. Graham, Y. Song, J. Scott, C. Poole, L. Phuttitarn, K. Jooya, P. Eichler, X. Jiang, A. Marra, B. Grinkemeyer, M. Kwon, M. Ebert, J. Cherek, M. T. Lichtman, M. Gillette, J. Gilbert, D. Bowman, T. Ballance, C. Campbell, E. D. Dahl, O. Crawford, N. S. Blunt, B. Rogers, T. Noel, and M. Saffman. Multi-qubit entanglement and algorithms on a neutral-atom quantum computer. *Nature*, 2022. `arXiv:2112.14589`, `doi:10.1038/s41586-022-04603-6`.

[34] J. E. Bjorkholm. Collision-limited lifetimes of atom traps. *Physical Review A*, 38(3):1599–1600, 1988. `doi:10.1103/physreva.38.1599`.

[35] Kai-Niklas Schymik, Sara Pancaldi, Florence Nogrette, Daniel Barredo, Julien Paris, Antoine Browaeys, and Thierry Lahaye. Single Atoms with 6000-Second Trapping Lifetimes in Optical-Tweezer Arrays at Cryogenic Temperatures. *Physical Review Applied*, 16(3):034013, 2021. `arXiv:2106.07414`, `doi:10.1103/physrevapplied.16.034013`.

[36] Harry Levine, Alexander Keesling, Ahmed Omran, Hannes Bernien, Sylvain Schwartz, Alexander S. Zibrov, Manuel Endres, Markus Greiner, Vladan Vuletić, and Mikhail D. Lukin. High-Fidelity Control and Entanglement of Rydberg-Atom Qubits. *Physical Review Letters*, 121(12):123603, 2018. `arXiv:1806.04682`, `doi:10.1103/physrevlett.121.123603`.

[37] T. Xia, M. Lichtman, K. Maller, A. W. Carr, M. J. Piotrowicz, L. Isenhower, and M. Saffman. Randomized Benchmarking of Single-Qubit Gates in a 2D Array of Neutral-Atom Qubits. *Physical Review Letters*, 114(10):100503, 2015. `arXiv:1501.02041`, `doi:10.1103/physrevlett.114.100503`.

[38] Ivaylo S. Madjarov, Jacob P. Covey, Adam L. Shaw, Joonhee Choi, Anant Kale, Alexandre Cooper, Hannes Pichler, Vladimir Schkolnik, Jason R. Williams, and Manuel Endres. High-fidelity entanglement and detection of alkaline-earth Rydberg atoms. *Nature Physics*, 16(8):857–861, 2020. `arXiv:2001.04455`, `doi:10.1038/s41567-020-0903-z`.

[39] Katrina Barnes, Peter Battaglino, Benjamin J. Bloom, Kayleigh Cassella, Robin Coxe, Nicole Crisosto, Jonathan P. King, Stanimir S. Kondov, Krish Kotru, Stuart C. Larsen, Joseph Lauigan, Brian J. Lester, Mickey McDonald, Eli Megidish, Sandeep Narayanaswami, Ciro Nishiguchi, Remy Notermans, Lucas S. Peng, Albert Ryou, Tsung-Yao Wu, and Michael Yarwood. Assembly and coherent control of a register of nuclear spin qubits. *Nature Communications*, 13(1):2779, 2022. `doi:10.1038/s41467-022-29977-z`.

[40] Nathan Schine, Aaron W Young, William J Eckner, Michael J Martin, and Adam M Kaufman. Long-lived Bell states in an array of optical clock qubits. *arXiv*, 2021. `arXiv:2111.14653`.

[41] Alec Jenkins, Joanna W. Lis, Aruku Senoo, William F. McGrew, and Adam M. Kaufman. Ytterbium Nuclear-Spin Qubits in an Optical Tweezer Array. *Physical Review X*, 12(2):021027, 2022. `arXiv:2112.06732`, `doi:10.1103/physrevx.12.021027`.

[42] Shuo Ma, Alex P. Burgers, Genyue Liu, Jack Wilson, Bichen Zhang, and Jeff D. Thompson. Universal Gate Operations on Nuclear Spin Qubits in an Optical Tweezer Array of ^{171}Yb Atoms. *Physical Review X*, 12(2):021028, 2022. `arXiv:2112.06799`, `doi:10.1103/physrevx.12.021028`.

[43] Masao Takamoto, Feng-Lei Hong, Ryoichi Higashi, and Hidetoshi Katori. An optical lattice clock. *Nature*, 435(7040):321, 2005. `doi:10.1038/nature03541`.

[44] Tobias Bothwell, Colin J. Kennedy, Alexander Aeppli, Dhruv Kedar, John M. Robinson, Eric Oelker, Alexander Staron, and Jun Ye. Resolving the gravitational redshift across a millimetre-scale atomic sample. *Nature*, 602(7897):420–424, 2022. `arXiv:2109.12238`, `doi:10.1038/s41586-021-04349-7`.

[45] Alexandre Cooper, Jacob P. Covey, Ivaylo S. Madjarov, Sergey G. Porsev, Marianna S. Safronova, and Manuel Endres. Alkaline-Earth Atoms in Optical Tweezers. *Physical Review X*, 8(4):041055, 2018. `arXiv:1810.06537`, `doi:10.1103/physrevx.8.041055`.

[46] M. A. Norcia, A. W. Young, and A. M. Kaufman. Microscopic Control and Detection of Ultracold Strontium in Optical-Tweezer Arrays. *Physical Review X*, 8(4):041054, 2018. `arXiv:1810.06626`, `doi:10.1103/physrevx.8.041054`.

[47] Samuel Saskin, Jack Wilson, Brandon Grinkemeyer, and Jeff Thompson. Narrow-Line Cooling and Imaging of Ytterbium Atoms in an Optical Tweezer Array. *Physical Review Letters*, (14), 2019. `arXiv:1810.10517`, `doi:10.1103/physrevlett.122.143002`.

[48] Matthew A. Norcia, Aaron W. Young, William J. Eckner, Eric Oelker, Jun Ye, and Adam M. Kaufman. Seconds-scale coherence on an optical clock transition in a tweezer array. *Science*, 366(6461):93–97, 2019. `arXiv:1904.10934`, `doi:10.1126/science.aay0644`.

[49] Ivaylo S. Madjarov, Alexandre Cooper, Adam L. Shaw, Jacob P. Covey, Vladimir Schkolnik, Tai Hyun Yoon, Jason R. Williams, and Manuel Endres. An Atomic-Array Optical Clock with Single-Atom Readout. *Physical Review X*, 9(4):041052, 2019. `arXiv:1908.05619`, `doi:10.1103/physrevx.9.041052`.

[50] Aaron W. Young, William J. Eckner, William R. Milner, Dhruv Kedar, Matthew A. Norcia, Eric Oelker, Nathan Schine, Jun Ye, and Adam M. Kaufman. Half-minute-scale atomic coherence and high relative stability in a tweezer clock. *Nature*, 588(7838):408–413, 2020. `doi:10.1038/s41586-020-3009-y`.

[51] K. Shibata, S. Kato, A. Yamaguchi, S. Uetake, and Y. Takahashi. A scalable quantum computer with ultranarrow optical transition of ultracold neutral atoms in an optical lattice. *Applied Physics B*, 97(4):753, 2009. `arXiv:0904.4523`, `doi:10.1007/s00340-009-3696-4`.

[52] A Yamaguchi, S Uetake, S Kato, H Ito, and Y Takahashi. High-resolution laser spectroscopy of a Bose–Einstein condensate using the ultranarrow magnetic quadrupole transition. *New Journal of Physics*, 12(10):103001, 2010. `doi:10.1088/1367-2630/12/10/103001`.

[53] S. Kato, K. Shibata, R. Yamamoto, Y. Yoshikawa, and Y. Takahashi. Optical magnetic resonance imaging with an ultra-narrow optical transition. *Applied Physics B*, 108(1):31–38, 2012. `doi:10.1007/s00340-012-4893-0`.

[54] V. A. Dzuba, V. V. Flambaum, and S. Schiller. Testing physics beyond the standard model through additional clock transitions in neutral ytterbium. *Physical Review A*, 98(2):022501, 2018. `arXiv:1803.02452`, `doi:10.1103/physreva.98.022501`.

[55] K. M. Maller, M. T. Lichtman, T. Xia, Y. Sun, M. J. Piotrowicz, A. W. Carr, L. Isenhower, and M. Saffman. Rydberg-blockade controlled-not gate and entanglement in a two-dimensional array of neutral-atom qubits. *Physical Review A*, 92(2):022336, 2015. `arXiv:1506.06416`, `doi:10.1103/physreva.92.022336`.

[56] A. V. Gorshkov, A. M. Rey, A. J. Daley, M. M. Boyd, J. Ye, P. Zoller, and M. D. Lukin. Alkaline-Earth-Metal Atoms as Few-Qubit Quantum Registers. *Physical Review Letters*, 102(11):110503, 2009. `arXiv:0812.3660`, `doi:10.1103/physrevlett.102.110503`.

[57] Tetsushi Takano, Shin-Ichi-Ro Tanaka, Ryo Namiki, and Yoshiro Takahashi. Manipulation of Nonclassical Atomic Spin States. *Physical Review Letters*, 104(1):013602, 2010. `arXiv:0909.2423`, `doi:10.1103/physrevlett.104.013602`.

[58] Nobuyuki Takei, Makoto Takeuchi, Yujiro Eto, Atsushi Noguchi, Peng Zhang, Masahito Ueda, and Mikio Kozuma. Faraday rotation with a single-nuclear-spin qubit in a high-finesse optical cavity. *Physical Review A*, 81(4):042331, 2010. `arXiv:0912.4948`, `doi:10.1103/physreva.81.042331`.

[59] Salvatore R. Manmana, Kaden R. A. Hazzard, Gang Chen, Adrian E. Feiguin, and Ana Maria Rey. SU(N) magnetism in chains of ultracold alkaline-earth-metal atoms: Mott transitions and quantum correlations. *Physical Review A*, 84(4):043601, 2011. `arXiv:1108.2327`, `doi:10.1103/physreva.84.043601`.

[60] A. V. Gorshkov, M. Hermele, V. Gurarie, C. Xu, P. S. Julienne, J. Ye, P. Zoller, E. Demler, M. D. Lukin, and A. M. Rey. Two-orbital SU(N) magnetism with ultracold alkaline-earth atoms. *Nature Physics*, 6(4):289–295, 2010. `arXiv:0905.2610`, `doi:10.1038/nphys1535`.

[61] T F Gallagher. Doubly excited states. *Journal of the Optical Society of America B*, 4(5):794, 1987. `doi:10.1364/josab.4.000794`.

[62] Alex P. Burgers, Shuo Ma, Sam Saskin, Jack Wilson, Miguel A. Alarcón, Chris H. Greene, and Jeff D. Thompson. Controlling Rydberg Excitations Using Ion-Core Transitions in Alkaline-Earth Atom-Tweezer Arrays. *PRX Quantum*, 3(2):020326, 2022. `doi:10.1103/prxquantum.3.020326`.

[63] Ky-Luc Pham, Thomas F. Gallagher, Pierre Pillet, Steven Lepoutre, and Patrick Cheinet. Coherent Light Shift on Alkaline-Earth Rydberg Atoms from Isolated Core Excitation without Autoionization. *PRX Quantum*, 3(2):020327, 2022. `doi:10.1103/prxquantum.3.020327`.

[64] J. T. Wilson, S. Saskin, Y. Meng, S. Ma, R. Dilip, A. P. Burgers, and J. D. Thompson. Trapping Alkaline Earth Rydberg Atoms Optical Tweezer Arrays. *Physical Review Letters*, 128(3):033201, 2022. `doi:10.1103/physrevlett.128.033201`.

[65] Morten Kjaergaard, Mollie E. Schwartz, Jochen Braumüller, Philip Krantz, Joel I.-J. Wang, Simon Gustavsson, and William D. Oliver. Superconducting Qubits: Current State of Play. *Annual Review of Condensed Matter Physics*, 11(1):1–27, 2019. `arXiv:1905.13641`, `doi:10.1146/annurev-conmatphys-031119-050605`.

[66] C. J. Ballance, T. P. Harty, N. M. Linke, M. A. Sepiol, and D. M. Lucas. High-Fidelity Quantum Logic Gates Using Trapped-Ion Hyperfine Qubits. *Physical Review Letters*, 117(6):060504, 2016. `arXiv:1512.04600`, `doi:10.1103/physrevlett.117.060504`.

[67] Morten Kjaergaard, Mollie E Schwartz, Ami Greene, Gabriel O Samach, Andreas Bengtsson, Michael O'Keeffe, Christopher M McNally, Jochen Braumüller, David K Kim, Philip Krantz, Milad Marvian, Alexander Melville, Bethany M Niedzielski, Youngkyu Sung, Roni Winik, Jonilyn Yoder, Danna Rosenberg, Kevin Obenland, Seth Lloyd, Terry P Orlando, Iman Marvian, Simon Gustavsson, and William D Oliver. Programming a quantum computer with quantum instructions. *arXiv*, 2020. `arXiv:2001.08838`.

[68] Craig R. Clark, Holly N. Tinkey, Brian C. Sawyer, Adam M. Meier, Karl A. Burkhardt, Christopher M. Seck, Christopher M. Shappert, Nicholas D. Guise, Curtis E. Volin, Spencer D.

Fallek, Harley T. Hayden, Wade G. Rellergert, and Kenton R. Brown. High-Fidelity Bell-State Preparation with $^{40}Ca^+$ Optical Qubits. *Physical Review Letters*, 127(13):130505, 2021. `arXiv:2105.05828`, `doi:10.1103/physrevlett.127.130505`.

[69] Chen Wang, Yvonne Y. Gao, Philip Reinhold, R. W. Heeres, Nissim Ofek, Kevin Chou, Christopher Axline, Matthew Reagor, Jacob Blumoff, K. M. Sliwa, L. Frunzio, S. M. Girvin, Liang Jiang, M. Mirrahimi, M. H. Devoret, and R. J. Schoelkopf. A Schrödinger cat living in two boxes. *Science*, 352(6289):1087–1091, 2016. `arXiv:1601.05505`, `doi:10.1126/science.aaf2941`.

[70] Pengfei Wang, Chun-Yang Luan, Mu Qiao, Mark Um, Junhua Zhang, Ye Wang, Xiao Yuan, Mile Gu, Jingning Zhang, and Kihwan Kim. Single ion qubit with estimated coherence time exceeding one hour. *Nature Communications*, 12(1):233, 2021. `arXiv:2008.00251`, `doi:10.1038/s41467-020-20330-w`.

[71] Yuto Ashida and Masahito Ueda. Multiparticle quantum dynamics under real-time observation. *Physical Review A*, 95(2):022124, 2017. `doi:10.1103/physreva.95.022124`.

[72] Denis A. Ivanov, Gabriel Mazzucchi, Igor B. Mekhov, and Santiago F. Caballero-Benitez. Quantum optical feedback control for creating strong correlations in many-body systems. *Optica*, 3(11):1213–1219, 2016. `doi:10.1364/optica.3.001213`.

[73] D. Yang, C. Laflamme, D. V. Vasilyev, M. A. Baranov, and P. Zoller. Theory of a Quantum Scanning Microscope for Cold Atoms. *Physical Review Letters*, 120(13):133601, 2018. `arXiv:1709.01530`, `doi:10.1103/physrevlett.120.133601`.

[74] D. Yang, D. V. Vasilyev, C. Laflamme, M. A. Baranov, and P. Zoller. Quantum scanning microscope for cold atoms. *Physical Review A*, 98(2):023852, 2018. `arXiv:1805.09220`, `doi:10.1103/physreva.98.023852`.

[75] J. E. Lye, J. J. Hope, and J. D. Close. Nondestructive dynamic detectors for Bose-Einstein condensates. *Physical Review A*, 67(4):043609, 2003. `doi:10.1103/physreva.67.043609`.

[76] J. J. Hope and J. D. Close. Limit to Minimally Destructive Optical Detection of Atoms. *Physical Review Letters*, 93(18):180402, 0. `doi:10.1103/physrevlett.93.180402`.

[77] J. J. Hope and J. D. Close. General limit to nondestructive optical detection of atoms. *Physical Review A*, 71(4):043822, 2005. `arXiv:quant-ph/0409160`, `doi:10.1103/physreva.71.043822`.

[78] Ulrik L Andersen, Tobias Gehring, Christoph Marquardt, and Gerd Leuchs. 30 years of squeezed light generation. *Physica Scripta*, 91(5):053001, 2016. `doi:10.1088/0031-8949/91/5/053001`.

[79] Florian Wolfgramm, Alessandro Cerè, Federica A. Beduini, Ana Predojević, Marco Koschorreck, and Morgan W. Mitchell. Squeezed-Light Optical Magnetometry. *Physical Review Letters*, 105(5):053601, 2010. `arXiv:1008.1721`, `doi:10.1103/physrevlett.105.053601`.

[80] N Otterstrom, R C Pooser, and B J Lawrie. Nonlinear optical magnetometry with accessible in situ optical squeezing. *Optics Letters*, 39(22):6533, 2014. `arXiv:1409.2935`, `doi:10.1364/ol.39.006533`.

[81] E. S. Polzik, J. Carri, and H. J. Kimble. Spectroscopy with squeezed light. *Physical Review Letters*, 68(20):3020–3023, 0. `doi:10.1103/physrevlett.68.3020`.

[82] H. Grote, K. Danzmann, K. L. Dooley, R. Schnabel, J. Slutsky, and H. Vahlbruch. First Long-Term Application of Squeezed States of Light in a Gravitational-Wave Observatory. *Physical Review Letters*, 110(18):181101, 2013. `arXiv:1302.2188`, `doi:10.1103/physrevlett.110.181101`.

[83] Michael A. Taylor, Jiri Janousek, Vincent Daria, Joachim Knittel, Boris Hage, Hans-A. Bachor, and Warwick P. Bowen. Biological measurement beyond the quantum limit. *Nature Photonics*, 7(3):229–233, 2013. `arXiv:1206.6928`, `doi:10.1038/nphoton.2012.346`.

[84] Samuel L. Braunstein and Peter van Loock. Quantum information with continuous variables. *Reviews of Modern Physics*, 77(2):513–577, 2005. `arXiv:quant-ph/0410100`, `doi:10.1103/revmodphys.77.513`.

[85] Morris Edgar Rose. *Elementary theory of angular momentum*. Courier Corporation, 1995.

[86] Vladimir Borisovich Berestetskii, Evgenii Mikhailovich Lifshitz, and Lev Petrovich Pitaevskii. *Quantum Electrodynamics: Volume 4*, volume 4. Butterworth-Heinemann, 1982. `doi:10.1016/C2009-0-24486-2`.

[87] M Ya Agre. Multipole expansions in quantum radiation theory. *arXiv*, 2014. `arXiv:1410.2232`.

[88] A. N. Moskalev D. A. Varshalovich and V. K. Khersonskii. *Quantum theory of angular momentum*. World Scientific, 1988. `doi:10.1142/0270`.

[89] N. L. Manakov, A. V. Meremianin, and Anthony F. Starace. Multipole Expansions of Irreducible Tensor Sets and Some Applications. *Journal of Physics B*, 22(76):148–148, 1977. `doi:10.1080/2052546.1977.11908842`.

[90] D.A. Steck. *Quantum and Atom Optics*. 2007. URL: `https://atomoptics.uoregon.edu/~dsteck/teaching/quantum-optics/`.

[91] D. J. Wineland and Wayne M. Itano. Laser cooling of atoms. *Physical Review A*, 20(4):1521–1540, 1979. `doi:10.1103/physreva.20.1521`.

[92] D. Leibfried, R. Blatt, C. Monroe, and D. Wineland. Quantum dynamics of single trapped ions. *Reviews of Modern Physics*, 75(1):281–324, 2003. `doi:10.1103/revmodphys.75.281`.

[93] A. Kramida, Yu. Ralchenko, J. Reader, and and NIST ASD Team. NIST Atomic Spectra Database (ver. 5.9), [Online]. Available: `https://physics.nist.gov/asd` [2016, January 31]. National Institute of Standards and Technology, Gaithersburg, MD., 2021.

[94] H. Lehec, A. Zuliani, W. Maineult, E. Luc-Koenig, P. Pillet, P. Cheinet, F. Niyaz, and T. F. Gallagher. Laser and microwave spectroscopy of even-parity Rydberg states of neutral ytterbium and multichannel-quantum-defect-theory analysis. *Physical Review A*, 98(6):062506, 2018. `arXiv:1805.02712`, `doi:10.1103/physreva.98.062506`.

[95] Y. Takasu, K. Komori, K. Honda, M. Kumakura, T. Yabuzaki, and Y. Takahashi. Photoassociation Spectroscopy of Laser-Cooled Ytterbium Atoms. *Physical Review Letters*, 93(12):123202, 2003. `doi:10.1103/physrevlett.93.123202`.

[96] K. Honda, Y. Takahashi, T. Kuwamoto, M. Fujimoto, K. Toyoda, K. Ishikawa, and T. Yabuzaki. Magneto-optical trapping of Yb atoms and a limit on the branching ratio of the $^1P_1$ state. *Physical Review A*, 59(2):R934–R937, 1999. `doi:10.1103/physreva.59.r934`.

[97] K. Beloy, J. A. Sherman, N. D. Lemke, N. Hinkley, C. W. Oates, and A. D. Ludlow. Determination of the 5d6s 3D1 state lifetime and blackbody-radiation clock shift in Yb. *Physical Review A*, 86(5):051404, 2012. `doi:10.1103/physreva.86.051404`.

[98] S. G. Porsev, Yu. G. Rakhlina, and M. G. Kozlov. Electric-dipole amplitudes, lifetimes, and polarizabilities of the low-lying levels of atomic ytterbium. *Physical Review A*, 60(4):2781–2785, 1999. `doi:10.1103/physreva.60.2781`.

[99] Thomas F. Gallagher. *Rydberg Atoms*. Cambridge Monographs on Atomic, Molecular and Chemical Physics. Cambridge University Press, 1994. `doi:10.1017/CBO9780511524530`.

[100] L. D. Landau and L. M. Lifshitz. *Quantum Mechanics Non-Relativistic Theory, Third Edition: Volume 3*. Butterworth-Heinemann, 3 edition. `doi:10.1016/C2013-0-02793-4`.

[101] V. A. Yerokhin, S. Y. Buhmann, S. Fritzsche, and A. Surzhykov. Electric dipole polarizabilities of Rydberg states of alkali-metal atoms. *Physical Review A*, 94(3):032503, 2016. `arXiv:1608.04515`, `doi:10.1103/physreva.94.032503`.

[102] Sylvain Ravets, Henning Labuhn, Daniel Barredo, Thierry Lahaye, and Antoine Browaeys. Measurement of the angular dependence of the dipole-dipole interaction between two individual Rydberg atoms at a Förster resonance. *Physical Review A*, 92(2):020701, 2015. `arXiv:1504.00301`, `doi:10.1103/physreva.92.020701`.

[103] Sylvain Ravets, Henning Labuhn, Daniel Barredo, Lucas Béguin, Thierry Lahaye, and Antoine Browaeys. Coherent dipole–dipole coupling between two single Rydberg atoms at an electrically-tuned Förster resonance. *Nature Physics*, 10(12):914–917, 2014. `arXiv:1405.7804`, `doi:10.1038/nphys3119`.

[104] Mireille Aymar, Chris H. Greene, and Eliane Luc-Koenig. Multichannel Rydberg spectroscopy of complex atoms. *Reviews of Modern Physics*, 68(4):1015–1123, 1996. `doi:10.1103/revmodphys.68.1015`.

[105] S. N. Pisharody and R. R. Jones. Probing Two-Electron Dynamics of an Atom. *Science*, 303(5659):813–815, 2004. `doi:10.1126/science.1092220`.

[106] M J Seaton. Quantum defect theory. *Reports on Progress in Physics*, 46(2):167, 1983. `doi:10.1088/0034-4885/46/2/002`.

[107] C L Vaillant, M P A Jones, and R M Potvliege. Multichannel quantum defect theory of strontium bound Rydberg states. *Journal of Physics B: Atomic, Molecular and Optical Physics*, 47(19):199601, 2014. `doi:10.1088/0953-4075/47/19/199601`.

[108] H Kitayoshi, S Sumiea, K Siirakawa, and S Takeshita. Dsp synthesized signal source for analog testing stimulus and new test method. In *Digest of Papers-International Test Conference*, pages 825–834. IEEE, 1985.

[109] S. J. M. Kuppens, K. L. Corwin, K. W. Miller, T. E. Chupp, and C. E. Wieman. Loading an optical dipole trap. *Physical Review A*, 62(1):013406, 2000. `doi:10.1103/physreva.62.013406`.

[110] A. Fuhrmanek, R. Bourgain, Y. R. P. Sortais, and A. Browaeys. Light-assisted collisions between a few cold atoms in a microscopic dipole trap. *Physical Review A*, 85(6):062708, 2012. `arXiv:1107.5781`, `doi:10.1103/physreva.85.062708`.

[111] Lukas Novotny and Bert Hecht. *Principles of Nano-Optics*. Cambridge University Press, 2 edition, 2012. `doi:10.1017/CBO9780511794193`.

[112] R Stephen Berry. The Theory of Penning Ionization. *Radiation Research*, 59(2):367, 1974. `doi:10.2307/3573984`.

[113] M. E. Gehm, K. M. O'Hara, T. A. Savard, and J. E. Thomas. Dynamics of noise-induced heating in atom traps. *Physical Review A*, 58(5):3914–3921, 1998. `doi:10.1103/physreva.58.3914`.

[114] C. Tuchendler, A. M. Lance, A. Browaeys, Y. R. P. Sortais, and P. Grangier. Energy distribution and cooling of a single atom in an optical tweezer. *Physical Review A*, 78(3):033425, 2008. `arXiv:0805.3510`, `doi:10.1103/physreva.78.033425`.

[115] Samuel Saskin. *Building Quantum Systems with Ytterbium Rydberg Arrays*. PhD thesis, Princeton University, 2021. URL: `https://dataspace.princeton.edu/handle/88435/dsp01vt150n404`.

[116] J F Wyart and P Camus. Extended analysis of the emission spectrum of neutral ytterbium (yb i). *Physica Scripta*, 20(1):43–59, jul 1979. `doi:10.1088/0031-8949/20/1/010`.

[117] F Lindenfelser, M Marinelli, V Negnevitsky, S Ragg, and J P Home. Cooling atomic ions with visible and infra-red light. *New Journal of Physics*, 19(6):063041, 2017. `doi:10.1088/1367-2630/aa7150`.

[118] J. I. Cirac, R. Blatt, P. Zoller, and W. D. Phillips. Laser cooling of trapped ions in a standing wave. *Physical Review A*, 46(5):2668–2681, 1992. `doi:10.1103/physreva.46.2668`.

[119] Ryuta Yamamoto, Jun Kobayashi, Kohei Kato, Takuma Kuno, Yuto Sakura, and Yoshiro Taka-hashi. Site-resolved imaging of single atoms with a Faraday quantum gas microscope. *Physical Review A*, 96(3):033610, 2017. `doi:10.1103/physreva.96.033610`.

[120] Meng Khoon Tey, Gleb Maslennikov, Timothy C H Liew, Syed Abdullah Aljunid, Florian Huber, Brenda Chng, Zilong Chen, Valerio Scarani, and Christian Kurtsiefer. Interfacing light and single atoms with a lens. *New Journal of Physics*, 11(4):043011, 2009. `doi:10.1088/1367-2630/11/4/043011`.

[121] D. J. Wineland, Wayne M. Itano, J. C. Bergquist, and Randall G. Hulet. Laser-cooling limits and single-ion spectroscopy. *Physical Review A*, 36(5):2220–2232, 1987. `doi:10.1103/physreva.36.2220`.

[122] Rodney Loudon. *The Quantum Theory of Light*. Clarendon Press, Oxford, 1973.

[123] Ryan S. Bennink and Robert W. Boyd. Improved measurement of multimode squeezed light via an eigenmode approach. *Physical Review A*, 66(5):053815, 2002. `doi:10.1103/physreva.66.053815`.

[124] Henning Vahlbruch, Moritz Mehmet, Karsten Danzmann, and Roman Schnabel. Detection of 15 dB Squeezed States of Light and their Application for the Absolute Calibration of Photoelectric Quantum Efficiency. *Physical Review Letters*, 117(11):110801, 2016. `doi:10.1103/physrevlett.117.110801`.

[125] Fam Le Kien, Philipp Schneeweiss, and Arno Rauschenbeutel. Dynamical polarizability of atoms in arbitrary light fields: general theory and application to cesium. *The European Physical Journal D*, 67(5):92, 2013. `doi:10.1140/epjd/e2013-30729-x`.

[126] Takafumi Tomita, Shuta Nakajima, Yosuke Takasu, and Yoshiro Takahashi. Dissipative Bose-Hubbard system with intrinsic two-body loss. *Physical Review A*, 99(3):031601, 2019. `arXiv:1809.09989`, `doi:10.1103/physreva.99.031601`.

謝辞

京都大学量子光学研究室の皆さまを始めとした多くの方々のご指導・ご協力のおかげで、この度本学位論文をまとめることができました。この場をお借りして心より感謝申し上げます。

指導教官である高橋義朗教授には修士の頃から5年余に渡り、いつも丁寧なご指導を頂きました。また博士課程に進学する際には、私の相談に乗って下さり、リドベルグ状態を用いた量子計算という挑戦的でやりがいのあるプロジェクトのスタートアップを担わせて頂きました。博士からの再スタートで不安もありましたが、折に触れ時には直接実験室まで来られて様子を気にかけて頂き、いつも的確なアドバイスを下さったおかげで、この度本論文の成果を上げることができました。重ねて御礼申し上げます。

高須洋介准教授、武井宣幸博士（現・東工大特定准教授）には実験の多岐にわたりご指導とサポートをして頂きました。高須さんには枝葉末節に至るまで様々なことをお聞きしましたが、いつも親切に対応して頂いたおかげで、安心して実験に取り組むことができました。157での実験を始めるに当たりこれは何ですかあれは何ですかと色々質問しましたが、一見ガラクタのように見えるものまでスラスラと教えて頂いた際には感動いたしました。武井さんには2年間にわたり直接の上司としていつも見守っていただきました。武井さんのフランクな人柄と私が失敗をしても笑って済ませて下さる暖かさがなければ、実験をこうしてコツコツと続けることはできなかったでしょう。グループの雰囲気や私達学生の自主性をいつも重視してくれていたこと、武井さんが東工大へ異動されてからは一層実感しました。御二方への感謝の念に堪えません。

小西秀樹博士には昨年8月から実験に参加して頂き、実験を大きく加速していただきました。順序立てて問題を処理していくだけでなく、より良い環境の構築を進めてくださり、効率的な研究の進め方を学ばせていただきました。実験や論文作成においては的確に私の間違いを指摘・修正していただき、私も僅かながら成長することができたのではないかと思います。ありがとうございました。

後輩のD1の中村勇真君、M2の草野透志君にはいつも精力的に実験を進めていただきました。二人とも色々と教えていたのも最初の頃だけで、気づけばこちらが教えてもらうようにすらなっていました。怠惰な私ですが、二人の情熱に刺激を受け、気を引き締めることができていたと思います。中村くんとは結果的に最も長く一緒に実験をしましたが、時に雑談に付き合ってもらいつつ、私の見落としの指摘などいつもサポートをしてくれました。草野くんには光源の開発・最適化などの作業を数多くしていただきました。退屈な作業が多かったのは申し訳なかったと思います。優秀な後輩と共に実験を進めることができて私は幸運でした。

岡山大学の原秀明助教とは D1 の 1 年間にわたり、断続的にではありますが、一緒に実験をさせて頂きました。修士の頃に身につけられていなかった知識や技術を原さんに教えて頂くことができて良かったと思います。環境も今ほど整っていなかったため大変なところもありましたが、原さんのおかげで一緒に楽しく実験をすることができました。PA 実験が途中のままになってしまっていることは残念ですが、最終的には何か成果を残すことができればと思います。

　I would also thanks to Phillip Lunt, Vikram Ramesh and Abilash Kumar Jha, who joined us as an intern. They contributed to our progress much. I wish their experience in Kyoto was meaningful for them.

　OB の富田隆文博士（現・分子研）には修士の間同じ QGM グループとして大変お世話になりましたが、分子研に着任されてからも同じリドベルグアレイの実験をしていることもあり、アドバイスを頂いたり合同セミナーを持ちかけてもらったりとまだまだお世話になっていることを感じ、頭の上がらない思いです。

　量子光学研究室の他のグループの方々にも多くの場面でお世話になりました。小野滉貴博士には居室や帰り道でいつも雑談に付き合って頂いた他、学位審査や学振についての事務的な手続き等についても丁寧に教えていただきました。実験では次々と成果を出されている姿に尊敬の念と奮起の思いを抱きます。また、QGM グループの髙田佳弘君にもよくオプティクスを貸していただいたり、雑談に付き合って貰いました。QGM グループを途中で抜ける形になり髙田くんへの負担が大きくなってしまい申し訳ありませんでした。単一格子点が見えたときは我が事のように嬉しかったです。今後の SU(N) ダイナミクス観測も応援しております。

　秘書の寺川さん、安原さんにはいつもご迷惑をおかけしております。情けないことに事務所類にしょっちゅう不備のある私ですが、いつもにこやかに対応してくださっていることに、ここで改めて感謝申し上げます。

　ここで名前を挙げなかった研究室の皆様に加え、機器開発室の皆様や事務室の方々、その他大勢の方々にお世話になりました。ありがとうございました。

　最後に博士課程修了までの長い間私を見守ってくれていた両親に感謝します。

令和四年五月
奥野大地